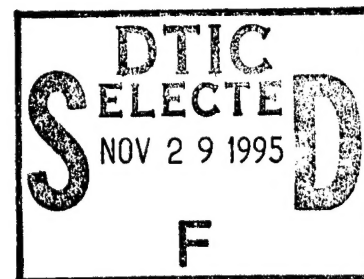


CARBON FIBER REINFORCED GLASS MATRIX COMPOSITES FOR SATELLITE APPLICATIONS

Prepared by

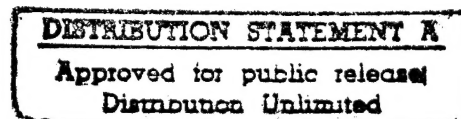
W. K. Tredway



FINAL REPORT

Contract N00014-89-C-0046

for



Department of the Navy
Office of Naval Research
Arlington, VA 22217

October 31, 1995



UNITED
TECHNOLOGIES
RESEARCH
CENTER

DTIC QUALITY INSPECTED 1

19951122 065

REPORT DOCUMENTATION PAGE

Form Approved
OMB No. 0704-0188

Public reporting burden for this collection of information is estimated to average 1 hour per response, including the time for reviewing instructions, searching existing data sources, gathering and maintaining the data needed, and completing and reviewing the collection of information. Send comments regarding this burden estimate or any other aspect of this collection of information, including suggestions for reducing this burden, to Washington Headquarters Services, Directorate for Information Operations and Reports, 1215 Jefferson Davis Highway, Suite 1204, Arlington, VA 22202-4302, and to the Office of Management and Budget, Paperwork Reduction Project (0704-0188), Washington, DC 20503.

1. AGENCY USE ONLY (Leave blank)		2. REPORT DATE 31 October 1995	3. REPORT TYPE AND DATES COVERED Final Report January 1989 - June 1995	
4. TITLE AND SUBTITLE CARBON FIBER REINFORCED GLASS MATRIX COMPOSITES FOR SATELLITE APPLICATIONS			5. FUNDING NUMBERS N00014-89-C-0046	
6. AUTHOR(S) W. K. Tredway				
7. PERFORMING ORGANIZATION NAME(S) AND ADDRESS(ES) United Technologies Research Center 411 Silver Lane East Hartford, CT 06108			8. PERFORMING ORGANIZATION REPORT NUMBER R95-5.102.0006-3	
9. SPONSORING/MONITORING AGENCY NAME(S) AND ADDRESS(ES) Department of the Navy Office of Naval Research Arlington, VA 22217			10. SPONSORING/MONITORING AGENCY REPORT NUMBER	
11. SUPPLEMENTARY NOTES				
12a. DISTRIBUTION / AVAILABILITY STATEMENT Unclassified/Unlimited			12b. DISTRIBUTION CODE	
13. ABSTRACT (Maximum 200 words) The development of carbon fiber reinforced glass and glass-ceramic matrix composites for satellite applications is described. A variety of carbon fibers (HMU, P-100, FT700, K1100X) have been used to reinforce borosilicate glass and BMAS glass-ceramics to create high performance composite materials useful for structural applications in space. Fundamental material properties that are described in this report include tensile and compressive stress-strain behavior, tensile and compressive fatigue behavior, effect of fiber orientation on tensile strength and elastic modulus, notch sensitivity, high temperature strength characteristics, thermal expansion behavior, thermal fatigue behavior, thermal conductivity characteristics, and space environmental durability. Also included is a section describing the fabrication and testing of very thin-gage (0.35 mm) C/Glass composites that have potential applications for thermal management applications. The final section describes work conducted by MSNW, Inc. to perform a detailed design study utilizing C/Glass composites for an NRL Deep Space Program Scientific Experiment (DSPSE) satellite component.				
14. SUBJECT TERMS glass matrix composites, carbon fiber reinforced composites, ceramic matrix composites, satellite applications			15. NUMBER OF PAGES 137	
			16. PRICE CODE	
17. SECURITY CLASSIFICATION OF REPORT Unclassified	18. SECURITY CLASSIFICATION OF THIS PAGE Unclassified	19. SECURITY CLASSIFICATION OF ABSTRACT Unclassified	20. LIMITATION OF ABSTRACT SAR	



R95-5.102.0006-3

**Carbon Fiber Reinforced Glass Matrix Composites
for Satellite Applications**

FINAL REPORT

Contract N00014-89-C-0046

REPORTED BY

William K. Tredway
William K. Tredway

APPROVED BY

Karl M. Prewo
Karl M. Prewo
Manager of
Advanced Ceramics

DATE October 31, 1995

Accession For	
NTIS CRA&I	<input checked="checked" type="checkbox"/>
DTIC TAB	<input type="checkbox"/>
Unannounced	<input type="checkbox"/>
Justification	
By	
Distribution /	
Availability Codes	
Dist	Avail and/or Special
A-1	

TABLE OF CONTENTS

<u>SECTION</u>	<u>PAGE</u>
I. PREFACE	1
II. FIBER REINFORCED GLASS MATRIX COMPOSITES FOR SPACE STRUCTURES	
1. Introduction	2
2. Materials	2
2.1 Fibers	
2.2 Matrices	
3. Fabrication Methods	4
4. Mechanical Properties	
4.1 Monotonic Tensile Stress-Strain Behavior	6
4.2 Effect of Fiber Orientation on Composite Behavior	8
4.3 Tensile Fatigue Behavior	10
4.4 Notch Sensitivity of C/Glass Composites	11
4.5 Compression Behavior	12
4.6 Cyclic Compression and Compression Fatigue Behavior	13
4.7 Reversed Mode Loading Behavior of C/Glass Composites	16
4.8 High Temperature Behavior	20
5. Thermophysical Properties	
5.1 Thermal Expansion	23
5.2 Thermal Fatigue Behavior	24
5.3 Thermal Conductivity	26
6. Space Environmental Durability	27
7. Summary	28

<u>SECTION</u>	<u>PAGE</u>
III. FABRICATION AND PROPERTIES OF THIN-GAGE GLASS MATRIX COMPOSITES FOR SPACE STRUCTURES	
1. Introduction	59
2. Composite Fabrication	59
3. Microstructural Examination	60
4. Tensile Behavior	61
5. Thermal Expansion Behavior	61
6. Thermal Conductivity	64
IV. DETAILED DESIGN OF C/GLASS COMPOSITES FOR DSPSE SATELLITE STIFFENERS	
- Summary	76
- Background	79
- Objectives	81
- Material Property Database	82
• Test Plan	82
• Experimental Data	83
• Preliminary B-basis Design Allowables	87
• Properties Used in Stiffener Design	92
- Detailed Structural Analysis	92
• DSPSE Geometry	93
• Finite Element Model	94
• Design Configurations	95
• Thermostructural Response	96
• Margins of Safety and Weight Savings	97
- Recommended Stiffener Design	101
- Conclusions and Recommendations	102

I. PREFACE

This report contains the results of work performed during the period from January, 1989 to June, 1995 on ONR Contract N00014-89-C-0046 to develop carbon fiber reinforced glass matrix (C/Glass) composites for structural satellite applications. Section II contains a broad overview of the results of this study with respect to the important mechanical, thermal, and thermomechanical behavior of C/Glass composites that were investigated. This section was intended to serve as a primer which could provide an introduction to C/Glass composites and present all of the information that is important in understanding how this material would perform in the space environment. Section III contains the results of a related study that was conducted in support of MSNW, Inc. to perform an evaluation of the potential satellite applications for C/Glass composites. In this study, very thin-gage C/Glass composites (~0.35 mm thick) were fabricated and tested in order to supply important property information to MSNW for their evaluation. Finally, section IV contains the results of a study conducted by MSNW for UTRC in support of contract N00014-89-C-0046. The purpose of this work was to conduct a detailed design study to use C/Glass composites as a stiffener component for an NRL Deep Space Program Scientific Experiment (DSPSE) spacecraft.

The author would like to thank Dr. Steve Fishman of the Office of Naval Research for serving as the Technical Monitor throughout the period of performance of this investigation.

This program was supported by the Ballistic Missile Defense Organization / Innovative Science and Technology through Office of Naval Research contract N00014-89-C-0046. Dr. Steve Fishman at ONR was the Technical Monitor.

II. FIBER REINFORCED GLASS MATRIX COMPOSITES FOR SPACE STRUCTURES

II.1. INTRODUCTION

Advanced materials being developed for structural applications in space will have extraordinary requirements placed on them due to the challenging demands of space structures. Depending on the particular application, issues such as dimensional stability, density, specific strength and stiffness, near-zero thermal expansion, and space environmental durability can be critically important factors. One of the materials being developed for utilization in space structures is carbon fiber reinforced glass (C/Glass). This exceptional class of materials has been the subject of investigation for many years due to the unique combination of high strength, stiffness, and toughness, low thermal expansion, low density, excellent tribological characteristics, and ease of fabrication. C/Glass composites offer performance equivalent or better than polymer and metal matrix systems in many areas. In addition, the superior temperature capability and extreme resistance to the space environment make C/Glass composites an attractive material for many space based applications. This section describes the behavior of C/Glass composites pertinent to use as a structural material in space.

II.2. MATERIALS

II.2.1 Fibers

One of the most attractive features of using carbon fibers as a reinforcement is the wide variety of carbon fibers that are available in terms of strength, elastic modulus, thermal expansion, and thermal conductivity. This makes possible the idea of tailoring, or engineering, composites for specific applications. Table II-1 summarizes some of the carbon fibers that are currently available along with the pertinent property data. It is clear from the data that density,

thermal expansion, and thermal conductivity are all closely related to fiber elastic modulus. In fact, all of these characteristics (including modulus) are established by the internal structure of the fiber, with crystallite size and the degree of crystallite orientation being the most dominant factors [1-2]. Fiber strength is somewhat dependent on these factors but is influenced to a greater extent by the presence and size of internal and surface defects. The internal and surface structure and surface chemistry can vary greatly for different types of fiber, with corresponding differences in fiber properties. For example, a polyacrylonitrile (PAN) based fiber such as HMU has a "skin-core" type microstructure, with an inner core consisting of curled and bent graphite crystallites surrounded by an outer skin of crystallites that are highly aligned with their basal planes parallel to the fiber surface (Figure II-1a). This results in a smooth fiber surface with a low surface energy characteristic of graphite basal planes. On the other hand, a high elastic modulus fiber derived from a mesophase pitch precursor, such as P-100, has a radial microstructure, with highly oriented graphite crystallites exhibiting radial alignment about the fiber axis (Figure II-1b). A significant fraction of these high energy edge planes intersect the fiber surface, resulting in an increase in fiber surface energy. Understanding the fiber surface morphology and chemistry is important since these characteristics are known to affect the nature of the fiber-matrix interface, which probably exerts the strongest influence on overall composite performance [3].

Table II-1 - Carbon Fiber Room Temperature Property Data

<u>Fiber</u>	<u>Manufacturer</u>	<u>Density</u> <u>(g/cm³)</u>	<u>Tensile</u> <u>Strength</u> <u>(MPa)</u>	<u>Tensile</u> <u>Modulus</u> <u>(GPa)</u>	<u>Axial</u> <u>Thermal</u> <u>Expansion</u> <u>(10⁻⁶ cm/cm K)</u>	<u>Axial</u> <u>Thermal</u> <u>Conductivity</u> <u>(W/m K)</u>
T-300	APP*	1.76	3100	234	-0.5	8.5
HMU	Hercules	1.84	2760	380	-0.7	80
FT500	Tonen	2.14	3000	500	-1.0	150
FT700	Tonen	2.16	3300	700	-1.5	360
P-100	APP*	2.16	2240	724	-1.6	520
P-120	APP*	2.18	2070	827	-1.6	520
K1100X	APP*	2.23	2350	920	-1.6	1030

* Amoco Performance Products

II.2.2 Matrices

A large number of glass and glass-ceramic compositions can be successfully utilized as matrix materials for C/Glass composites. Table II-2 lists some of the systems from which matrix compositions are commonly derived along with typical values of density, thermal expansion, and maximum temperature capability. Glass-ceramics are materials that exhibit the viscous characteristics of glass at temperatures above their melting point, thus enabling them to be formed into a variety of complex shapes. They also have the unique trait of being able to be converted from an amorphous material to a dense polycrystalline material through an appropriate heat treatment, thus imparting superior mechanical and temperature characteristics to the matrix. Again, it is important to realize that matrix chemistry can play a large role in determining overall composite performance. Reactions between the matrix and the fiber, or the lack thereof, can affect the strength of the fiber-matrix interface, which in turn controls many important aspects of composite behavior [3]. Also, it has been recently shown that the wetting behavior of the matrix on the carbon fiber is an important factor in determining fiber-matrix interfacial bond strength and subsequent composite performance [4].

Table II-2 - Matrix Materials Used for Carbon Fiber Reinforced Glass Composites

<u>Matrix Type</u>	<u>Matrix System</u>	<u>Density (g/cm³)</u>	<u>Thermal Expansion (10⁻⁶ m/m K)</u>	<u>Temperature Capability (°C)</u>
Glass	Borosilicate	2.2	3.2	500-560
Glass-Ceramic	LAS*	2.45	1.0	1000
"	BMAS**	2.7	3.0	1200
"	MAS [†]	2.6	1.0	1250

* LAS = Lithium aluminosilicate

** BMAS = Barium magnesium aluminosilicate

[†] MAS = Magnesium aluminosilicate

II.3. FABRICATION METHODS

The most common method of fabricating C/Glass composites is by hot-pressing multi-ply laminates consisting of carbon fiber and glass powder at a temperature well above the softening point of the glass [5-6]. In the case of glass-ceramic matrix compositions, the hot-pressing

temperature is also dependent on the crystallization behavior of the glass. Unitape prepregs are made by a slurry impregnation process whereby fiber tows are unwound from the supply spool, pulled through a slurry consisting of water, glass powder, and an acrylic binder, and then wound onto a hexagonal mandrel and allowed to dry. Prepregged fabric can also be produced by dipping the fabric in slurry and allowing it to dry. A composite preform is then made by cutting the prepreg into plies, stacking in the desired orientation, and thermally decomposing the binder. Final consolidation is achieved by loading the preform into a graphite die and hot-pressing using the appropriate conditions of temperature and pressure. C/Glass composites fabricated via this method are typically fully densified with less than 1% porosity.

The size of composite articles that can be fabricated via hot-pressing is limited only by the size of the furnace chamber. As part of this program, flat panels of [0/90] reinforced C/Glass up to 51 cm x 20 cm in size and 0.25 cm thick have been fabricated in a large hot-press at United Technologies Research Center (UTRC). Composite thickness can also vary considerably, ranging from a practical maximum of 1.25 cm all the way down to as thin as 0.25 mm. While the complexity of parts that can be fabricated via hot-pressing is somewhat limited, the geometries that can be produced are not restricted to flat panels. Curved "hat-section" beams, airfoil shapes, and other complex structures have also been successfully fabricated using hot-pressing techniques.

Other techniques have also been utilized to produce C/Glass composite articles in situations where external and/or internal structural geometries are too complex for hot-pressing. Examples of such techniques are: (1) injection molding, where chopped carbon fiber and glass powder are injected into a die cavity at high temperature; (2) matrix transfer molding, where molten glass is transferred from a reservoir into a rigidized fiber preform at high temperature, and; (3) hot isostatic pressing (HIP), where isostatic pressure is used to consolidate the composite preform inside a vacuum-evacuated can. The technique that has been investigated most recently at UTRC for its potential to fabricate C/Glass composites for space structures is HIP. Specifically, HIP has been used to fabricate continuously reinforced circular cross-section (2.5 to 4.4 cm diameter) and square cross-section (2.5 cm square) thin-walled tubular elements in lengths up to 30 cm (Figure II-2a). In addition, L-beams in lengths up to 122 cm have also been fabricated by HIP; Figure II-2b shows examples of L-beams that are 61 and 91 cm in length. Details of the steps involved in HIP processing were summarized in a previous report [7]. One of the major advantages of using HIP for fabrication of tubes and beams is that it allows for the scale-up of parts to lengths of 3 meters. Such structural elements are commonly envisioned as the main components of satellite truss structures. Section IV of this report describes the design and structural analysis of a C/Glass component for an NRL satellite. The fabrication and compression testing of HIP'ed C/Glass tubes was described in a previous report [7].

II.4. MECHANICAL PROPERTIES

II.4.1 Monotonic Tensile Stress-Strain Behavior

C/Glass composites typically exhibit non-linear tensile stress-strain behavior that is quite unique in its characteristics. In general, the high tensile strength of the carbon fibers used as reinforcement translates to reasonably high composite strength, with values for unidirectionally reinforced composites ranging from 500 MPa to 900 MPa, depending on the type of fiber and the fiber volume fraction. C/Glass composites also generally exhibit significant fiber pullout and crack bridging during fracture, indicating a reasonable degree of toughness. However, the aforementioned differences in fiber surface morphology, fiber surface chemistry, matrix chemistry, and matrix wetting behavior can lead to substantial differences in composite stress-strain behavior depending on the exact nature of the fiber-matrix interface. In this section the tensile stress-strain behavior of two borosilicate glass matrix composites, one containing PAN-based HMU fiber and the other reinforced with pitch-based fiber (P-100 or FT700), will be described and compared with respect to various features of the stress-strain curve and how they relate to interfacial strength.

Figure II-3 shows a typical stress-strain curve for a unidirectional HMU reinforced borosilicate glass (HMU/BSG) composite containing approximately 45 vol% fiber. Upon initial loading the composite displays linear elastic behavior up to a stress and strain of about 400 MPa and 0.25%, respectively. In this initial linear region, the composite elastic modulus is predictable based on a combination of stiffness from the carbon fibers and the glass matrix. At the upper level of this initial linear region, the stress-strain curve deviates significantly from linearity, passing through a transition region of increasing strain with very little increase in stress. The point where the curve deviates from linearity is commonly referred to as the proportional limit (PL). In the HMU/BSG composite system, it has been suggested that the PL and the subsequent "plateau" region correspond to wide-scale microcracking of the matrix and fiber-matrix debonding [8]. However, recent evidence in the literature obtained using acoustic emission indicates that the initiation of microcracking in this composite system actually begins much earlier at about 125 MPa [9]. It is likely that the microcrack density continues to increase on extended loading from 125 MPa until it reaches a saturation level, followed by fiber-matrix debonding at the PL and plateau region. Similar behavior has been observed in other fiber reinforced ceramic composites. The occurrence of wide-scale microcracking in the HMU/BSG composite is verified by the fact that on unloading and reloading after passing through the plateau region, the composite elastic modulus is decreased from the original by an amount attributable to a loss of matrix stiffness.

Following the transition region, the curve again exhibits linear behavior representative of the fibers carrying the load alone after matrix microcracking. The mechanism of fiber-matrix debonding prior to this stage is critical to the fibers being able to carry the load until they reach their inherent failure strain of 0.7%. If significant debonding did not occur, matrix cracks would experience little if any deflection and would instead propagate directly through the fibers, resulting in lower composite strength and near-brittle failure. A considerable amount of fiber pullout typifies fracture surfaces in HMU/BSG composites, indicative of low fiber-matrix interfacial strength.

While the performance of HMU/BSG composites is exceptional in terms of strength and toughness, stiffness-critical applications in space structures will most likely require the utilization of higher elastic modulus pitch-based carbon fibers, such as P-100 or FT700. The tensile stress-strain behavior of P-100/BSG and FT700/BSG composites differs in several respects from that of HMU/BSG composites. The curve in Figure II-3 illustrates the tensile behavior of a unidirectionally reinforced P-100/BSG composite containing approximately 40 vol% fiber (this curve is also typical of the behavior of FT700/BSG composites). The initial portion of the curve is again representative of linear elastic behavior which is predictable based on a rule-of-mixtures approach, with the elastic modulus being at an acceptably high level for many stiffness-critical space applications. The curve experiences a PL at a stress and strain of about 125 MPa and 0.03%, respectively, followed by a secondary region of steadily decreasing slope. The fibers continue to carry the load until they reach their failure strain of approximately 0.2%.

The stress-strain curves of the HMU and P-100 reinforced materials differ in two main respects: 1) the P-100/BSG composite does not exhibit the sudden increase in strain following the PL, and; 2) the secondary region representative of fibers carrying the load alone in the P-100/BSG composite is not linear, but instead exhibits a negative curvature with increasing strain. The two materials also differ in the sense that, in contrast to the HMU reinforced system, strain cycling of the P-100/BSG composite past the PL does not result in any change in the initial elastic modulus. The mechanism for this is described below. The fracture behavior of the P-100/BSG composite also differs from that of the HMU/BSG composite, with fiber pullout not being as extensive in the P-100/BSG material. These dissimilarities between the two composite systems are due in large part to differences in the nature of the fiber-matrix interface caused by the unlike surface structure and surface chemistry of HMU and P-100 carbon fiber. Stronger interfacial bonding in the P-100/BSG composite resulting from a rougher surface and a higher surface energy along with the lower *in-situ* strength of the P-100 fibers are thought to lead to shorter pullout lengths and reduced composite toughness.

The PL in the P-100/BSG composite, as in the HMU/BSG system, seems to correspond to a loss in the matrix contribution to the composite elastic modulus. However, the mechanism by

which the matrix stiffness is decoupled from the composite in the P-100/BSG composite is not yet certain. Calculations of residual matrix tensile stress in the P-100/BSG system using the composite cylinder assemblage model show that the magnitude of matrix tensile stress generated during cooling parallel to the fiber direction is approximately 125 MPa at room temperature [10]. This level of stress is great enough to generate a considerable number of *pre-existing* matrix microcracks in the P-100/BSG composite due to thermal residual stresses alone, as shown in Figure II-4. This figure shows an optical micrograph of a replica of the surface of a 0° reinforced P-100/BSG composite after fabrication and before any testing. It is evident from the micrograph that a large number of evenly spaced microcracks exist running normal to the fiber direction, with an average crack spacing of about 160 μm . Other experimental evidence regarding pre-existing matrix microcracks has been gathered using acoustic emission monitoring of FT700/BSG composite specimens during tensile testing. Signals normally associated with matrix cracking were not detected throughout the entire loading cycle, suggesting that the matrix may have already been fully microcracked from thermal residual stresses. Also, cyclic tensile testing [11] and tensile fatigue testing of P-100/BSG and FT700/BSG composites at UTRC have shown that loading of tensile specimens to a point well beyond the PL does not result in any loss of initial composite stiffness during reloading in subsequent cycles.

This behavior is in sharp contrast to the HMU/BSG system, where loading above the PL results in a permanent decrease in initial modulus on reloading by an amount corresponding to the matrix contribution to composite stiffness [8], indicating that the matrix has fully cracked and debonded from the fibers. The "recoverable" loss in modulus observed in the P-100/BSG and FT700/BSG systems suggests that another mechanism is responsible for the non-linear stress-strain behavior in these composites. One possible mechanism proposed here is that Poisson contraction of the fibers away from the matrix during loading coupled with the high interfacial tensile stress (from thermal expansion mismatch) in the P-100/BSG and FT700/BSG systems results in gradual decoupling of the fibers from the matrix during loading, causing a progressive reduction in load transfer from the matrix to the fibers. This would account for the steadily decreasing slope of the stress-strain curve in the secondary region after the PL (Figure II-3) as well as the recovery of the original composite stiffness on unloading. Continued work is underway at UTRC to confirm the mechanism(s) responsible for the non-linear stress-strain behavior in the P-100/BSG, FT700/BSG, and other high modulus pitch fiber reinforced systems.

II.4.2 Effect of Fiber Orientation on Composite Behavior

The effect of fiber orientation on the tensile stress-strain behavior of HMU/BSG composites has been studied previously [8]. In that study, it was found that the dependence of

the UTS and elastic modulus on ply angle θ (for unidirectional composites) or $\pm\theta$ (for angle-ply composites) could be well-described using classical laminate theory (Figures II-5 and II-6). The UTS was accurately predicted in these composites by the Tsai-Hill (maximum work) failure criterion. More recently, work has been performed at UTRC to determine the effect of fiber orientation on the performance of FT700/BSG composites. As in the previous study, both unidirectional (θ) and angle-ply ($\pm\theta$) composites were investigated. The particular aspects of performance that were assessed as a function of fiber angle were UTS and elastic modulus.

Classical laminate theory [12] was used to predict the elastic modulus of the FT700/BSG composites as a function of ply angle θ . The results for both unidirectional and angle-ply composites are shown in Figure II-7. The values used for composite longitudinal modulus (329 GPa) Poisson's ratio (0.18) are the experimentally measured values for the 0° reinforced composite. The value used for transverse elastic modulus was estimated based on transverse tensile tests of P-100/BSG composites. The composite shear modulus G was used as an adjustable parameter to fit the data. In order to obtain the best fit, the value of G for the angle-ply composites was only half that of the unidirectional composites. This is similar to behavior exhibited in the HMU/BSG system [8] and may be due to higher interply stresses in the angle-ply composites caused due to ply anisotropy in thermal expansion. In general, good agreement was seen between the predicted and measured elastic moduli in both the unidirectional and angle-ply composites.

Two different strength theories, the maximum stress failure criterion and the maximum work failure criterion, were used to predict the ultimate tensile strength of the unidirectionally reinforced composites as a function of θ . In the maximum stress failure criterion, composite failure is assumed to occur by either tensile fiber failure, shear failure of the fiber-matrix interface or the matrix, or tensile failure of the fiber-matrix interface or matrix [12]. The maximum stress theory predicts that composite failure will occur by the mechanism exhibiting the lowest value of strength at a particular value of θ . The maximum work failure criterion is based on the von Mises failure criterion describing a failure "envelope" or surface in three-dimensional space [12]. This approach takes account of interactions that occur between tensile and shear stresses in the material and considers the complex nature of fracture that typically occurs in composites.

Both the maximum stress failure criterion and the maximum work failure criterion provided very good descriptions of the tensile strength exhibited by the unidirectionally reinforced composites as a function of θ (Figure II-8a). In these calculations, the value of τ (shear strength) was used as an adjustable parameter to fit the data. A value of 28 MPa was found to provide the best fit and agrees well with the previously reported work on the HMU/BSG system [8]. The variation of strength as a function of θ for each of the three mechanisms of the maximum stress

theory is shown along with the prediction of the maximum work theory. It appears from the figure that the good agreement with the maximum strength theory was fortuitous; a composite with a 20° off-axis orientation may not have fit the theory as well. The fit of the angle-ply composite data to the maximum work theory was not as good as that seen in the unidirectionally reinforced composites. Figure II-8b shows the predicted (maximum work) and experimental strengths for both unidirectional and angle-ply reinforced FT700/BSG composites. The $\pm 10^\circ$ and $\pm 45^\circ$ angle-ply orientations do not show particularly good agreement with the maximum work prediction. The reason for this lack of agreement in the angle-ply composites is not understood. It may relate to complex interactions and failure mechanisms in these angle-ply FT700/BSG composites that are not accounted for in the maximum work theory.

II.4.3 Tensile Fatigue Behavior

The tensile fatigue behavior of unidirectional and [0/90] reinforced HMU/BSG composites has been evaluated previously [13]. Testing was performed at North Carolina A&T State University on material that was fabricated at UTRC. Samples were tested in a tensile-tensile mode at a frequency of 10 Hz and an R-ratio (maximum stress/minimum stress) of 0.10. All tests where failure did not occur during fatigue were stopped after 10^6 cycles and then uploaded to failure to determine the residual strength after fatigue. Samples were tested at several peak stress levels below and above the PL stress. The results for both unidirectional and [0/90] reinforced HMU/BSG composites are shown in Figures II-9 and II-10. For both composites, runout to 10^6 cycles was observed up to peak stress levels representing about 75-80% of the ultimate tensile strength (as determined via monotonic tensile testing on samples obtained from each composite panel). Above this peak stress level, fatigue failures were observed, with the number of cycles to failure decreasing with increasing peak stress. The residual strength of the samples that experienced runout was equal to or greater than the monotonic tensile strength in every case. This aspect of the fatigue behavior of these materials is not fully understood; however, similar behavior has been observed in other carbon fiber reinforced ceramic matrix composite systems [14].

More recently, evaluation of the tensile-tensile fatigue behavior of pitch carbon fiber reinforced BSG composites has been conducted at UTRC. Specific composite systems under investigation were 0° FT700/BSG and [0/90] P-100/BSG. While not as extensive as the fatigue testing just described for the HMU/BSG system, the trends demonstrated are similar to those exhibited by the HMU/BSG composites. Figures II-11 and II-12 illustrate the tensile-tensile fatigue results obtained for the two different composites. The same parameters that were described for the HMU/BSG testing were also used for evaluation of the [0/90] P-100/BSG composites. For the 0° FT700/BSG composites, the frequency was reduced to 0.33 Hz and

testing was stopped after reaching 10^5 cycles. (Cycle time was reduced for the FT700/BSG composites to allow for better data acquisition during each cycle.) It is clear from Figure II-11 that the behavior of the 0° FT700/BSG system is similar to that of the HMU/BSG system. Again, runout was observed up to a peak stress level of about 75-80% of the monotonic tensile strength, with higher peak loads resulting in fatigue failures. Residual tensile strength after fatigue was again equal to or greater than the monotonic tensile strength, indicating that fatigue at these peak stress levels was not inducing fiber damage. The behavior of the [0/90] P-100/BSG composite shown in Figure II-12 indicates that similar trends are also exhibited.

The tensile-tensile fatigue behavior of all the C/Glass systems just described indicates that fatigue failures will not be a concern for peak stress levels up to at least 60% of the ultimate tensile strength (for lifetimes of up to 10^6 cycles). The fatigue failures that were observed at higher peak stresses ($> 75\%$ of the ultimate tensile strength) are thought to be at least partially related to the statistical nature of fiber tensile strength. As the ultimate composite strength is approached at the higher peak stress levels, weaker fibers in the composite begin to fail, leaving fewer fibers to carry the load. These remaining fibers are then subjected to a higher level of stress, resulting in composite failure at loads below the ultimate (monotonic) tensile strength.

II.4.4 Notch Sensitivity of C/Glass Composites

Another aspect of the performance of C/Glass composites that has been evaluated is the sensitivity of the materials to the presence of a notch, which acts as a stress concentrator during mechanical loading. For elliptical shaped holes oriented with the major axis of the ellipse normal to the direction of the applied stress, the stress concentration factor (K) depends on the degree of elongation of the ellipse [12]. Long flat elliptical holes or cracks that are oriented with the long direction normal to the direction of the applied stress result in very large stress concentration factors at the tip of the notch. When taking into account the smaller load-bearing cross-section resulting from the presence of the notch, materials that are notch insensitive will maintain a constant level of strength irrespective of the value of K. Notch sensitive materials, on the other hand, will show a steady decrease in strength with increasing K (i.e., sharper notches). For the special geometrical case of a circular notch, the stress concentration factor K is 3 at the edge of the hole and is independent of hole diameter. Notch sensitive materials containing circular holes would exhibit a decrease in strength compared to unnotched material. However, unlike the case for elliptical holes, the strength drop would be constant for any size hole since the stress concentration factor is always the same.

To evaluate the degree of notch sensitivity in C/Glass composites, circular holes ranging in diameter from 1.6 mm to 6.5 mm were drilled ultrasonically in the center of [0/90] reinforced

tensile samples in the HMU/BSG, FT700/BSG, and P-100/BSG systems. The effect of the notches on the tensile strength of the [0/90] HMU/BSG composites has been reported previously [15]. Figure II-13(a) shows the tensile strength as a function of the ratio of hole diameter to specimen width (d/b) for the HMU/BSG system. The dashed lines on the figure indicate a "scatter band" of strengths that were observed in this material (*i.e.*, all of the observed strengths fall within the scatter band). It is clear that the level of strength in the HMU/BSG system is fairly constant for both unnotched and notched samples, indicating that the composites in this system are notch insensitive. The notch sensitivity of the FT700/BSG and P-100/BSG systems has been investigated more recently. Figure II-14(a) shows the results for the FT700/BSG system. As described for the HMU/BSG system, the strength of the FT700/BSG composites is essentially constant within the scatter band for all the samples, indicating that this system is also notch insensitive. The results for the P-100/BSG system are shown in Figure II-15(a). Unlike the other two systems described previously, the P-100/BSG composites containing circular holes exhibited a decrease in strength (~15-25%) compared to the unnotched material. As expected with circular notches, the degree of strength loss was fairly constant for all of the notched samples. This behavior indicates that the P-100/BSG system is sensitive to the presence of a notch, although the degree of notch sensitivity is not that large (*viz.*, the material still retains at least 75% of its original strength).

The reason for the notch insensitivity observed in the HMU/BSG and FT700/BSG composites is thought to be related to the relatively weak fiber-matrix interfacial bond that exists in these systems. The degree of notch sensitivity in a material is related to the way that the material responds to the concentrated stress field at the notch tip [12]. Mechanisms such as matrix microcracking and fiber-matrix debonding can serve to quickly dissipate the concentrated stress and make the material notch insensitive. Examination of fracture surfaces in the vicinity of the notch in the HMU/BSG and FT700/BSG systems indicated a significant degree of fiber pullout [Figures 13(b) and 14(b)], suggesting that the primary means of concentrated stress relief in these composites was via fiber-matrix debonding. The reason for the slight notch sensitivity observed in the P-100/BSG system is unclear, since every other aspect of its mechanical behavior is similar to that of the FT700/BSG system. Adding to the inconsistency is the appearance of the notched P-100/BSG composite fracture surfaces [Figure II-15(b)], which exhibited an amount of fiber pullout very similar to that observed in the FT700/BSG composites.

II.4.5 Compression Behavior

Many types of space structures, such as tubes for satellite trusses, will be loaded primarily in compression. The compression behavior of unidirectional and [0/90] reinforced HMU/BSG, FT700/BSG, and P-100/BSG composites as determined using the Celanese specimen geometry

and test fixture is summarized in Table II-3. (The HMU/BSG composites were tested at Martin Marietta as part of an Air Force/SDIO program to generate mechanical and thermal property data on potential spacecraft structural materials. Complete information can be found in the handbook prepared at the end of the Martin Marietta program [16]). The elastic moduli for all three composite systems agree well with those predicted using a rule-of-mixtures approach. The ultimate compressive strength (UCS) for the HMU/BSG composite is essentially equivalent to the tensile strength exhibited by this system. The high values of the ratio of UCS to UTS as compared to polymer matrix or metal matrix composites is due to the excellent compressive strength of the ceramic matrix, which provides full support for the carbon fibers until they fail either by kinking, bending, or shearing. The lower values of UCS demonstrated by the FT700/BSG and P-100/BSG composites are due to the poor compressive strength of high modulus pitch based carbon fibers that results from the highly oriented radial internal structure of the fiber. Inherent to this structure is a relatively low shear strength between graphite basal planes, which inevitably leads to failure by shear when loaded in compression [17-18]. However, the values of UCS for this system are comparable to P-100 reinforced polymer matrix and metal matrix composites.

Table II-3 - Compression Behavior of HMU/BSG and P-100/BSG Composites

<u>Composite System</u>	<u>Fiber Volume %</u>	<u>Orientation</u>	<u>Number of Samples</u>	<u>Ultimate Compressive Strength (MPa)</u>	<u>Elastic Modulus (GPa)</u>
HMU/BSG	44	0°	4	870 ± 18	147 ± 3
	40	[0/90]	3	600 ± 32	86 ± 8
FT700/BSG	52	0°	3	419 ± 42	391 ± 14
	46	[0/90]	3	215 ± 19	169 ± 16
P-100/BSG	43	0°	3	385 ± 5	356 ± 42
	44	[0/90]	2	230 ± 2	162 ± 7

II.4.6 Cyclic Compression and Compression Fatigue Behavior

Cyclic compression and compression fatigue testing at room temperature was performed on P-100/BSG-2 composites having fiber orientations of either 0° or (0/+20/0/0/-20/0)_s. Unidirectional samples were chosen as the baseline material, while the 0/±θ/0 orientation was

selected to compare with the results obtained for thin-walled tubes that had been compression tested in work reported previously [7]. Samples for both types of testing had a 1.27 cm gage length and were machined from flat panels fabricated using conventional hot-pressing methods.

Cyclic Compression Testing

Cyclic compression testing was performed by loading the composites to successively higher stress levels over a four or five period cycle, with the composite being loaded to failure on the final cycle. A cross-head displacement rate of 0.13 cm/min was used. Each specimen was completely unloaded in-between loading cycles. Figure II-16 contains the compressive stress-strain curves for the first, second and fourth cycles for a unidirectional P-100/BSG-2 composite, while data for all cycles are given in Table II-4. The stress-strain curves indicate that as the load was increased during successive cycles, the area of the hysteresis loop increases, indicating an increase in the amount of energy dissipated in the specimen. Examples of processes that could be responsible for energy dissipation during loading-unloading could be fiber-matrix interfacial sliding or slipping between individual graphite planes within the carbon fiber. A small amount of permanent deformation was introduced into the sample during cycling, indicated by the failure of the loop to close during unloading. As can be seen from the data in Table II-4, no significant change in the elastic modulus of the material was observed during successive loading cycles.

Shown in Figure II-17 is the cyclic stress-strain response for the first, second and fourth cycles on a (0/+20/0/0/-20/0)_s P-100/BSG-2 composite, with the data for all cycles being shown in Table II-4. As in the unidirectional material, the amount of energy dissipated in the multiaxial composite (as measured by the area of the hysteresis loop) increased with increasing load level, a small amount of permanent strain was introduced during cycling, and no change in the elastic modulus was seen during the four successive loading cycles.

Both the unidirectional and the multiaxial reinforced materials were loaded to failure in compression following cyclic compressive testing. Determination of the ultimate compressive properties after cyclic loading showed only a slight deviation in the compressive strength and modulus compared to the monotonic properties. It is interesting that although the cyclic stress-strain curves of Figures 16 and 17 represent energy having been dissipated in the composites, this energy did not result in severe degradation of the ultimate compressive properties of either composite. It is believed that the work performed on the composites during cyclical loading induced some damage in the high modulus P-100 fibers by creating shear bands, as described previously. The fact that a slight degradation in the UCS was observed following cyclic testing supports this belief. During successively higher loads, the damage is most likely increased, but this damage is not manifested in a severe UCS degradation because the matrix still supports the

fibers. As discussed later in this report, tensile testing of P-100/BSG-2 samples that were loaded initially in compression showed a significant decrease in the ultimate tensile properties. In this case, the damage to the fibers was not supported by the glass matrix, because the matrix has little strength in tension, and a dramatic drop in composite UTS was observed.

Table II-4 - Cyclic Compression Properties of P-100/BSG-2 Composites

<u>Fiber Orientation</u>	<u>Cycle No.</u>	<u>Maximum Stress (MPa)</u>	<u>E (GPa)</u>
0°	<i>Monotonic Data</i>	366	242
	1	123	249
	2	190	259
	3	248	254
	4	316	261
	UCS	326	257
(0/+20/0/0/-20/0)	<i>Monotonic Data</i>	351	308
	1	82	269
	2	186	260
	3	224	262
	4	261	265
	5	300	260
	UCS	301	259

Compressive Fatigue Testing

Compressive fatigue testing was carried out at a compressive peak stress of 250 MPa (70% of the UCS) an R ratio of 0.1, and a loading frequency of 0.33 Hz. This frequency corresponds to a crosshead displacement of approximately 0.07cm/min for these specimens.

Figure II-18 shows the change in the compressive elastic modulus (measured during loading) with increasing number of cycles for both fiber orientations. The unidirectional composite shows no decrease in modulus, even after 200,000 cycles. At approximately 208,000

cycles, the sample was uploaded to failure and exhibited a compressive strength of 362 MPa. This compares favorably with the monotonic UCS of 366 MPa for this composite (Table II-4), indicating that compressive fatigue loading did not affect the residual compressive strength of the unidirectionally reinforced material. The multiaxial composite exhibited markedly different behavior. At some point during the first cycle, damage was imparted into the specimen, as evidenced by the sharp decrease in the elastic modulus measured during the second cycle loading. From the second cycle to the 26,000th cycle, the elastic modulus continued to decrease until the composite failed during uploading at 246 MPa.

Insight into the difference in behavior for the two specimens can be found by examining the fracture surfaces seen in Figure II-19. The unidirectional composite (Fig. II-19a) showed no degradation of material compressive properties after 208,000 cycles, and the fracture surface is very similar to monotonic compressive fracture surfaces. The unidirectional fibers show a classic shear failure surface at 45° , typical of P-100/BSG composites. In the case of the $(0/+20/0/0/-20/0)_s$ composite, severe degradation of the compressive strength and modulus resulted from fatigue loading. From Figure II-19b, it is evident that the degradation of the properties was associated with a delamination along the fiber axis in the $\pm 20^\circ$ direction. The fracture surface indicates fiber-matrix debonding in the off axis plies, while in the 0° fibers, classic shear failure is seen in the high modulus carbon fibers. Further evidence for this damage mode is shown by calculating the properties of a $(0/+20/0/0/-20/0)_s$ composite assuming the $\pm 20^\circ$ plies do not contribute. In the $(0/+20/0/0/-20/0)_s$ composite, 33% of the reinforcing fiber is in the off-axis direction. A calculated 33% reduction in the monotonic UCS and elastic modulus (Table II-4) gives values of 244 MPa for strength and 191 GPa for modulus. The dashed line in Figure II-19 corresponds to an elastic modulus of 191 GPa. As is seen in the figure, the $(0/+20/0/0/-20/0)_s$ composite modulus decreases during fatigue testing to this value, indicating that contribution to the modulus by the $\pm 20^\circ$ plies decreases with increasing fatigue. The composite failed at a strength of 246 MPa, which is in good agreement with the calculated value.

Although evident in fatigue testing, fiber-matrix debonding and the associated decrease in composite modulus was not seen in the $(0/+20/0/0/-20/0)_s$ composite panels studied in cyclic compression testing (described previously). This discrepancy is not completely understood at this time.

II.4.7 Reversed Mode Loading Behavior of C/Glass Composites

The effects of reversed mode loading on carbon fiber reinforced borosilicate glass composites was investigated for both unidirectionally reinforced HMU/BSG and P-100/BSG composites. Reversed mode loading consists of loading a sample in compression to a fixed level

(below failure), and subsequently loading the same sample in tension until failure, or, conversely, loading a sample to a fixed level in tension, and subsequently determining the ultimate residual compressive strength. This type of testing is important, as any component in service would most likely be subjected to differing loading conditions.

The HMU/BSG composite samples showed no degradation in mechanical properties as a result of reversed mode loading. Initially, specimens were pre-loaded in tension at levels of 11, 46, and 68% of the UTS of the material (Table II-5). The first two loading levels were below the proportional limit of the composite, with the third level (68%) being slightly above the proportional limit. Subsequent compression testing to failure of these specimens showed no decrease in the UCS (compared to the baseline) regardless of the level of tensile pre-stressing (Table II-5). Pre-loading of samples in compression at levels of 24, 48, and 73% of the UCS followed by subsequent tensile testing to failure revealed no degradation in the UTS or elastic modulus of the composite. In fact, the UTS of the prestressed materials showed an increase of approximately 20% after prestressing in compression (Table II-5).

Table II-5 - Reversed Mode Mechanical Test Results for 0° HMU/BSG-2 Composites

<u>Initial Load (MPa)</u>	<u>Ultimate Load (MPa)</u>	<u>E (GPa)</u>
None (Monotonic test)	589 (UCS)	*
None (Monotonic test)	568 (UTS)	170
63 (tension/11% UTS)	752 (UCS)	190
264 (tension/46% UTS)	641 (UCS)	190
389 (tension/68% UTS)	704 (UCS)	175
142 (compression/24% UCS)	711 (UTS)	168
284 (compression/48% UCS)	697 (UTS)	168
428 (compression/73% UCS)	665 (UTS)	169

Evaluation of P-100/BSG composite specimens indicated a dependence of compressive pre-loading on the residual tensile properties of the material, but not vice versa. Tensile pre-loading was performed at levels of 24 and 46% of the UTS, followed by compressive loading to failure (Table II-6). Both of these loading levels occurred in the linear region of the stress-strain curve. No change in the residual compressive strength of the specimens was observed after tensile pre-loading, although the compressive elastic modulus increased. When specimens were pre-loaded in compression at levels of 28, 43, and 69% of the UCS, a significant decrease in the residual tensile strength was observed. As shown in Table II-6, the UTS of the P-100/BSG-2 materials decreased dramatically after compressive pre-loading compared to the monotonic UTS. However, no change in the residual tensile elastic modulus was observed after compressive pre-loading.

Table II-6 - Reversed Mode Mechanical Test Results for 0° P-100/BSG-2 Composites

<u>Initial Load (MPa)</u>	<u>Ultimate Load (MPa)</u>	<u>E (GPa)</u>
None (Monotonic test)	351 (UCS)	308
None (Monotonic test)	631 (UTS)	319
150 (tension/24% UTS)	334 (UCS)	344
293 (tension/46% UTS)	383 (UCS)	383
97 (compression/28% UTS)	351 (UTS)	333
150 (compression/43% UTS)	293 (UTS)	333
243 (compression/69% UTS)	277 (UTS)	331

When samples were pre-loaded in compression, stress-strain curves showed inelastic behavior. Figure II-20 shows a typical compression stress-strain curve obtained in the longitudinal direction during pre-loading. As can be seen, the curve exhibits hysteresis during the loading-unloading cycle. The hysteresis is thought to be an indication of an energy dissipation process occurring within the material during compressive pre-loading. Examples of such processes could be fiber-matrix interfacial sliding or slipping between individual graphite

planes within the carbon fiber. In both fiber systems, pre-loading to any level of compression prior to tensile testing resulted in this type of stress-strain behaviour, with the area of the curve being dependant on the level of pre-stressing.

The amount of energy dissipation within the composites during compressive pre-loading was calculated based on the area of the compression stress-strain hysteresis loop and the tested volume of each specimen. The calculated values of energy dissipation occurring within each specimen during compressive loading and unloading is shown in Table II-7. The HMU/BSG system withstood over seventy times (70x) the amount of energy dissipation in the P-100/BSG system without any degradation of the resultant tensile properties. For levels of energy dissipation as low as 2.1 mJ/cm³, the P-100 fiber composites showed a dramatic decrease in the residual tensile strength, while the HMU fiber system showed no degradation in tensile properties after having over 153 mJ/cm³ of compressive energy dissipated during pre-loading.

Table II-7 - Energy Dissipated During Compressive Pre-stressing of Composites Studied in Reversed Mode Loading

<u>Composite System</u>	<u>Initial Compressive Load (MPa)</u>	<u>Cross-Sectional Area (10⁻³ cm²)</u>	<u>Energy Dissipated per Unit Volume (mJ/cm³)</u>
HMU/BSG-2	142 (24% UCS)	67.7	4.0
	284 (48% UCS)	67.2	34.0
	428 (73% UCS)	67.3	153.8
P-100/BSG-2	97 (28% UCS)	71.1	2.1
	150 (43% UCS)	68.0	19.2
	243 (69% UCS)	69.2	46.9

The explanation of the dramatic differences in the levels of energy that can be dissipated in compressive pre-loading, both with and without degradation to the resultant tensile properties for the two materials can be found in the fibers themselves. As described earlier, HMU fiber has a disordered carbon structure, while P-100 fibers have a highly structured, radial sheet-like structure. Because of these structural differences, HMU fibers have higher compressive

strengths than P-100 fibers. During compressive testing, HMU fibers typically fail in a fiber buckling and kinking mode, requiring great amounts of strain. Pitch-based fibers such as P-100 fail in a classical shear fashion, leaving a 45° angle at the fracture surface. These shear failures require very little strain. PAN based fibers have been reported to have up to ten times the strain to compressive failure of P-100 fibers [18]. For HMU/BSG composites, the fibers respond to the induced strain during compressive loading by buckling or kinking. The glass matrix supports the fibers and prevents failure. In P-100 fiber reinforced materials, the fibers respond to the strain induced during compressive loading by shearing, even at very low loads. Shear bands are introduced into the fiber without completely failing it. Evidence that the fibers have not completely failed is seen in the unchanged tensile modulus measured during the subsequent tensile loading to failure. The shear bands act as defects when loaded in tension, however, leading to a decrease in the residual tensile strength of the specimen after compressive pre-loading. Evidence of shear damage in the fibers is seen in scanning electron micrographs of the tensile fracture surfaces of the pre-stressed specimens. Figure II-21 compares tensile fracture surfaces of monotonic specimens and specimens after compression pre-stressing. In the pre-stressed material, a great many more shear failures are seen in the fibers, evidence of damage induced during the compressive pre-stressing as described above.

The results of cyclic testing and fatigue testing (described previously), together with the results of reversed mode testing combine to demonstrate the various critical functions that the carbon fiber or the glass matrix perform during composite loading. In tensile loading, the fiber controls the ultimate properties of the composite, not the matrix. Composite specimens that have been stressed such that the fibers are damaged (compression loaded), show a dramatic decrease in the tensile properties. During compressive loading, no effect is seen for either pre-tensile or pre-compressive loaded materials. In a compression test, the matrix contributes significantly to the UCS by supporting the fiber such that even specimens with damaged fibers still maintain the UCS of unstressed materials.

II.4.8 High Temperature Behavior

The ability of C/Glass composites to maintain mechanical performance at elevated temperatures in a non-oxidizing atmosphere such as space is dependent on the inherent temperature capability of the glass or glass-ceramic matrix. In order to fully evaluate high temperature composite properties, it is usually necessary to employ both flexural and tensile testing. Flexural testing provides a better indication of matrix integrity at temperature because it provides a means of highly stressing the matrix in shear. Tensile testing furnishes information on fiber strength, elastic modulus, and environmental stability at elevated temperature. Composites in the HMU/BSG system have been shown to retain their flexural and tensile

strength and stiffness in argon and air (for short times) up to a temperature of 560°C, corresponding to softening and relaxation of the BSG matrix [19]. BMAS glass-ceramic matrix composites unidirectionally reinforced with FT700 carbon fiber have demonstrated full retention of flexural strength in argon up to a temperature of 1200°C (Figure II-22). Post-test examination of samples tested at 1200°C indicated that the samples had failed in tension, with no indication of any plastic deformation induced during testing. Higher temperatures result in plastic deformation due to viscous flow of the residual glassy phase that still exists after crystallization of the matrix.

A limited amount of short-time flexural creep testing was performed on samples from the FT700/BMAS system at temperatures ranging from 1000°C to 1200°C in argon to determine the time dependent deformation behavior of this material. Samples were held at constant stress levels of 240 MPa and 480 MPa for one hour at temperature and then examined for signs of plastic deformation. Mid-span deflection was monitored throughout the duration of the test. Table II-8 shows the results of the very limited amount of testing that was performed. Up to a temperature of 1100°C, a stress level of 240 MPa resulted in no permanent deformation after one hour. The higher stress level of 480 MPa resulted in slight deformation after one hour at 1100° and 1200°C, with approximately 0.10 mm and 0.13 mm of permanent mid-span deflection, respectively. These preliminary results suggest that BMAS matrix composites are quite resistant to short-time creep up to 1150°C at moderate stress levels (at least up to 240 MPa).

Table II-8 - Flexural Creep Behavior in Argon of 0° FT700/BMAS Composites

<u>Temperature (°C)</u>	<u>Stress Level (MPa)</u>	<u>Mid-Span Deflection* (mm)</u>	<u>Comments</u>
1000	240	0	No deformation
1100	240	0	No deformation
1100	480	0.10	Slightly deformed
1150	240	0	No deformation
1200	480	0.12	Slightly deformed

* After one hour at temperature

As stated previously, it is clear that under inert atmosphere conditions composite failure is solely a function of the temperature capability of the matrix. Under oxidizing conditions, however, oxidation of the carbon fiber becomes an issue. In a previous study, strength loss in

unstressed unidirectionally reinforced HMU/BSG composites became noticeable after approximately 100 hours at temperatures above 450°C [20]. Under applied stress, strength degradation was found to take place more rapidly. Factors affecting the rate of strength loss are numerous, but consist mainly of the level of applied stress, specimen geometry, and fiber architecture within the composite. The primary mechanism for strength loss was found to be oxidation of carbon fiber in a direction normal to the fiber direction, *i.e.* oxidation from the sides and faces of the composite. The effective load-bearing cross-section of the composite became gradually smaller as oxidation progressed. More recent work at UTRC has shown that fiber coatings can significantly reduce the transverse oxidation rate in HMU/BSG composites at a temperature of 450°C, which translates to slower rate of strength loss. Composites in the FT700/BMAS system have been evaluated for flexural strength in air at temperatures up to 1200°C. Figure II-23 summarizes the results of this evaluation, and for comparison also shows the strength of the same material tested in argon. The numbers in parentheses next to each data point for the air testing indicates the length of time that the sample was exposed to a temperature above 800°C prior to being tested. It is clear from these results that strength degrades rapidly at these high temperatures, solely due to oxidation of the carbon fiber.

Higher temperature oxidation behavior under stress (stress rupture) has also been evaluated for 0° reinforced FT700/BMAS composites. Prior to the stress rupture evaluation, the inherent flexural strength of the material in argon at 800°C was determined to be 1170 MPa. Samples were then loaded in a 3-point flexural configuration and held at constant stress levels of 172, 345, 517, and 690 MPa in air at a temperature of 800°C until failure. Each sample that was evaluated had a thickness of approximately 1.8 mm and had been machined only along the longer edge faces. The time to failure at each stress level is shown graphically in Figure II-24. It is clear that the time to failure decreases with an increasing level of applied stress. This was the expected trend based on the strength degradation mechanism previously described for the HMU/BSG system. A similar oxidation mode was observed in the FT700/BMAS samples, *i.e.* transverse oxidation was the primary mechanism of strength degradation. The fact that the composites could last for more than one hour at 800°C at stress levels up to 345 MPa was thought to be fairly remarkable. This suggests that these materials may be candidates for limited life applications such as missile components. Samples with a larger cross-section or containing coated fiber could be expected to exhibit even longer life under similar loading conditions.

II.5. THERMOPHYSICAL PROPERTIES

II.5.1 Thermal Expansion

A requirement of nearly all space structures is that they exhibit low values of thermal expansion and a high level of dimensional stability so that any change in dimension due to temperature fluctuations during orbit is minimized. Because of the low coefficient of thermal expansion (CTE) values of carbon fiber and the glass matrices, C/Glass composites offer the potential of obtaining extreme dimensional stability and a near-zero CTE over a wide temperature range.. Since carbon fiber has a negative axial CTE (up to a temperature of 400 to 500°C), a resultant in-plane composite CTE of very close to zero is achievable by combining the fibers with a matrix which has a positive CTE, such as glass. Through control of fiber orientation and fiber content, it is possible to tailor thermal expansion behavior to achieve composites whose in-plane CTE is nearly zero over a wide temperature range. Figure II-25 shows the in-plane thermal strain as a function of temperature for a quasi-isotropic $[0/\pm 60^\circ]$ reinforced HMU/BSG composite over the temperature range of interest for most space applications (-150°C to +100°C). The curve is essentially flat over the entire temperature range, indicating a near-zero CTE, with less than 15×10^{-6} cm/cm hysteresis over the entire thermal cycle. This exceptional combination of near-zero CTE and extreme dimensional stability makes HMU/BSG composites potential candidates to replace monolithic glasses and polymer matrix composites for large space based mirrors and optical structures [21].

The thermal expansion behavior of C/Glass composites containing high modulus pitch-based carbon fibers has also been characterized since these materials will be necessary for stiffness-critical applications in space. The thermal strain behavior of unidirectionally reinforced P-100/BSG and FT700/BSG composites is characterized by closed hysteresis loops and shows similar levels of hysteresis as that of the HMU/BSG composite described above, with values of less than 25×10^{-6} cm/cm over the entire thermal cycle (Figure II-26). The more negative axial CTE for the high modulus pitch based fibers results in composite CTE's being more negative than those of HMU-reinforced composites, varying from approximately -1.1 to -0.75×10^{-6} cm/cm K over the temperature range of -150°C to +100°C. This compares with a CTE range of -0.5 to -0.25×10^{-6} cm/cm K for unidirectionally reinforced HMU/BSG composites of similar fiber content (Figure II-27). Even though these ranges of composite CTE for the P-100/BSG and FT700/BSG composites are somewhat negative, they still fall within an acceptable CTE window for many space-related structures. As an example, many satellite truss structures require high stiffness materials with CTE's that can vary from -1.4 to $+1.4 \times 10^{-6}$ cm/cm K over the temperature range of -150 to +100°C [10]. Unidirectionally reinforced P-100/BSG and FT700/BSG composites definitely satisfy both of these criteria.

The in-plane CTE of P-100/BSG and FT700/BSG composites can be brought closer to zero by going to an angle-ply configuration in a similar manner as the HMU/BSG composite described previously. However, going to the off-axis orientation required for zero CTE drastically reduces the in-plane elastic modulus, thereby defeating the original purpose for using the high modulus fiber. Preserving high composite stiffness is imperative for many space-based structures. One means of achieving this combination of high stiffness and near-zero CTE that has been developed at UTRC is to incorporate a second high modulus fiber with a positive CTE into the composite microstructure [22]. Boron and silicon carbide monofilaments have both been successfully combined with P-100 fiber to create a dual fiber reinforced glass matrix composite possessing a combination of high elastic modulus and near-zero CTE. Figure II-27 shows the CTE as a function of temperature for one of these dual fiber reinforced glass matrix composites along with the CTE curves for a P-100/BSG and a HMU/BSG composite. This is a good example of the remarkable tailorability afforded by the wide variety of fibers that can be used for fiber reinforced glass matrix composites.

II.5.2 Thermal Fatigue Behavior

One issue of concern when using C/Glass composites for space structures is the degree of stability in the mechanical properties of the composites after being subjected to a large number of thermal cycles during months of orbiting in space. In order to assess the sensitivity of C/Glass composites to thermal fatigue, unidirectional and [0/90] reinforced composites in the HMU/BSG and P-100/BSG systems were evaluated for tensile strength, elastic modulus, and PL stress after being subjected to as many as 2000 thermal cycles from -50°C to $+150^{\circ}\text{C}$. This temperature range was selected to simulate a typical thermal fluctuation during orbit. Table II-9 shows the results of thermal fatigue on the mechanical properties after 500 and 2000 thermal cycles. Each value is the average of either two (0 cycles) or three (500 and 2000 cycles) mechanical tests.

For three of the four C/Glass systems (0° HMU/BSG, 0° P-100/BSG, 0/90 P-100/BSG), there was a significant decrease in the PL stress after either 500 or 2000 thermal cycles compared to the as-fabricated material. This behavior can be explained by considering the strains that are being established between the matrix and fiber during thermal cycling due to their difference in thermal expansion behavior. Over the course of several hundred or more thermal cycles, this strain can lead to gradual degradation of the fiber-matrix interface and a weakening of the bond at the interface. This decrease in interfacial strength would lead to a reduction in PL stress. Also playing a role could be cracking of the matrix during thermal cycling due to these same thermal expansion mismatch effects. The surface of one sample from each composite system was observed microscopically after every 500 thermal cycles to document any matrix microcracking that may be accumulating during the test. In several cases, an increase in the amount of

microcracking could be observed with a higher number of thermal cycles.

Also evident from the data presented in Table II-9 is that in the two 0° reinforced systems, there is an increase in ultimate tensile strength for samples that have undergone some degree of thermal cycling. In the 0° HMU/BSG system, the average UTS increased noticeably after 500 cycles, and again after 2000 thermal cycles. In the 0° P-100/BSG system, the increase was more significant and appeared to take place during the initial 500 cycles, with no additional increase noted after 2000 thermal cycles. This effect is believed to be real since it was observed in all of the specimens that were evaluated. The explanation is thought to again be related to thermal strains/stresses, but this time in a slightly different manner. Residual thermal stresses that are built up during cooling of the composites from the fabrication temperature result in the fibers being placed in a state of residual compression. Thermal cycling may serve to relieve some of this residual stress by weakening the fiber-matrix interface and allowing the fibers to "relax".

Table II-9 - Thermal Fatigue Mechanical Test Results for HMU/BSG
and P-100/BSG Composites

<u>Composite System</u>	<u>Number of Thermal Cycles</u>	<u>Ave. Ult. Tensile Stress (MPa)</u>	<u>Ave. Elastic Modulus (GPa)</u>	<u>Ave. PL Stress (MPa)</u>
0° HMU/BSG	0	435	167	333
	500	488	171	289
	2000	528	167	67
[0/90] HMU/BSG	0	280	90	56
	500	320	88	54
	2000	323	88	51
0° P-100/BSG	0	524	371	431
	500	680	371	122
	2000	665	377	112
[0/90] P-100/BSG	0	359	203	141
	500	331	188	121
	2000	360	203	50

II.5.3 Thermal Conductivity

One of the unique characteristics of carbon fiber is the extremely high thermal conductivity that exists along the direction of the fiber. The fiber data summarized earlier in Table II-1 includes information on axial thermal conductivity. Thermal conductivity is another property that is strongly dependent on the internal microstructure of the fiber, with the two most important factors being crystallite size and the degree of crystallite orientation [1]. It can be seen in the table that the ultra-high modulus pitch based carbon fibers approach or exceed the thermal conductivity of copper (400 W/m K). In fact, a carbon fiber under development at Amoco Performance Products (K1100X) for the Navy exhibits an axial thermal conductivity nearly three times that of copper (1030-1100 W/m K).

Power generation systems in space will require the expulsion of waste heat, typically envisioned as being accomplished through a system of high thermal conductivity radiator fins [23-24]. C/Glass composites have been identified as a candidate material for radiator fins because of their high strength and stiffness, inherent space environmental durability, thin-gage fabrication capability, and the potential for high in-plane thermal conductivity (the trade study will be described in a subsequent section of this report). To demonstrate the potential of glass matrix composites containing the very highest thermal conductivity carbon fiber, unidirectionally reinforced K1100X/BSG composites were fabricated and tested. Samples of K1100X fiber were supplied to UTRC by Amoco Performance Products at the request of the Naval Surface Warfare Center. The unusual structure of the K1100X fiber can be seen in Figure II-28, which shows a picture of the composite microstructure. The split "Pac-Man" structure is prevalent in the majority of the fibers and arises during fiber manufacture due to thermal stresses generated in the fiber during cooling. Despite the split fiber structure, the tensile stress-strain behavior of the K1100X/BSG composite was very similar to that of P-100/BSG composites described in a previous section. The non-linear shape of the stress-strain curve (Figure II-29) was nearly identical to that shown in Figure II-3 for P-100/BSG, with values of tensile strength ranging from 470 to 515 MPa and the elastic modulus being in the range of 360 GPa for a composite containing 41 volume % fiber. The degree of fiber pullout observed on the fracture surface of the K1100X/BSG composite is considerably greater than that typically observed in a P-100/BSG composite, presumably indicating comparable or even higher toughness. The difference is thought to be related to the more highly aligned fiber structure which results in significant shearing of the fiber during composite tensile fracture.

The thermal conductivity characteristics of several C/Glass composites was assessed in the in-plane fiber direction and the through-thickness direction using a laser flash technique. Composites evaluated were [0/90] reinforced HMU/BSG, 0° reinforced P-100/BSG, and 0° reinforced K1100X/BSG. Figure II-30 shows the results of the measured in-plane thermal

conductivities as a function of temperature as well as the calculated room temperature conductivities for the three composites. The calculated values were obtained using a standard rule-of-mixtures approach. For the HMU/BSG composite, the agreement between the measured and calculated values is excellent. However, the measured values for the P-100/BSG and K1100X/BSG composites are only about 75-80% of the theoretical values, suggesting that some damage may have occurred to these high modulus fibers during fabrication. With respect to the measured thermal conductivities, of note is that the specific in-plane thermal conductivity (thermal conductivity/density) of the P-100/BSG composite is approximately twice the specific thermal conductivity of copper. Also measured was the through-thickness thermal conductivity, which was predictably quite low (2 W/m K) due to the insulating qualities of the glass matrix.

II.6. SPACE ENVIRONMENTAL DURABILITY

One of the most crucial requirements of materials to be utilized in space-based applications is that they be resistant to the rigors of the space environment. Atomic oxygen, micrometeoroids and orbital debris, solar radiation, and thermal cycling are but a few of the environmental factors that can seriously damage materials in space. The effects of atomic oxygen (AO) on carbon-containing materials in space can be especially severe. Erosion due to AO is a line-of-sight process, meaning that only material that is directly impinged by AO is affected. AO species are highly energetic and rapidly react with oxidizable materials, especially those that are carbon-based, in the temperature regime of the space environment. Analysis of carbon fiber reinforced polymer materials that have been exposed in low earth orbit has revealed that AO attack leads to significant erosion of both the epoxy matrix and the carbon fibers [25], with the formation of a cone-like surface morphology resulting from the release of volatile oxidation products. Most metal and ceramic materials have shown extreme stability when exposed to similar conditions, with erosion yields of less than $0.02 \times 10^{-24} \text{ cm}^3/\text{atom}$ compared with erosion yields greater than $1 \times 10^{-24} \text{ cm}^3/\text{atom}$ for carbon and polymer-based materials [25].

C/Glass composites were exposed to the space environment for a period of nearly 6 years aboard the Long Duration Exposure Facility (LDEF) satellite. The LDEF satellite was placed in low earth orbit by the shuttle orbiter Challenger in April of 1984 and was retrieved by the shuttle orbiter Columbia in January of 1990. The LDEF satellite was situated in a stable orbit with the cylindrical axis Earth pointing and the same edge always facing in the direction of the velocity vector. The purpose of the experiment was to expose potential spacecraft and satellite materials to the space environment in a controlled fashion, such that materials placed in a "leading edge" or "trailing edge" orientation would remain that way for the duration of the experiment. C/Glass composite materials were located in both leading edge (Row 8) and trailing edge (Row 4)

positions, with end-of-mission AO fluences for those positions being 6.93×10^{21} atoms/cm² and 9.32×10^4 atoms/cm², respectively.

Analysis of the C/Glass composites, performed at UTRC under corporate funding, indicated that they experienced negligible weight loss resulting from fiber erosion, with no change in flexural strength or thermal expansion behavior [26]. Figure II-31 shows optical micrographs of a polished cross-section of a C/Glass composite that was exposed on the leading edge (Row 8) of LDEF. A coating of nickel was deposited on the surface of the composite prior to sectioning and polishing to fill in and decorate any voids present due to carbon fiber that had been eroded away by AO. The micrographs clearly show that only fiber that was exposed at the surface of the samples (due to polishing) was eroded away, with the glass matrix providing excellent protection for interior fibers. In fact, even fibers near the surface that were covered by only a thin layer ($< 5 \mu\text{m}$) of glass were fully intact following exposure. This inherent resistance to the effects of AO suggests that C/Glass composites will not require additional protective measures, such as coatings, making them very attractive for space applications requiring long-term durability.

II.7. SUMMARY

Carbon fiber reinforced glass matrix composites have been developed which exhibit an outstanding combination of mechanical performance, high temperature capability, low density, near-zero thermal expansion, dimensional stability, and space environmental durability. The ability to choose from different fibers, a variety of matrices, and different ply orientations affords a remarkable degree of tailorability to these C/Glass composite materials. These attributes combine to make C/Glass composites an excellent candidate for many space-based structural applications.

REFERENCES

1. W. Johnson, "The Structure of PAN Based Carbon Fibres and Relationship to Physical Properties"; pp. 389-473 in *Handbook of Composites, Volume 1 - Strong Fibres*. Edited by W. Watt and B. V. Perov. Elsevier Science Publishers B. V., Amsterdam, 1985.
2. B. Rand, "Carbon Fibres from Mesophase Pitch"; pp. 495-575 in *ibid.*.

3. W. K. Tredway, K. M. Prewo and C. G. Pantano, "Fiber-Matrix Interfacial Effects in Carbon Fiber Reinforced Glass Matrix Composites," *Carbon*, **27** (1989) 717-727.
4. W. K. Tredway, C. G. Pantano and G. Chen, "Influence of Matrix Wetting on The Fiber-Matrix Interfacial Strength and Subsequent Performance of Carbon Fiber Reinforced Glass Composites," presented at the 93rd Annual Meeting of the American Ceramic Society, Cincinnati, OH, April 28-May 2, 1991.
5. K. M. Prewo, J. J. Brennan and G. K. Layden, "Fiber Reinforced Glasses and Glass-Ceramics for High Performance Applications," *Am. Ceram. Soc. Bull.*, **65** (1986) 305-313.
6. J. J. Brennan, "Glass and Glass-Ceramic Matrix Composites"; pp. 222-259 in *Fiber Reinforced Ceramic Composites: Materials, Processing and Technology*. Edited by K. S. Mazdiasni. Noyes Publications, Park Ridge, New Jersey, 1990.
7. W. K. Tredway and P. H. McCluskey, "Compression Testing of Continuous P-100 Fiber Reinforced Glass Matrix Composite Tubes," UTRC Contract Report R91-917981-1, Office of Naval Research Contract N00014-89-C-0046, October 1, 1991.
8. V. C. Nardone and K. M. Prewo, "Tensile Performance of Carbon-Fibre-Reinforced Glass," *J. Mater. Sci.*, **23** (1988) 168-180.
9. R. Y. Kim and N. J. Pagano, "Crack Initiation in Unidirectional Brittle-Matrix Composites," *J. Am. Ceram. Soc.*, **74** (1991) 1082-1090.
10. D. Volk, C. F. Yen and K. Buesking, "Structural Development of Fiber Reinforced Glass Matrix Composites," Materials Sciences Corporation Contract Report MSC TFR 2112/8601, Office of Naval Research Contract N00014-89-C-0211, June, 1990.
11. W. K. Tredway and K. M. Prewo, "Carbon Fiber Reinforced Glass Matrix Composites for Structural Space Based Applications," UTRC Contract Report R89-917704-1, Office of Naval Research Contract N00014-85-C-0332, July 31, 1989.
12. D. Hull, *An Introduction to Composite Materials*, Cambridge University Press, Cambridge, Great Britain, 1981.

13. V. S. Avva, North Carolina A&T State University, 1987, personal communication.
14. J. W. Holmes, University of Michigan, 1991, personal communication.
15. W. K. Tredway and K. M. Prewo, "Carbon Fiber Reinforced Glass Matrix Composites for Space Based Applications," UTRC Contract Report R87-917470-1, Office of Naval Research Contract N00014-85-C-0332, August 30, 1987.
16. *SDS Spacecraft Structural Composite Materials Selection Guide*, prepared by Ketema, Inc., Composite Materials Division, for WPD L502, AFWAL, Materials Laboratory, WPAFB, May, 1989.
17. J. M. Prandy and H. T. Hahn, "Compressive Strength of Carbon Fibers," *SAMPE Quart.*, **22** (1991) 47-52.
18. M. G. Dobb, D. J. Johnson and C. R. Park, "Compressional Behaviour of Carbon Fibers," *J. Mater. Sci.*, **25** (1990) 829-834.
19. K. M. Prewo, "Carbon Fibre Reinforced Glass Matrix Composite Tension and Flexure Properties," *J. Mater. Sci.*, **23** (1988) 2745-2752.
20. K. M. Prewo and J. A. Batt, "The Oxidative Stability of Carbon Fibre Reinforced Glass-Matrix Composites," *J. Mater. Sci.*, **23** (1988) 523-527.
21. K. M. Prewo and E. Minford, "Thermally Stable Composite (TSC™) - Graphite Fiber Reinforced Glass for Dimensionally Stable Applications," Proc. of SPIE, Vol. 505, *Advances in Optical Materials*, San Diego, California, August, 1984, pp. 188-191.
22. W. K. Tredway and K. M. Prewo, "Development of Dual Fiber Reinforced Glass Matrix Composites for Structural Space Based Applications," UTRC Contract Report R90-917886-1, Office of Naval Research Contract N00014-88-C-0251, May 31, 1990.
23. T. Mahefkey, "Thermal Management Issues and Technology Needs for SDI," *AIAA 22nd Thermophysics Conference*, Honolulu, Hawaii, 1987, Paper AIAA-87-1478.
24. A. Choudhury and G. Peterson, "A Review of Advanced Radiator Technologies for Spacecraft Thermal Control," *AIAA/ASME 5th Joint Thermophysics and Heat Transfer Conference*, Seattle, WA, 1990, Paper AIAA 90-1706.

25. B. A. Banks, et al., "Atomic Oxygen Effects on Materials," *NASA/SDIO Space Environmental Effects on Materials Workshop*, Hampton, VA, 1988, NASA CP-3035, pp. 197-239.
26. W. K. Tredway and K. M. Prewo, "Analysis of the Effect of Space Environmental Exposure on Carbon Fiber Reinforced Glass," UTRC Internal Report R91-112542-4, May 31, 1991.

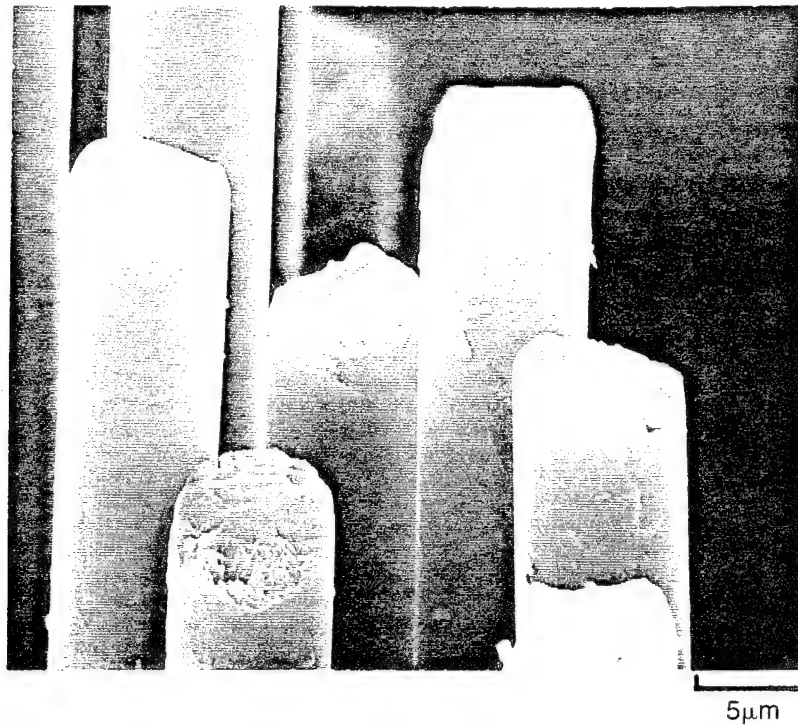


Figure II-1 (a). Structure of Hercules HMU Carbon Fiber

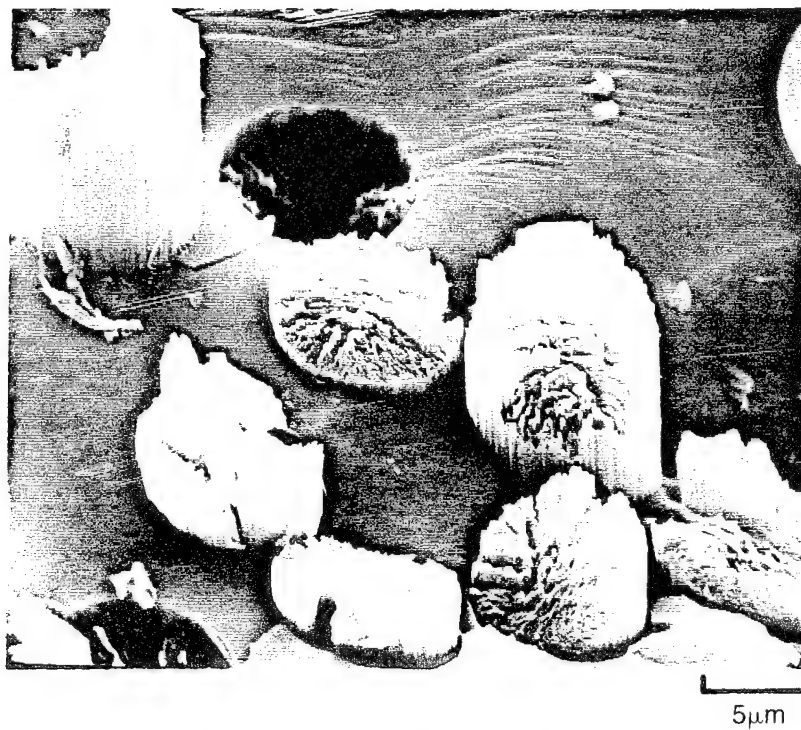


Figure II-1 (b). Structure of Amoco P-100 Carbon Fiber

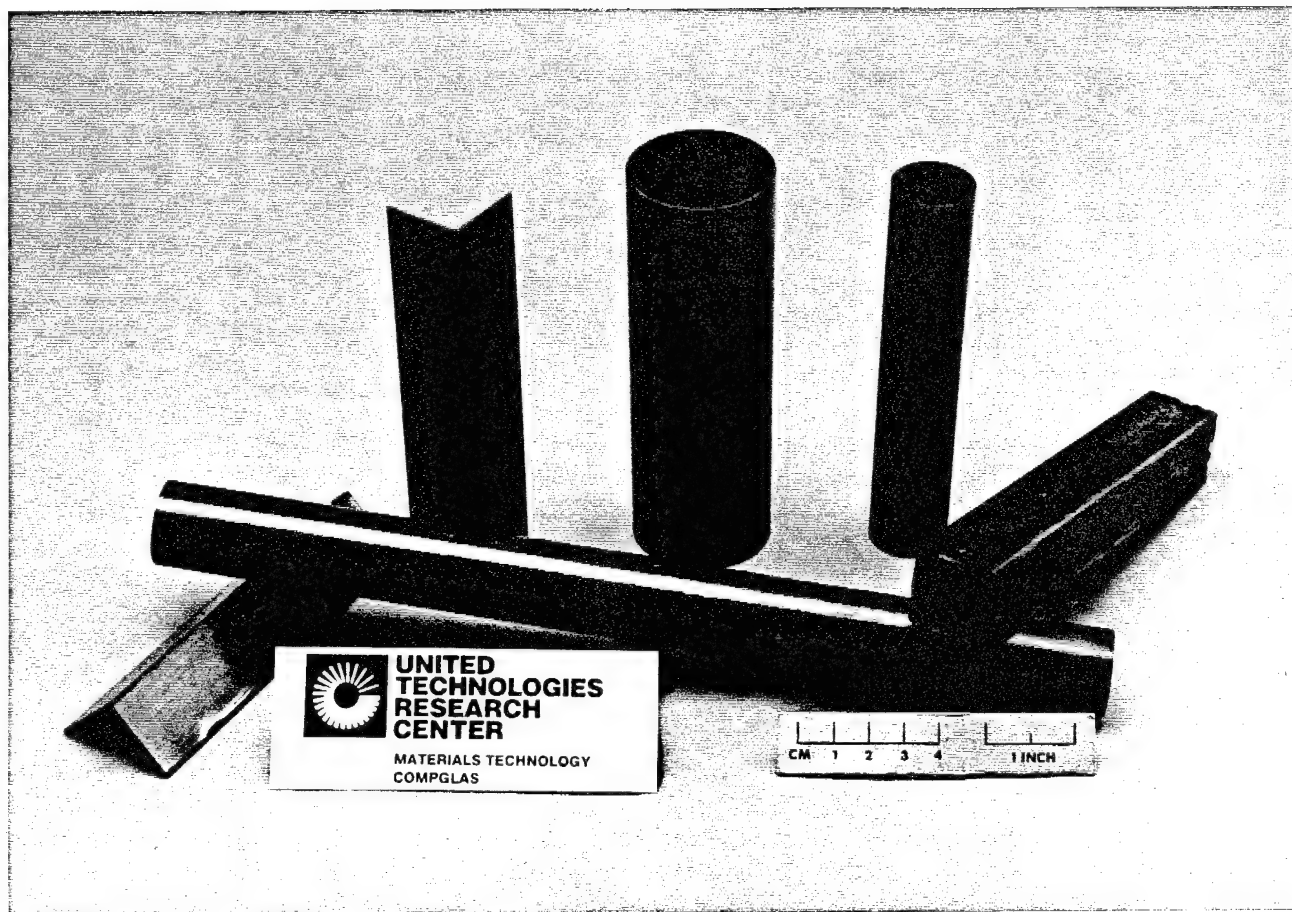


Figure II-2(a). Carbon Fiber Reinforced Glass Components Fabricated Using Hot Isostatic Pressing (HIP). The Components Shown Are Examples Of Circular And Square Cross-Section Tubes As Well As L-Beams. The Lengths Of The Components Shown Varies From 15 cm To 30 cm.

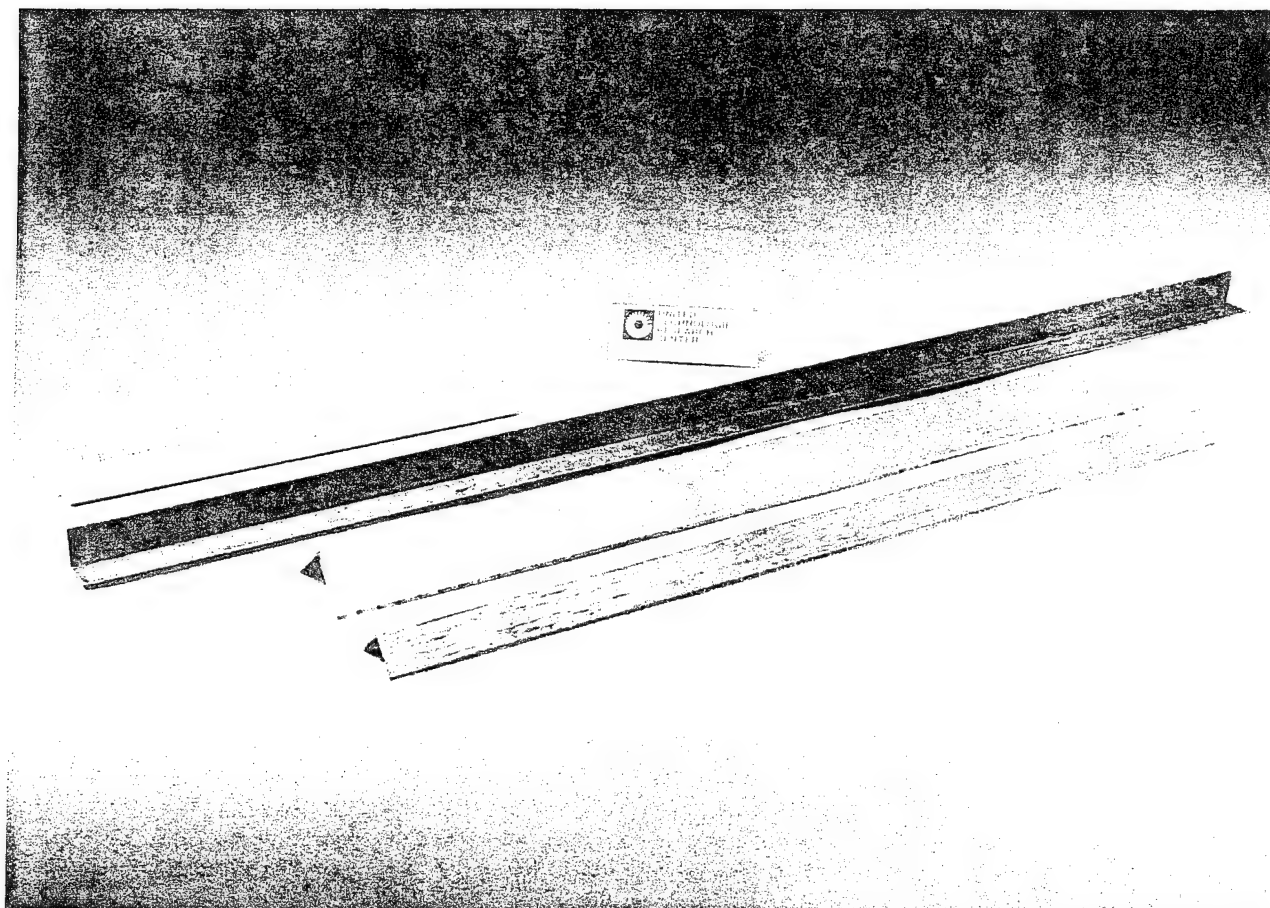


Figure II-2(b). Carbon Fiber Reinforced Glass Components Fabricated Using Hot Isostatic Pressing (HIP). These L-Beam Components Are 61 cm And 91 cm In Length.

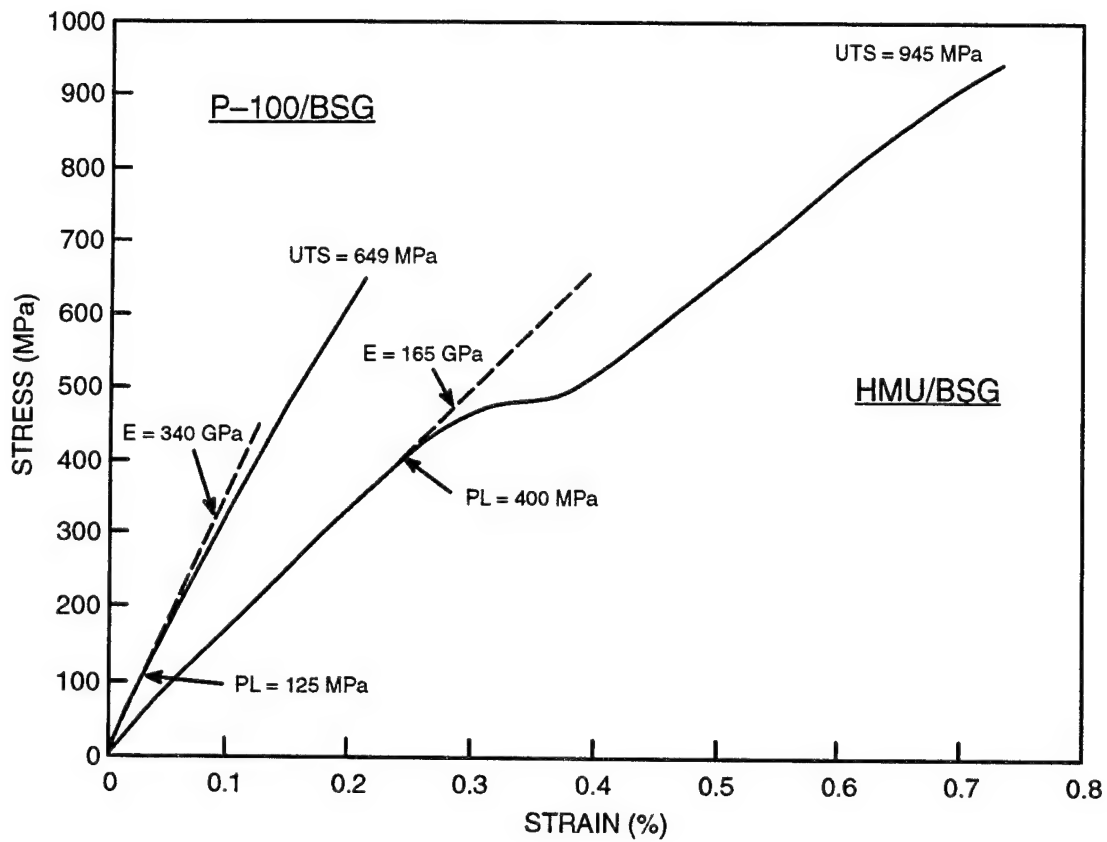


Figure II-3. Tensile Stress-Strain Behavior of 0° Reinforced P-100/BSG and HMU/BSG Composites

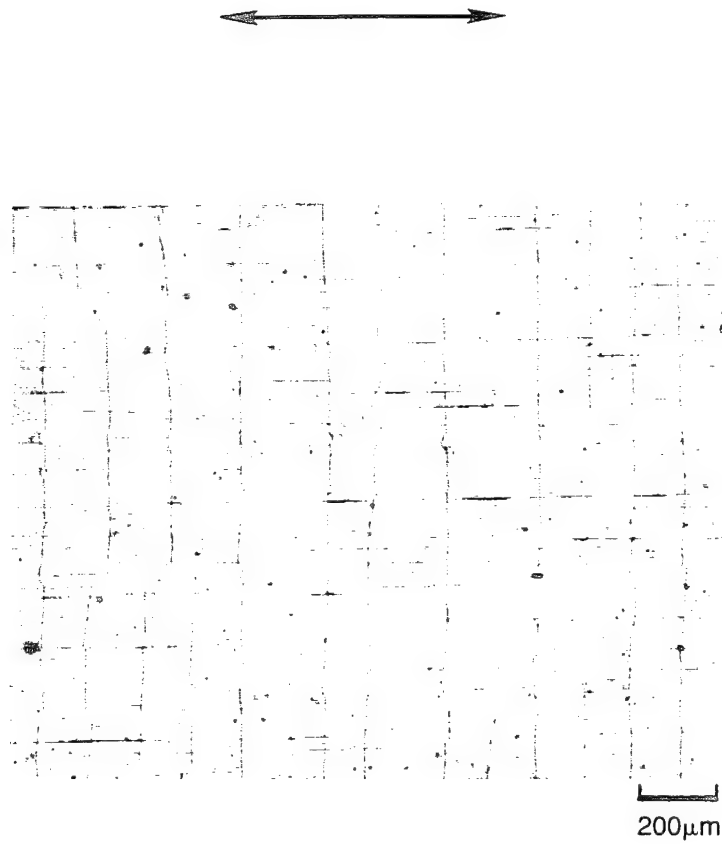


Figure II-4. Replica of the Surface of a 0°-Reinforced P-100/BSG Composite Showing Matrix Microcracks Formed Due to Thermal Residual Stress. The Arrow Indicates the Fiber Direction.

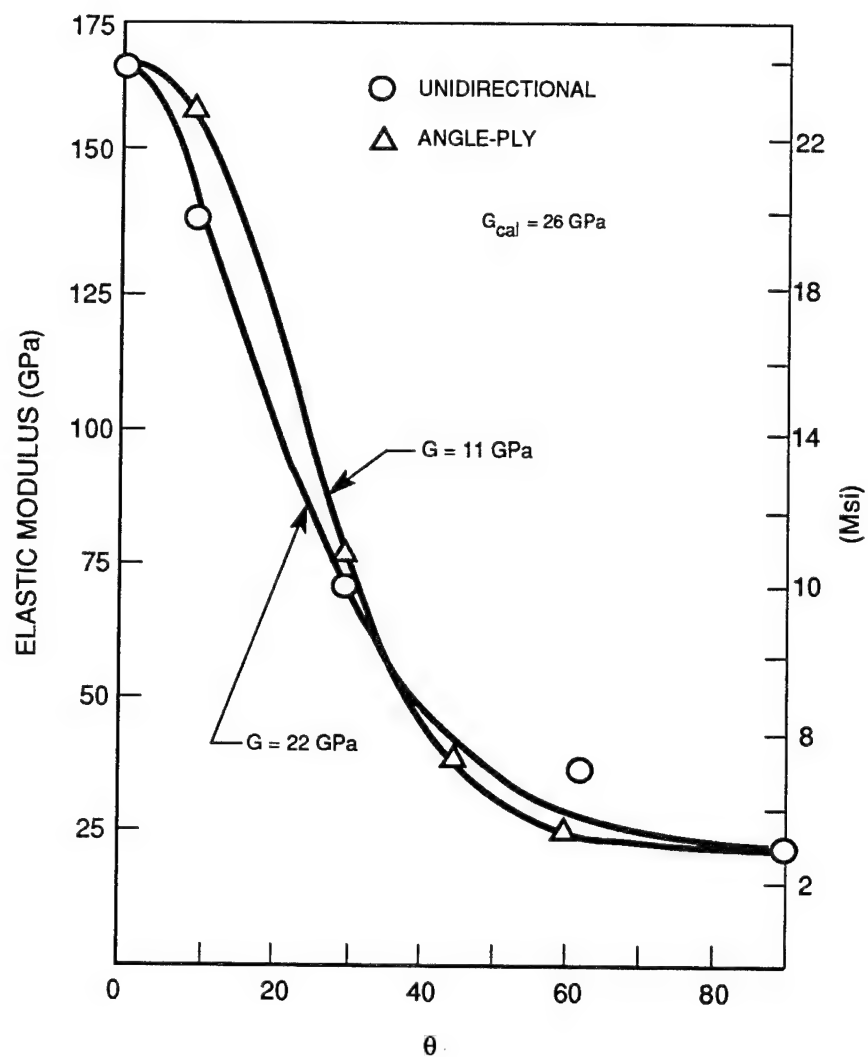


Figure II-5. Comparison of Measured and Calculated Elastic Modulus Values for Unidirectional and Angle-Ply 43 v/o HMU/BSG Composites

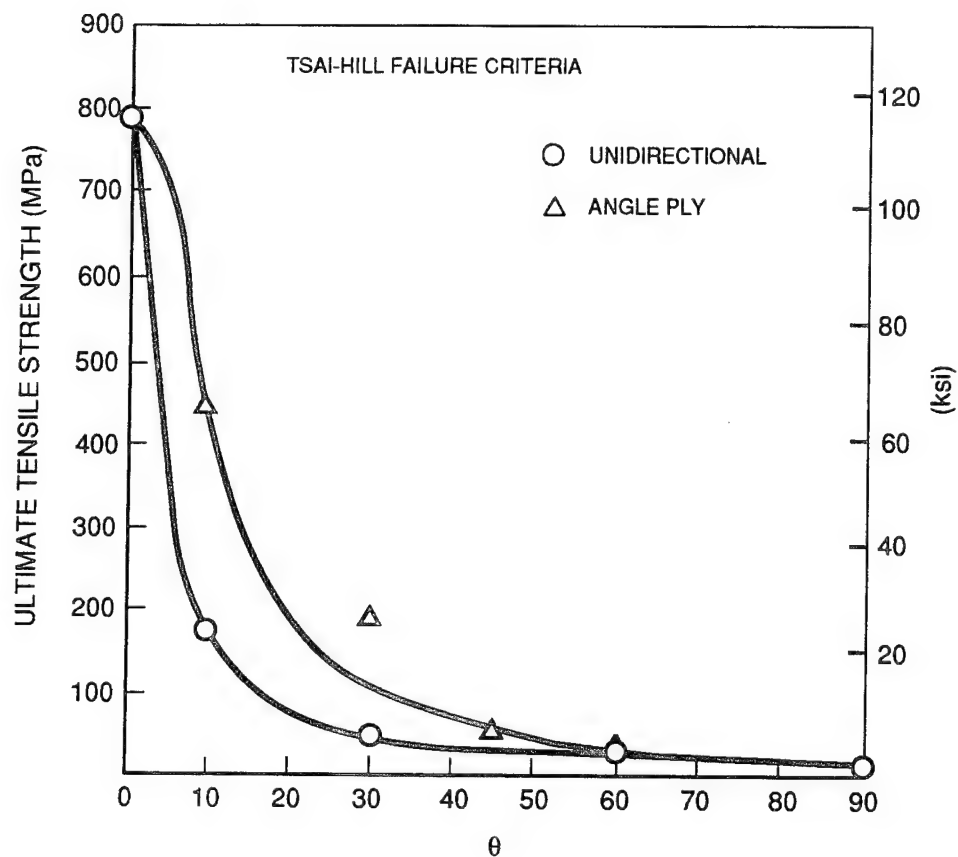


Figure II-6. Comparison of Measured and Predicted Strength of Unidirectional and Angle-Ply 43 v/o HMU/BSG Composites

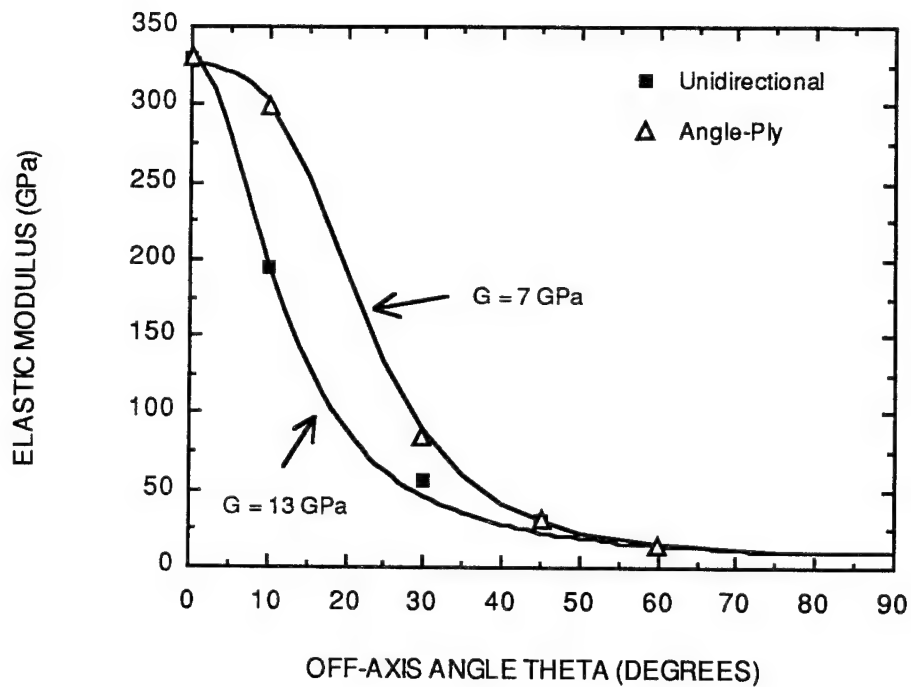


Figure II-7. Comparison of Measured and Predicted Elastic Modulus of Unidirectional and Angle-Ply FT700/BSG Composites

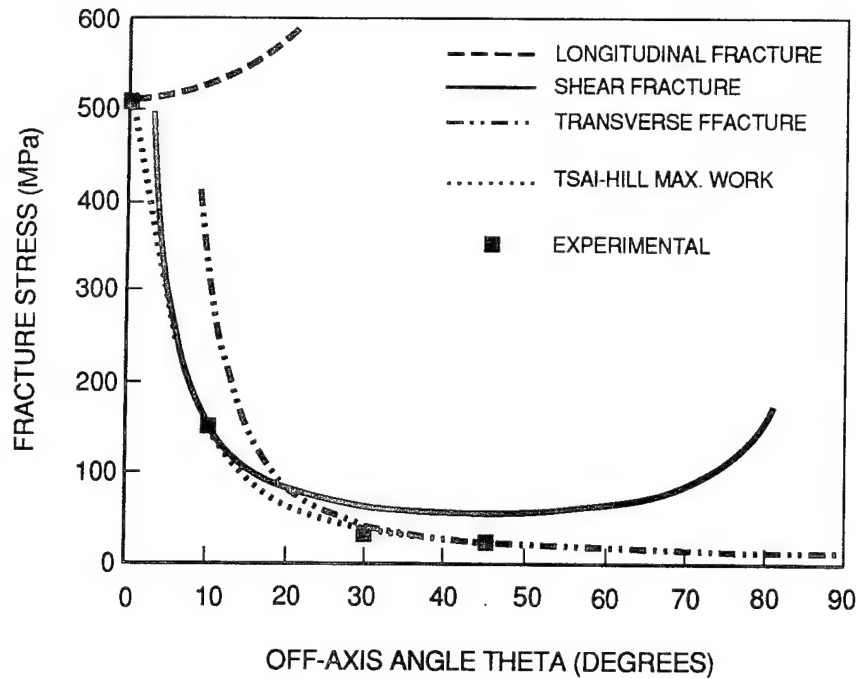


Figure II-8a. Comparison of Measured and Predicted Strength of Unidirectional FT700/BSG Composite

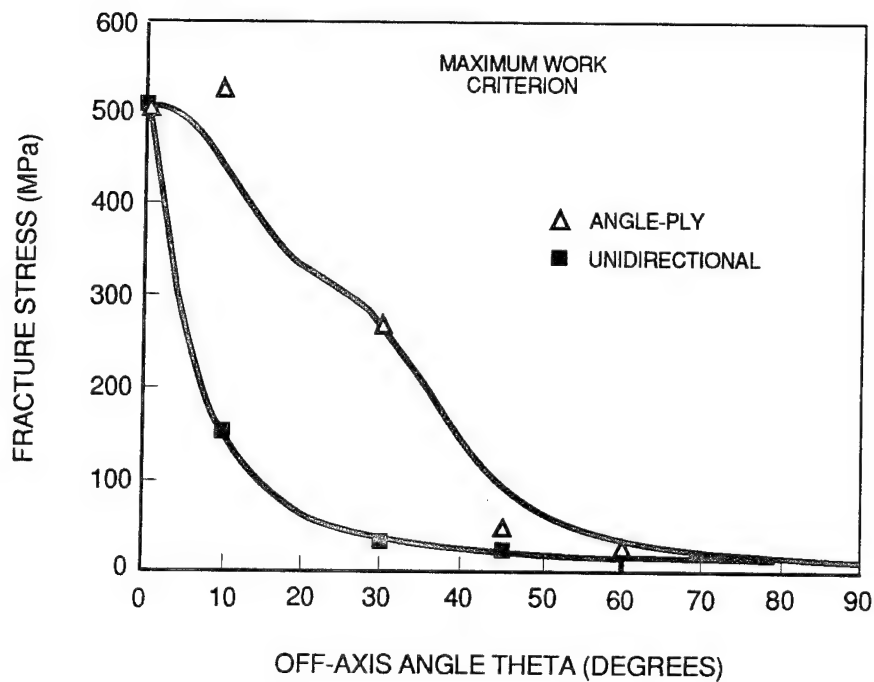


Figure II-8b. Comparison of Measured and Predicted Strength of Unidirectional and Angle-Ply FT700/BSG Composites Using Maximum Work Criterion

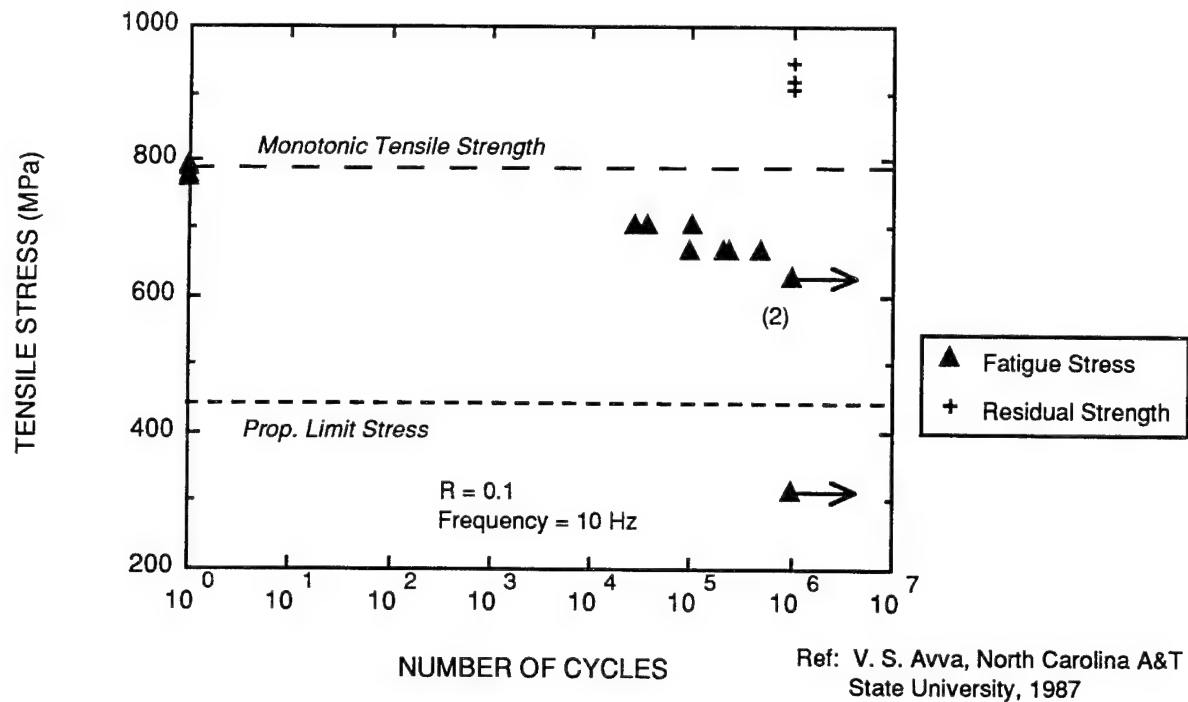


Figure II-9. Tensile Fatigue Behavior of Unidirectional HMU/BSG Composites

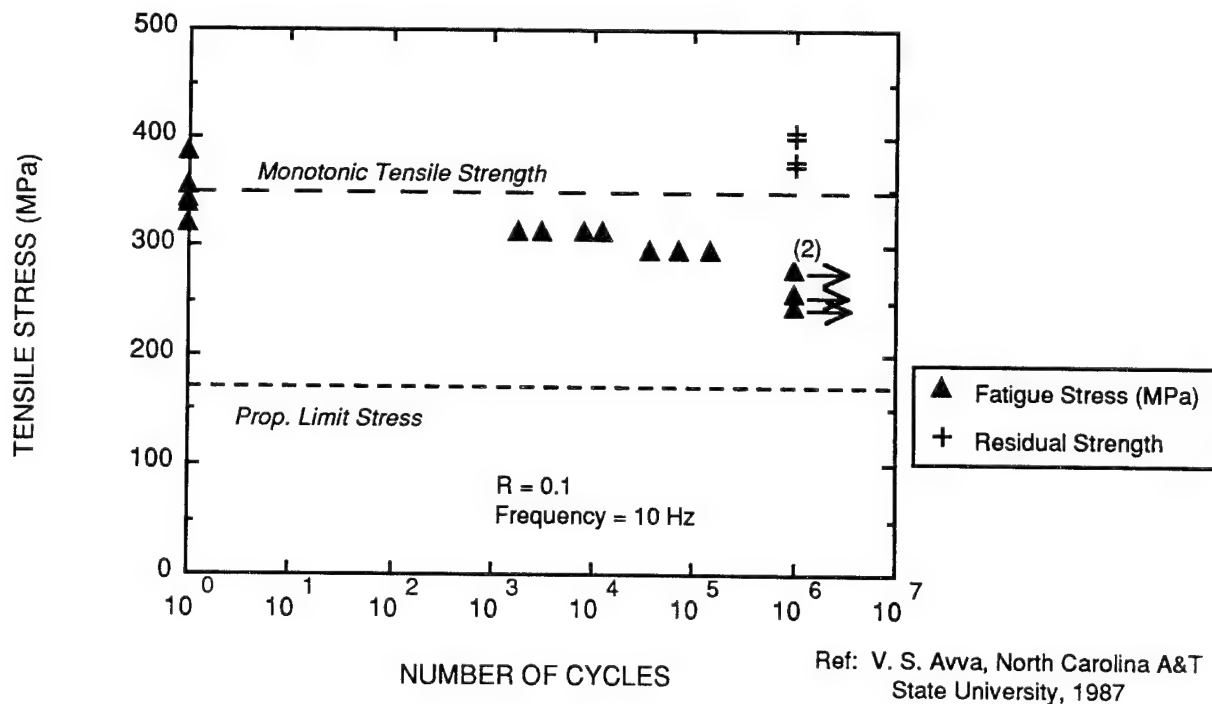


Figure II-10. Tensile Fatigue Behavior of [0/90] HMU/BSG Composites

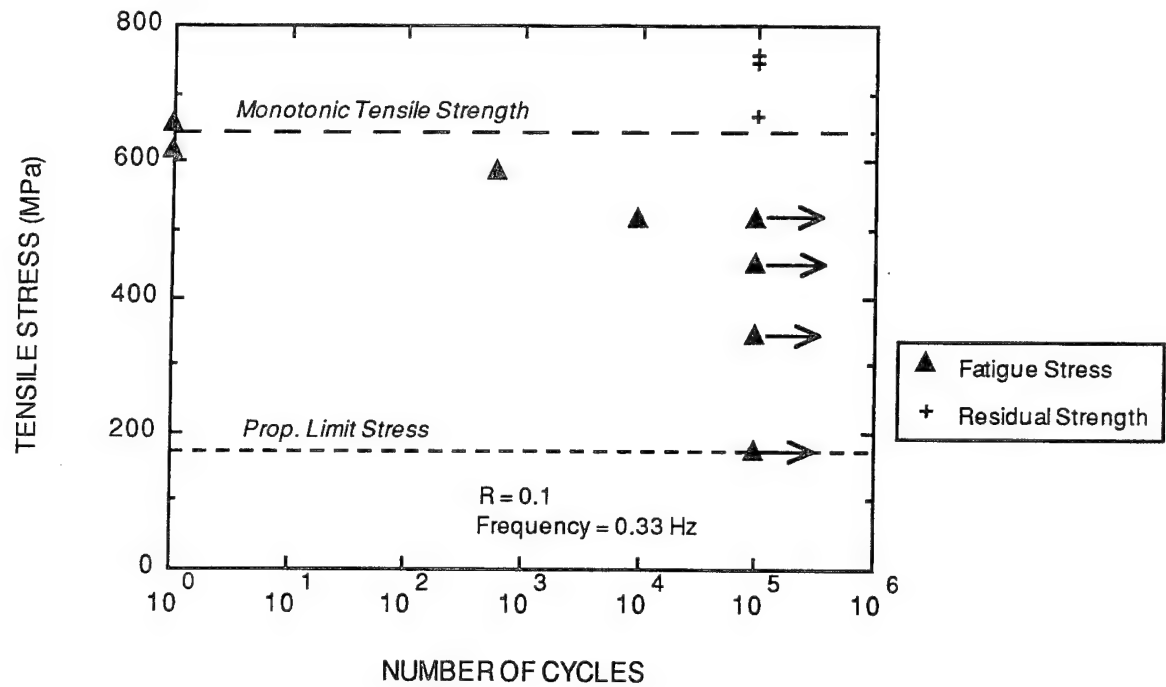


Figure II-11. Tensile Fatigue Behavior of Unidirectional FT700/BSG Composites

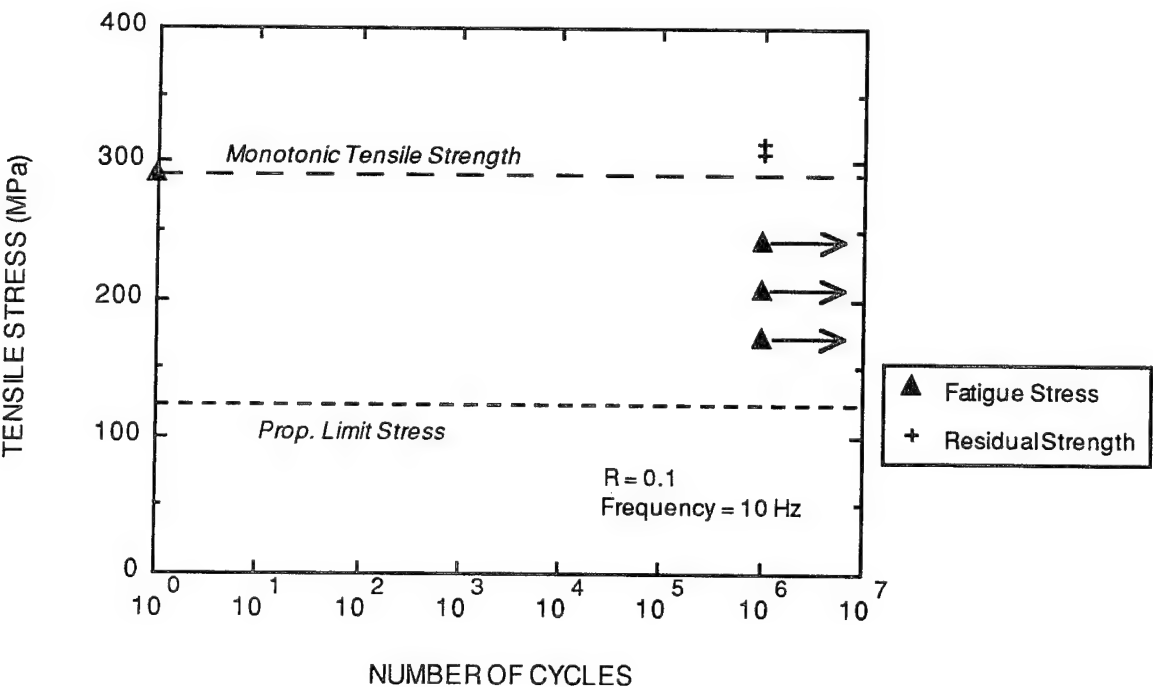


Figure II-12. Tensile Fatigue Behavior of [0/90] P-100/BSG Composites

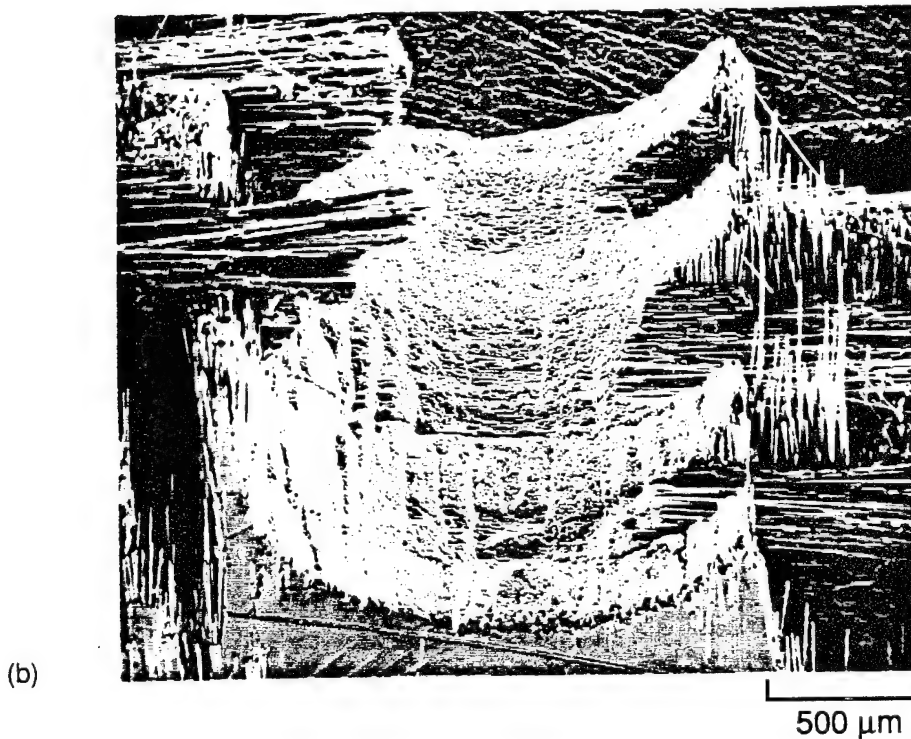
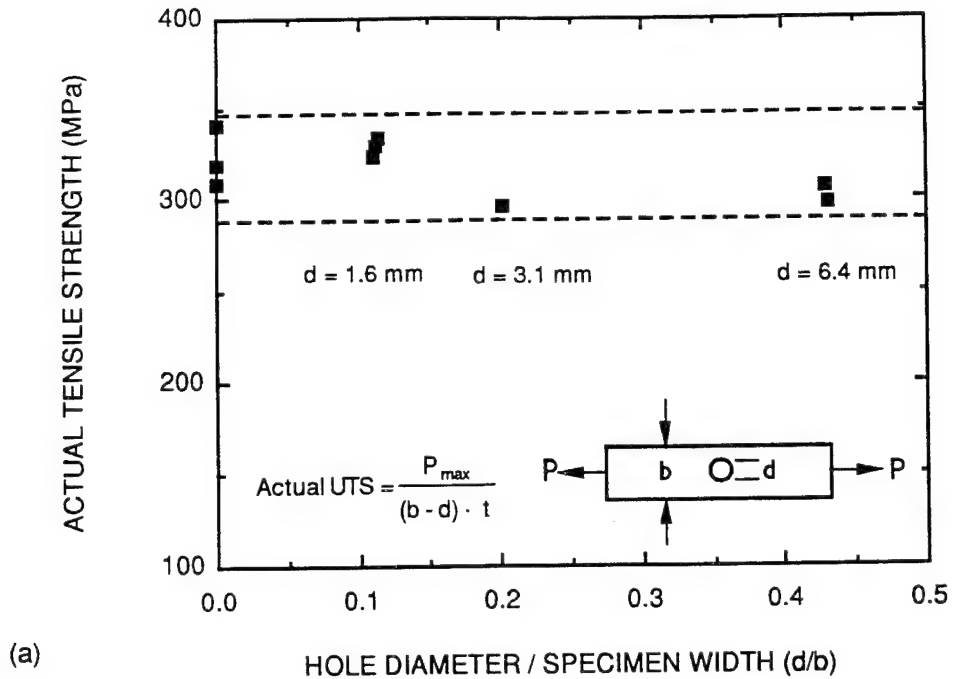
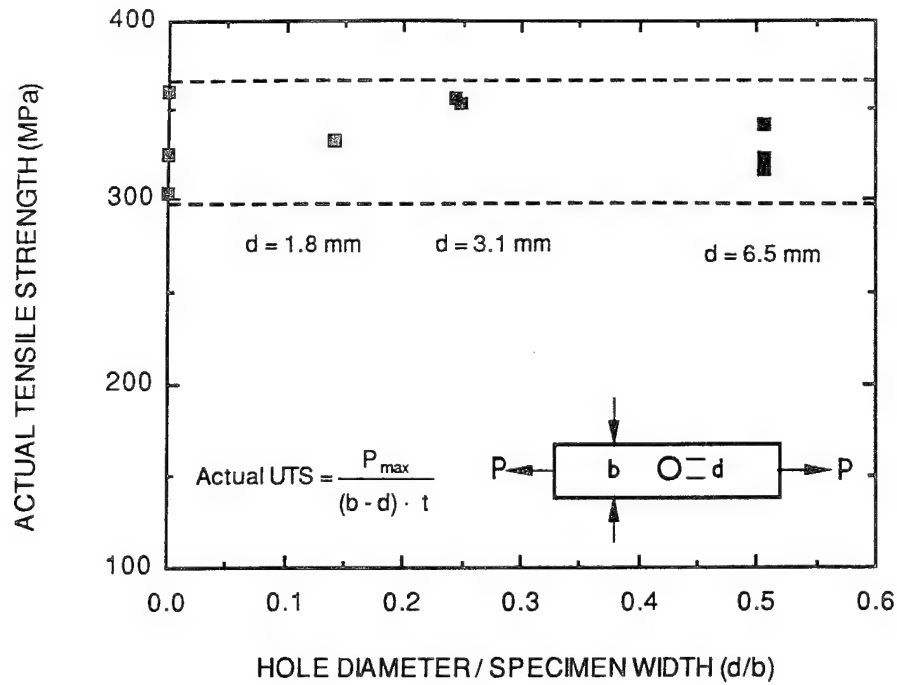
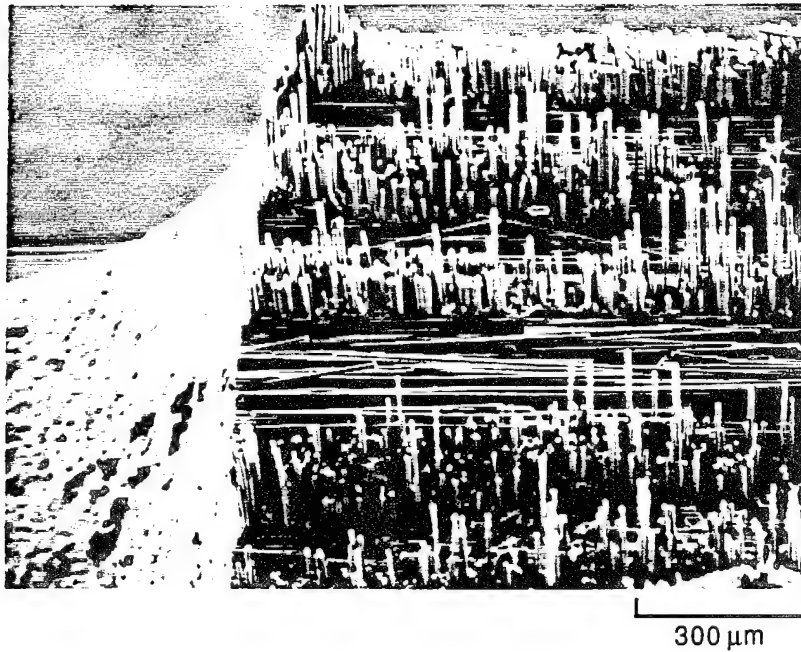


Figure II-13. (a) Tensile Strength of [0/90] HMU/BSG Composites Containing Circular Holes of Various Diameters. (b) Fracture Surface in the Vicinity of the Notch for a [0/90] HMU/BSG Composite.

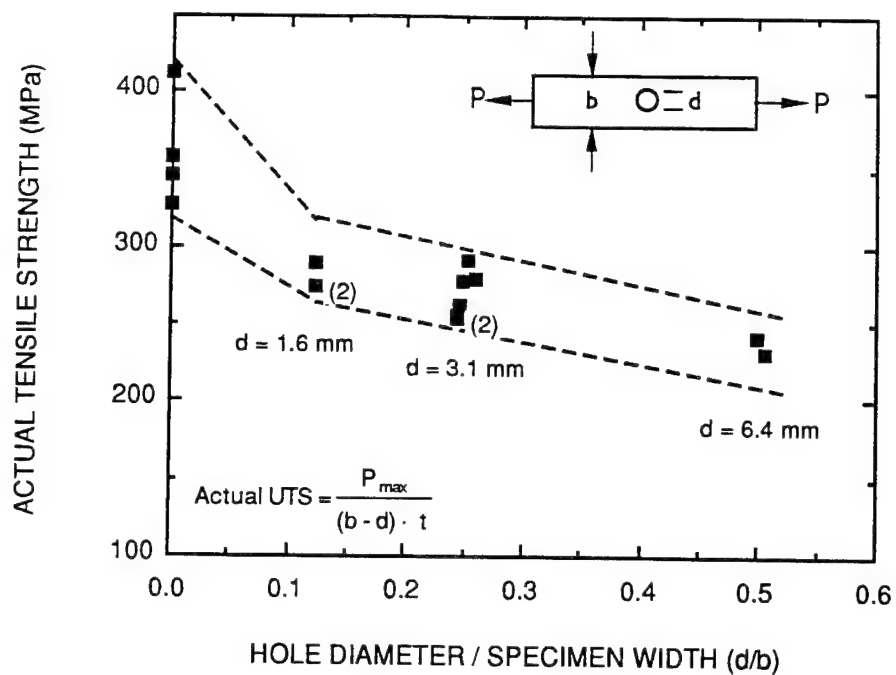


(a)

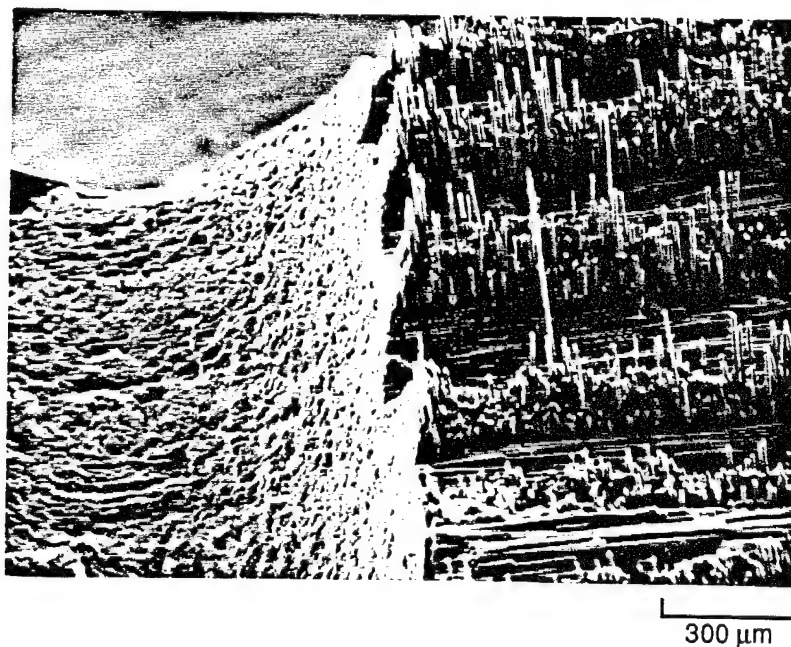


(b)

Figure II-14. (a) Tensile Strength of [0/90] FT700/BSG Composites Containing Circular Holes of Various Diameters. (b) Fracture Surface in the Vicinity of the Notch for a [0/90] FT700/BSG Composite.



(a)



(b)

Figure II-15. (a) Tensile Strength of [0/90] P-100/BSG Composites Containing Circular Holes of Various Diameters. (b) Fracture Surface in the Vicinity of the Notch for a [0/90] P-100/BSG Composite.

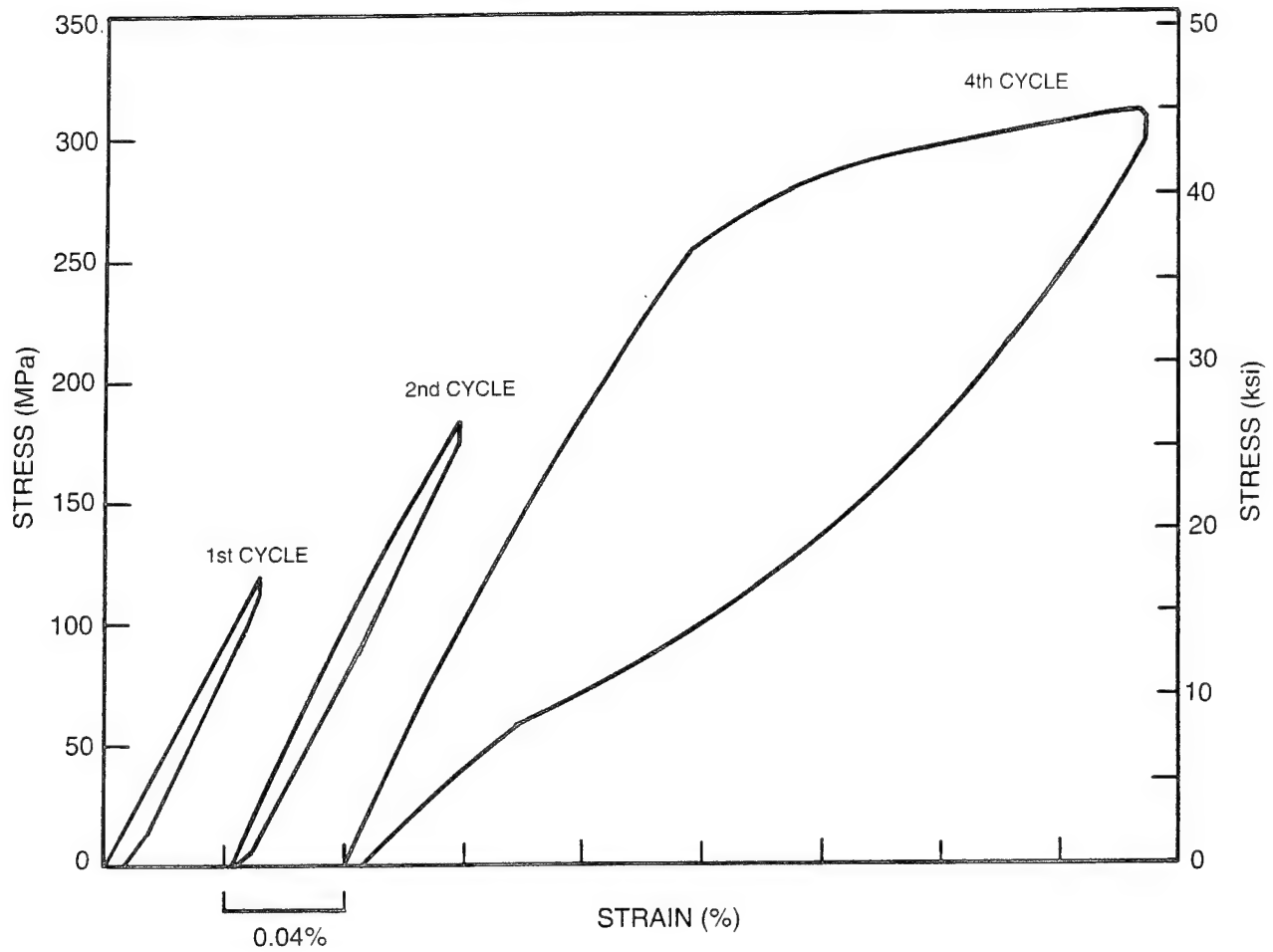


Figure II-16. Cyclic Compressive Stress-Strain Behavior for 0° P-100/BSG-2 Composites

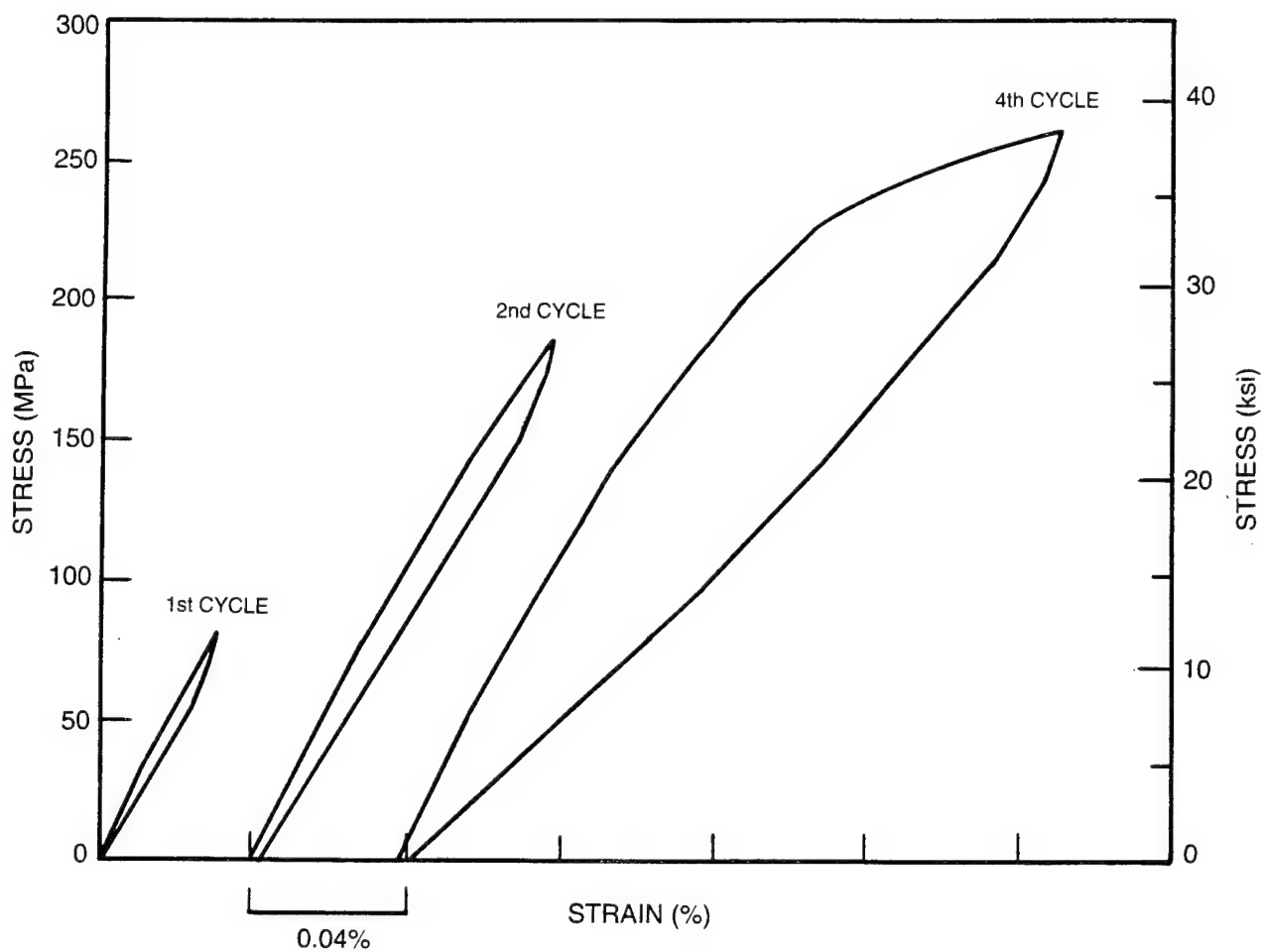


Figure II-17. Cyclic Compressive Stress-Strain Behavior for (0/20/0)_s P-100/BSG-2 Composites

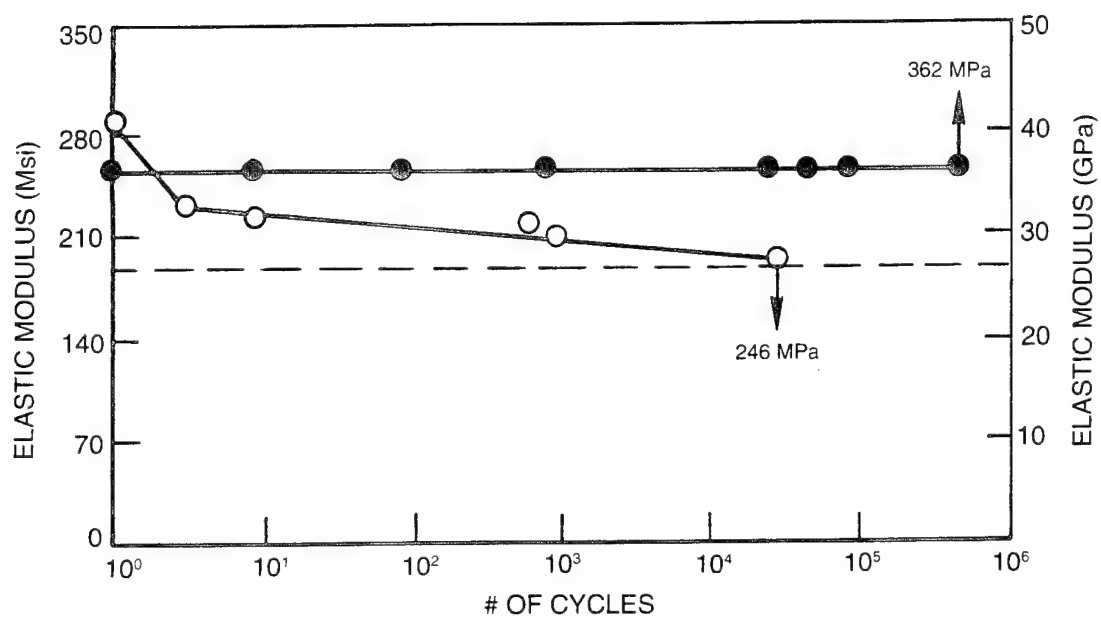
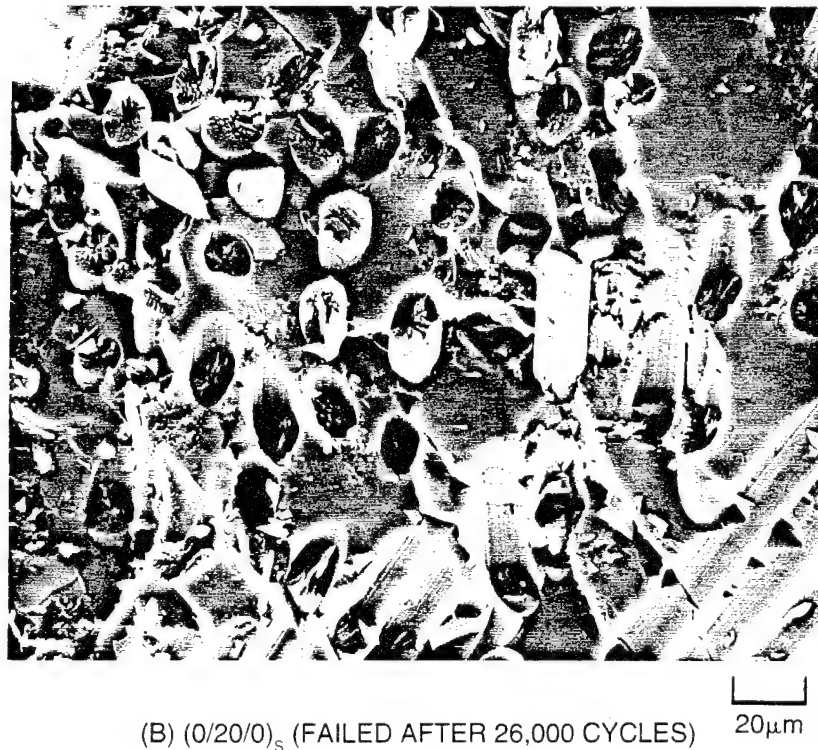


Figure II-18. Elastic Modulus Changes Measured During Compressive Fatigue Testing of Unidirectional (●) and (0/20/0)_s (○) Composites. The Dashed Line Represents 191 GPa.



(A) UNIDIRECTIONAL (208,000 CYCLES, UPLOADED)



(B) (0/20/0)_s (FAILED AFTER 26,000 CYCLES)

Figure II-19. Fracture Surfaces of P-100/BSG-2 Composites after Compressive Fatigue Testing

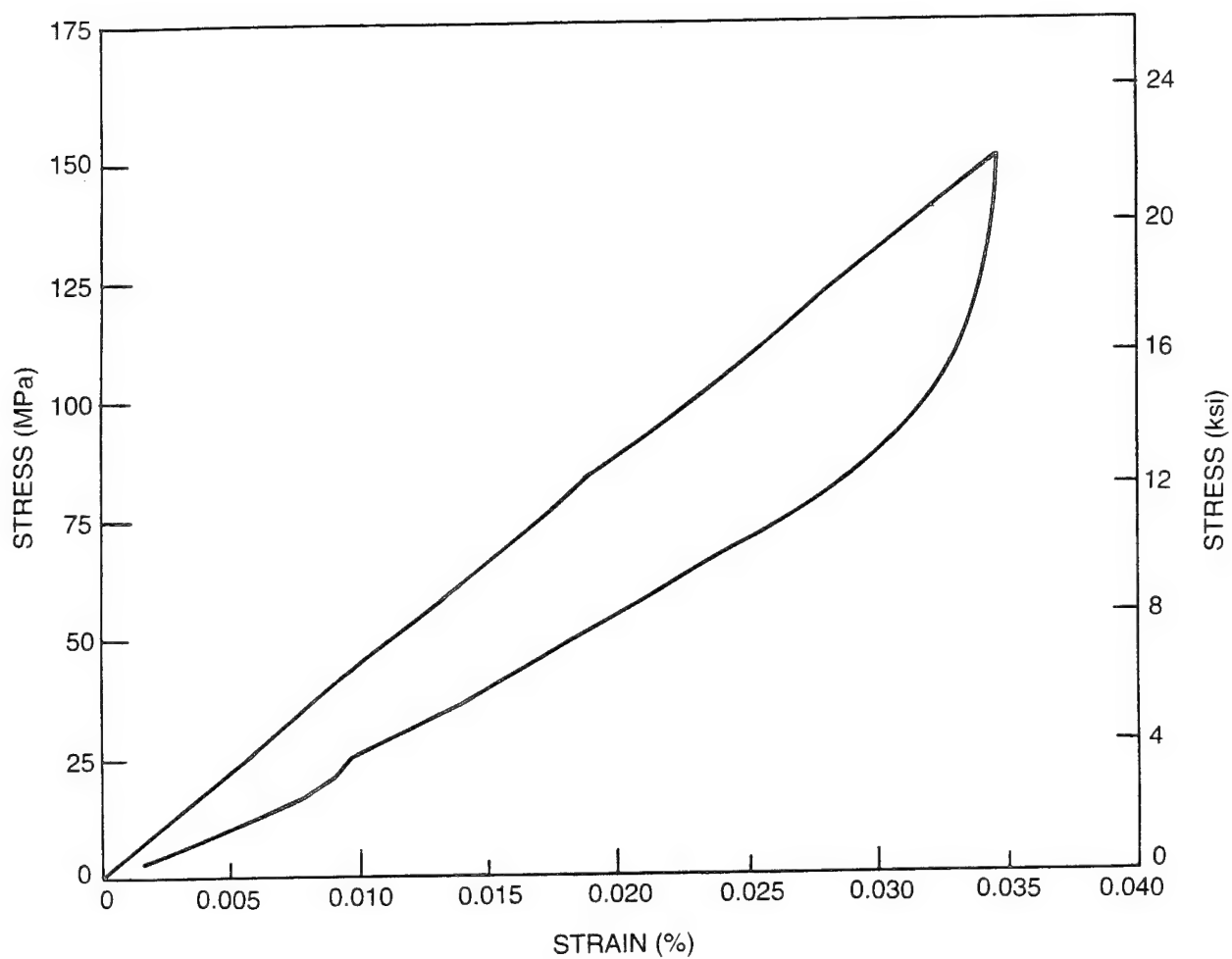


Figure II-20. Representative Hysteresis Behavior Observed for Both 0° HMU/BSG-2 and P-100/BSG-2 Composites During Compressive Pre-Stressing. Samples were Subsequently Loaded to Failure in Tension.

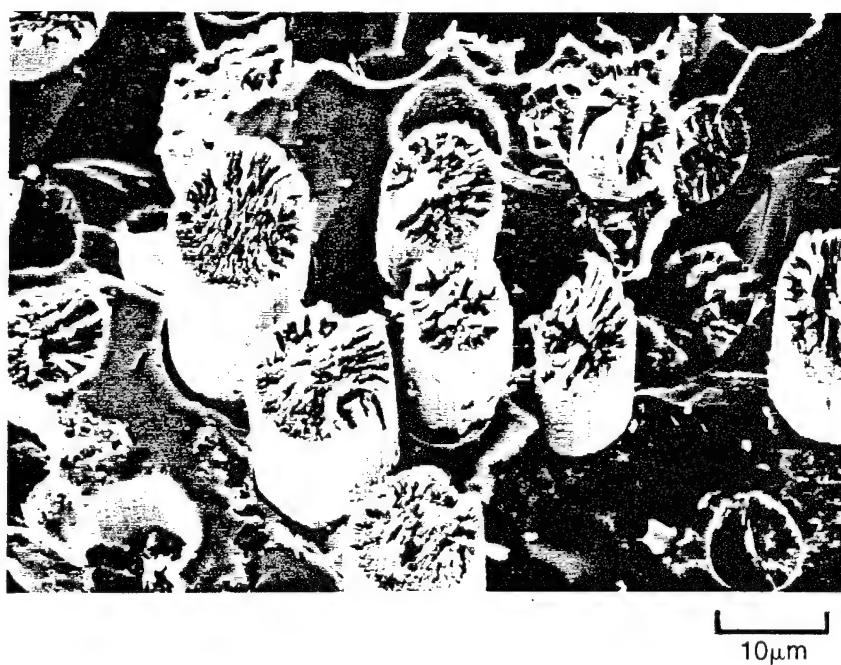


Figure II-21a. Tensile Fracture Surfaces of an as Fabricated (not Pre-Stressed)
P-100/BSG-2 0° Composite

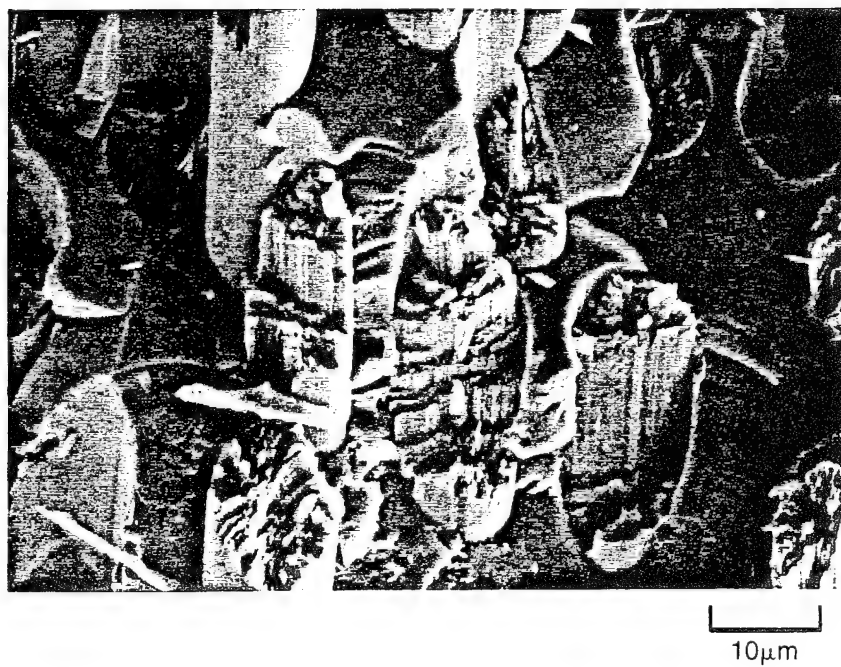
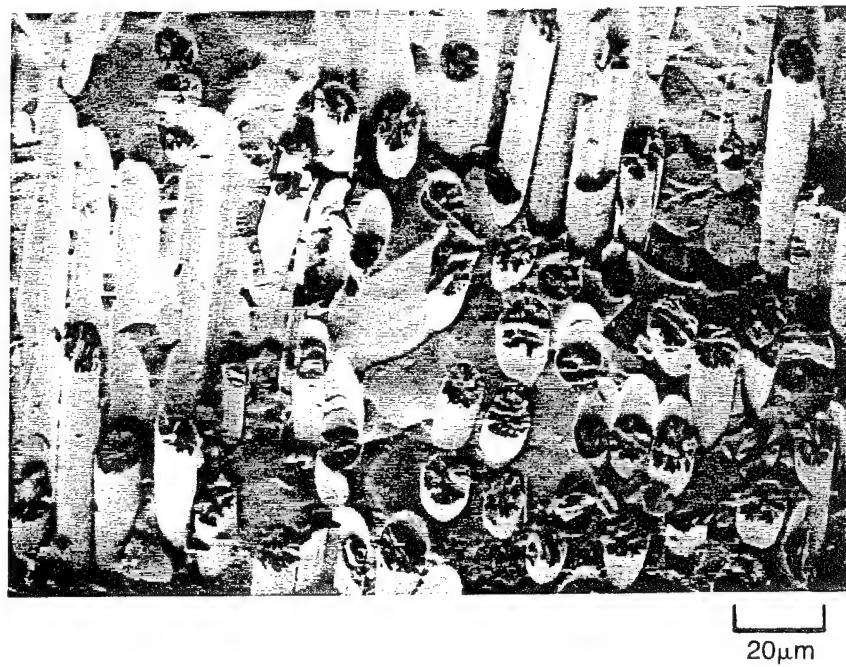


Figure II-21b. Tensile Fracture Surfaces of a Pre-Compression Stressed P-100/BSG-2 0° Composite

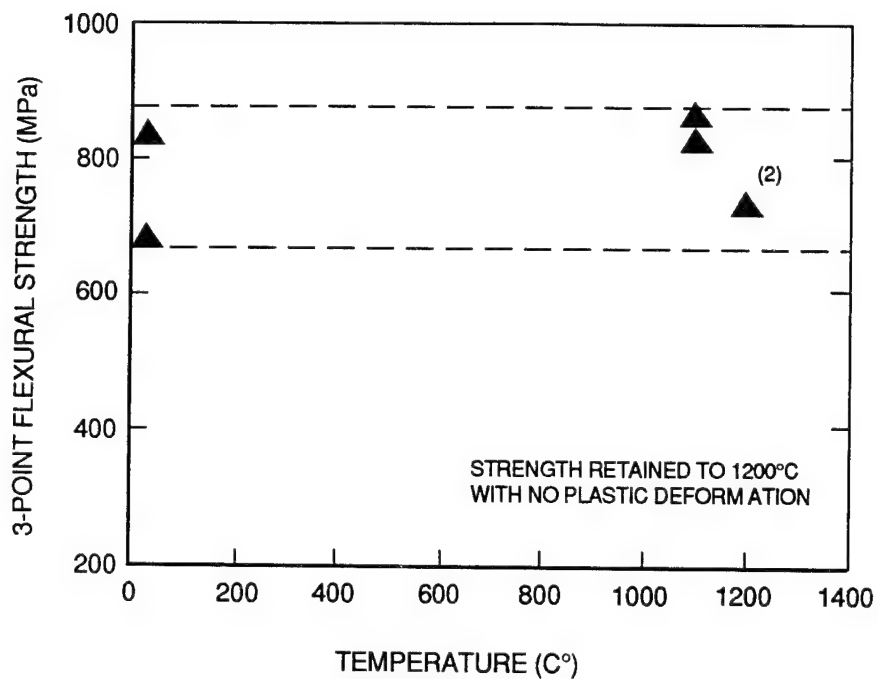


Figure II-22. 3-Point Flexural Strength as a Function of Temperature in Argon for a Unidirectional FT700/BMAS Composite

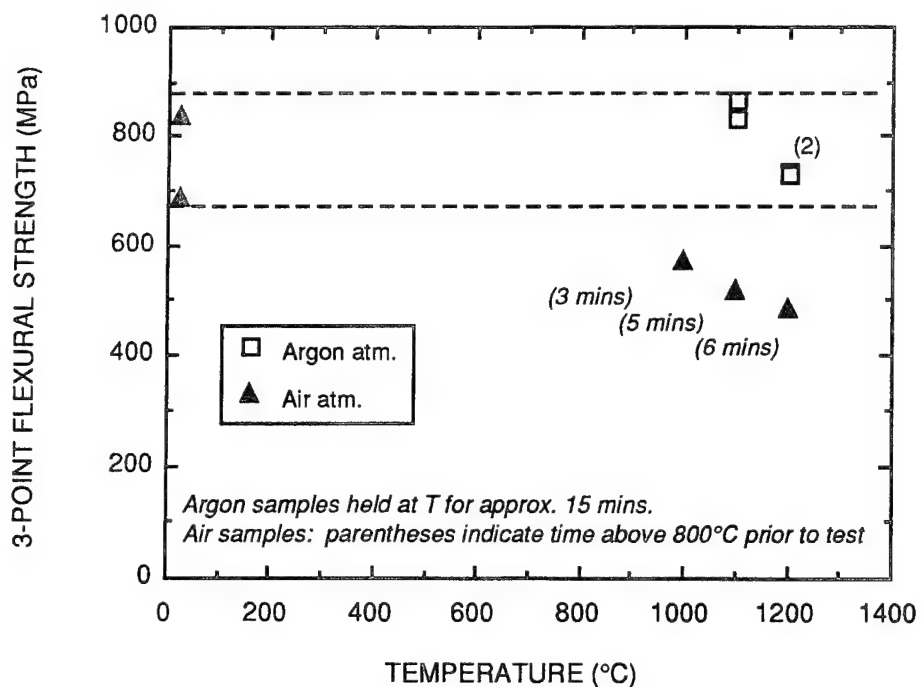


Figure II-23. 3-Point Flexural Strength vs. Temperature in Argon and in Air for a Unidirectional FT700/BMAS Composite

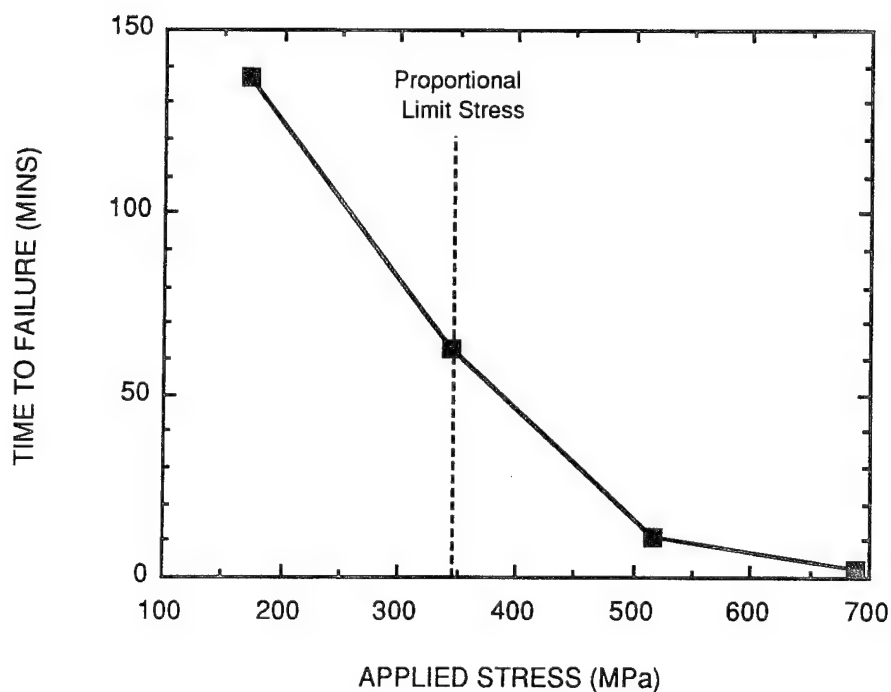


Figure II-24. Time to Failure vs. Applied Flexural Stress in Air at 800°C for a Unidirectional FT700/BMAS Composite

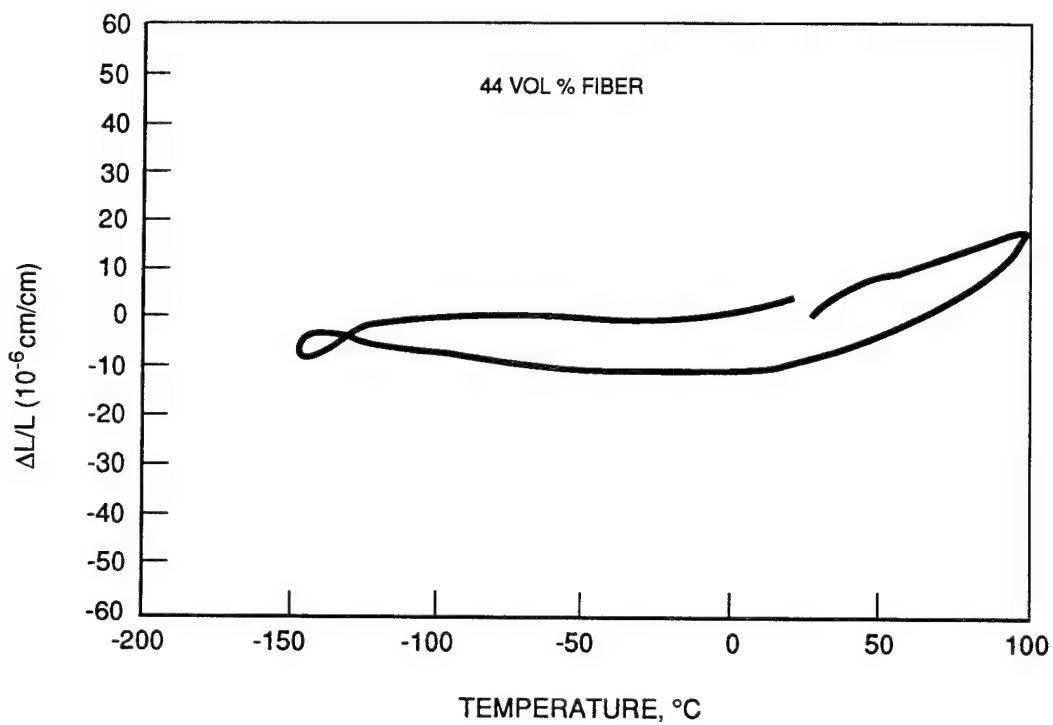


Figure II-25. Thermal Strain ($\Delta L/L$) vs. Temperature for a Quasi-Isotropic [0/±60] Reinforced HMU/BSG Composite Exhibiting Near-zero Thermal Expansion

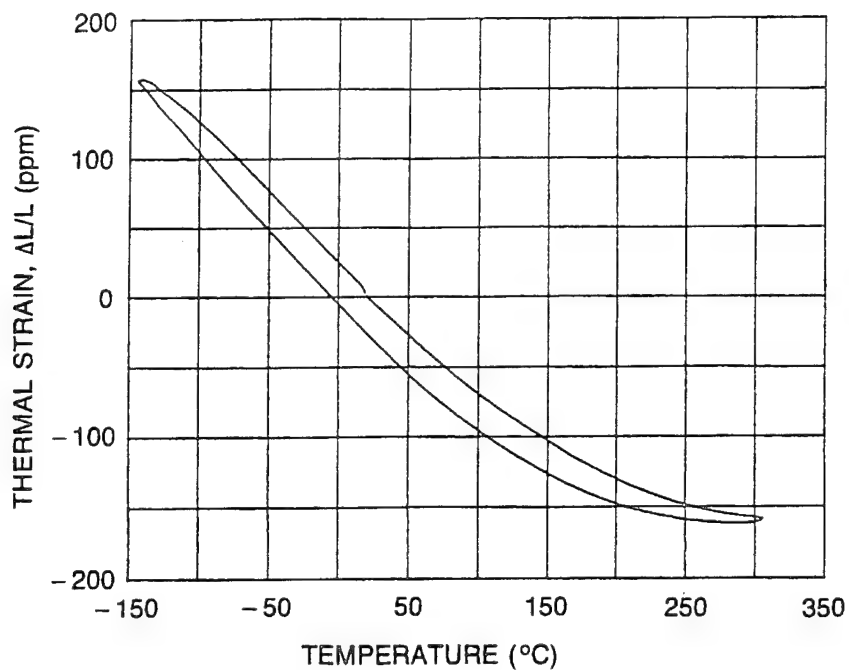


Figure II-26. Axial Thermal Strain vs. Temperature for 0°-45 v/o P-100/BSG Composite

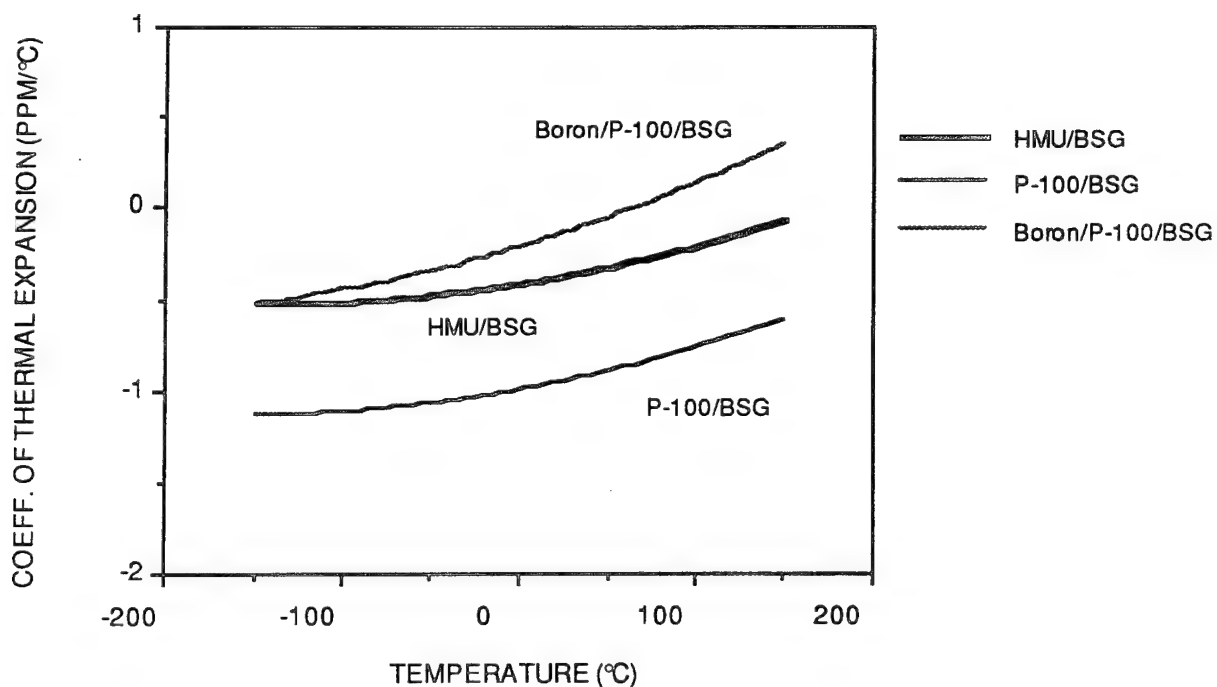


Figure II-27. Coefficient of Thermal Expansion vs. Temperature for Unidirectional HMU/BSG, P-100/BSG, and Boron/P-100/BSG Composites

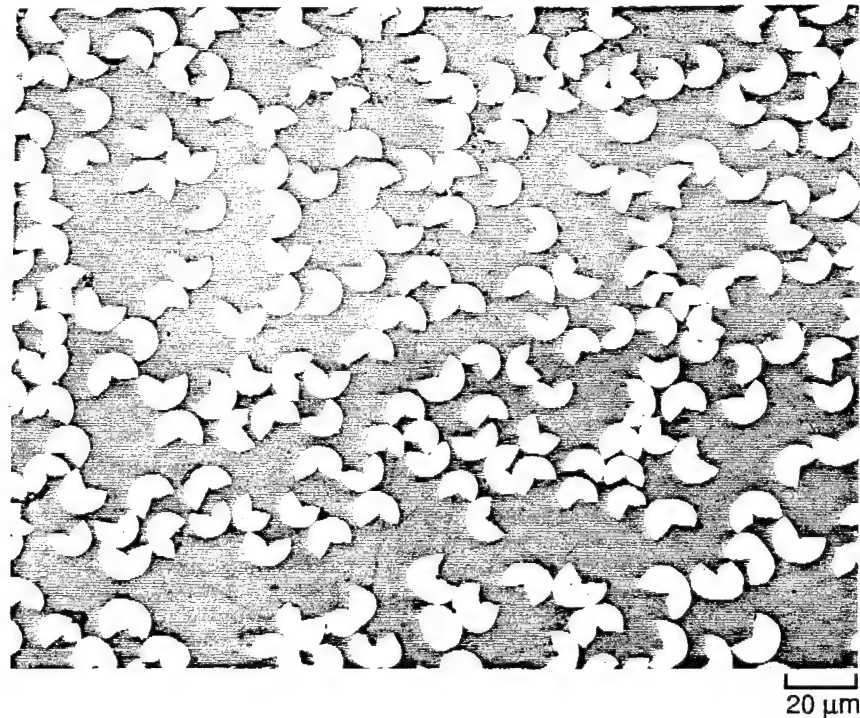


Figure II-28. Microstructure of Unidirectional K1100X/BSG Composite Showing the "Pac-Man" Fiber Structure

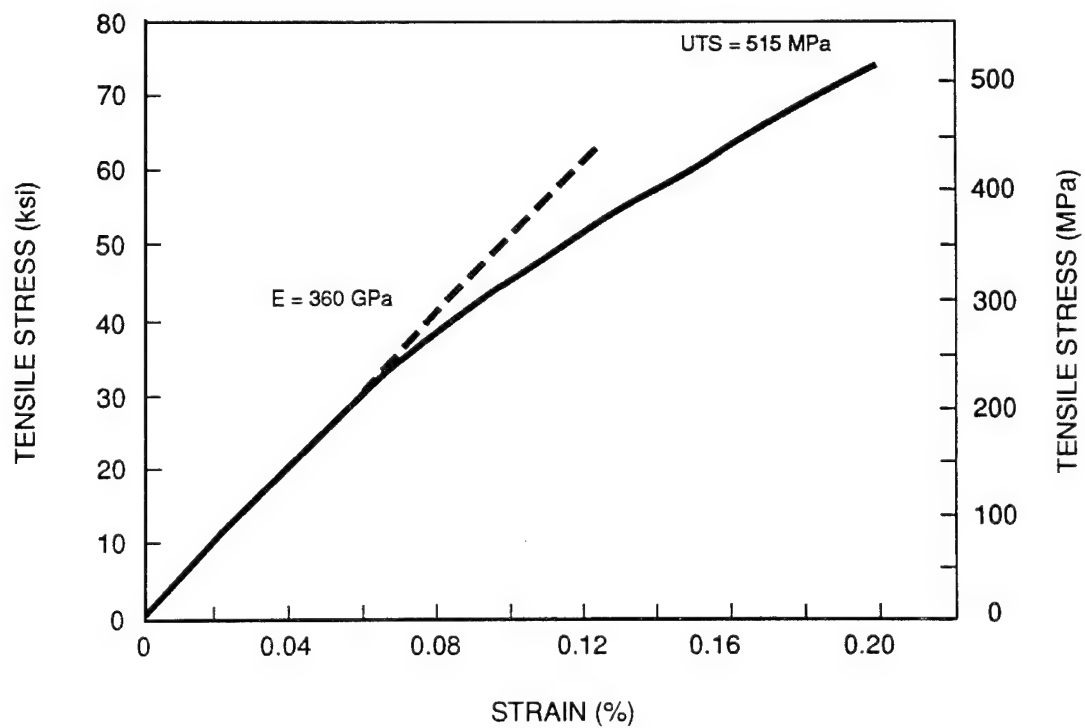


Figure II-29. Tensile Stress-Strain Behavior of a Unidirectional K1100X/BSG Composite Containing 41 v/o Fiber

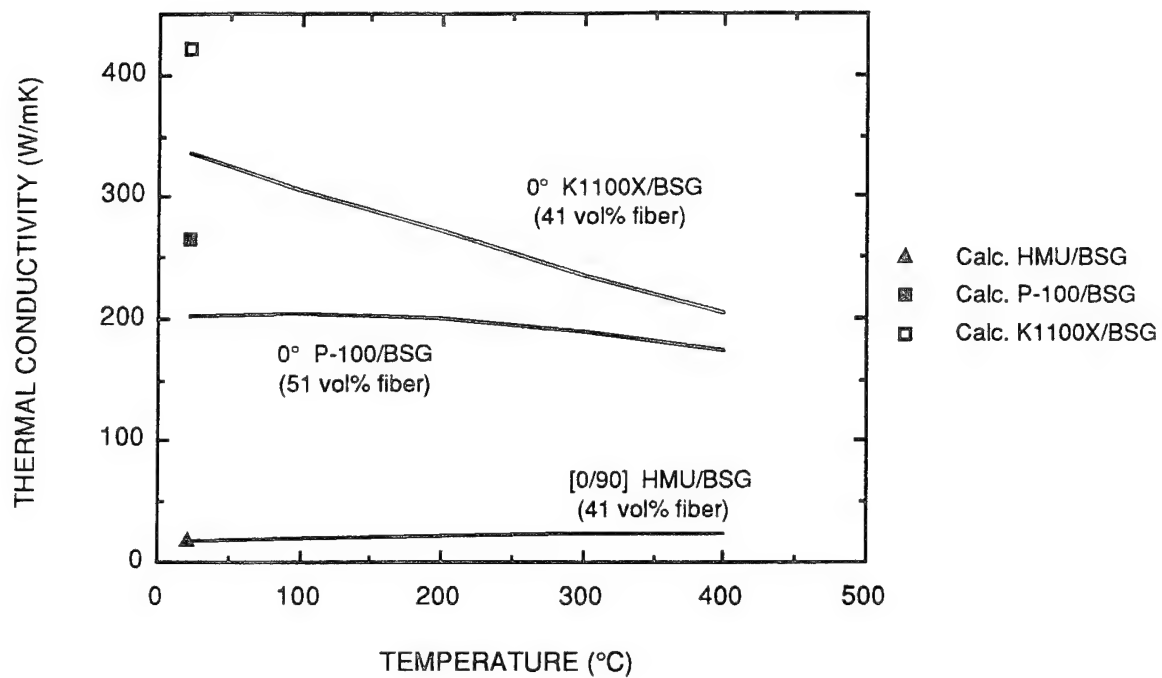


Figure II-30. In-Plane Thermal Conductivity vs. Temperature for 0° K1100X/BSG, 0° P-100/BSG, and [0/90] HMU/BSG Composites

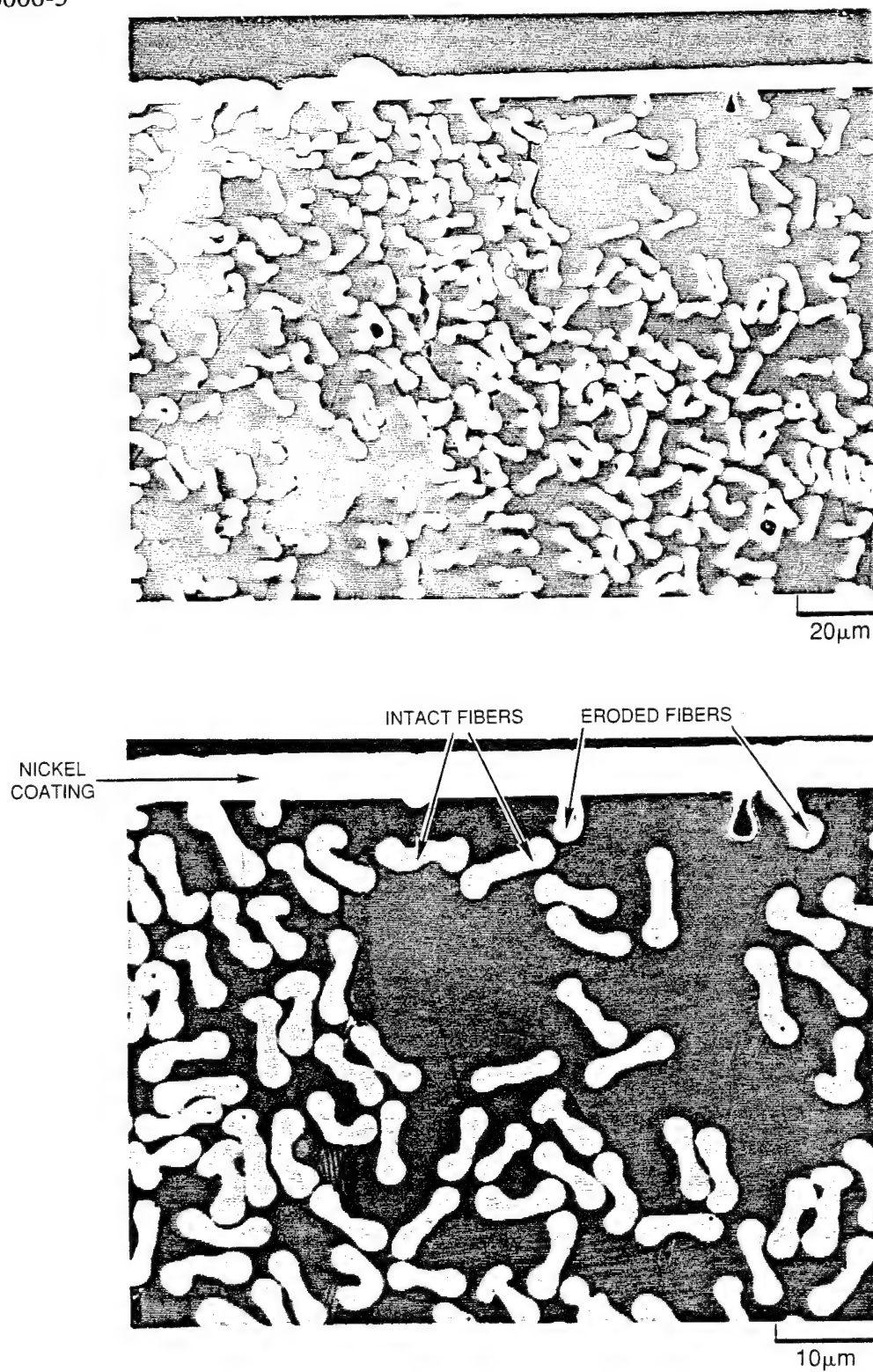


Figure II-31. Cross-Sectional View of Sample GL2-1 Showing Intact Fibers just Below the Sample Surface. Carbon Fibers that are Covered Even by Only a very Thin Layer of Glass have been Protected from AO Erosion.

III. FABRICATION AND PROPERTIES OF THIN-GAGE GLASS MATRIX COMPOSITES FOR SPACE STRUCTURES

III.1. INTRODUCTION

MSNW, Inc. was awarded a Phase I SBIR program by the Strategic Defense Initiative Organization in May, 1992 to evaluate the use of carbon fiber reinforced glass matrix (C/Glass) composites in satellite thermal management applications. The program was administered by the Naval Surface Warfare Center with Mr. Al Bertram serving as the technical monitor and had a period of performance of 6 months. United Technologies Research Center (UTRC) subcontracted to MSNW, Inc. on the program to fabricate and test five thin-gage C/Glass composites with fiber orientations determined by MSNW to be representative of various satellite thermal management applications. The composites were evaluated for microstructural uniformity, tensile stress-strain behavior, thermal expansion behavior, and thermal conductivity characteristics. This report summarizes the results of this composite fabrication and testing program conducted by UTRC.

III.2 COMPOSITE FABRICATION

The C/Glass composites that were fabricated on the program consisted of a borosilicate glass (BSG) matrix reinforced with either P-100 or K1100X carbon fiber, both of which are manufactured by Amoco Performance Products. The P-100 fiber is a commercially available product, with average property values of 2240 MPa tensile strength, 724 GPa elastic modulus, and 520 W/m·K axial thermal conductivity. The K1100X fiber is a developmental fiber tailored specifically for high thermal conductivity, and has average properties of 2350 MPa tensile strength, 920 GPa elastic modulus, and 1030 W/m·K axial thermal conductivity. The composites were fabricated by pre-pregging the carbon fiber with the BSG matrix powder in a slurry impregnation process, followed by lamination of the pre-pregged plies in the desired

configuration and hot-pressing at a temperature above 1200°C to achieve final composite densification.

A list of the composites that were fabricated along with fiber volume fractions and composite thickness is shown in Table III-1. Based on the composite thicknesses, the average ply thickness was approximately 90 to 100 μm in all of the composites. Fiber volume fractions for all of the composites were in the range of 40%. A thin layer of discontinuous carbon paper ("scrim") between the continuous fiber plies was required in the unidirectionally reinforced composites to provide a minimal level of transverse strength and handleability. The general appearance of all of the composites was excellent, with a high degree of surface finish owing to the BSG matrix. The ability to fabricate these materials in such thin-gage form is not a trivial attribute and is one of the characteristics that make C/Glass composites attractive for lightweight satellite thermal management applications.

Table III-1 Thin-Gage C/Glass Composites Fabricated

<u>Fiber/Matrix</u>	<u>Orientation</u>	<u>Vol % Fiber</u>	<u>Thickness (mm)</u>
P-100/BSG	0° + Scrim	40 (P-100) 4.2 (Scrim)	0.36
K1100X/BSG	0° + Scrim	38.1 (K1100X) 4.2 (Scrim)	0.36
P-100/BSG	[0/90] _s	41.9	0.38
K1100X/BSG	[0/90] _s	43.8	0.36
P-100/BSG	[0/±60] _s	41.5	0.58

III.3. MICROSTRUCTURAL EXAMINATION

Representative microstructures of the five composites are shown in the optical micrographs in Figures III-1 through III-5. Fiber distribution appears to be uniform in each of the composites. The scrim cloth between the continuous fiber plies is clearly evident in Figures III-1 and III-2. Intralaminar cracks near the outer surface of some of the composites are thought to be an artifact of the polishing process. Some through-thickness matrix cracks are clearly evident in Figures III-3 through III-5 and are the result of thermal stresses arising from thermal expansion mismatch between the fibers and matrix during cooling from the fabrication temperature.

Figures III-2 and III-4 clearly show the split "Pac-Man" structure of the K1100X fibers. This structure is inherent to the fiber itself and is not a result of composite fabrication. This was verified by observing the identical structure in K1100X fiber directly off the spool. The splitting of the fiber arises due to the highly aligned structure of the fiber and the relatively large graphite crystallite size. Because of this structure, thermal stresses generated during cooling from the graphitization temperature are easily able to "pop open" the fiber.

III.4. TENSILE BEHAVIOR

Tensile properties were measured on each of the five C/Glass composites in both the 0° and 90° directions. A minimum of three samples were tested in each configuration. Straight-sided specimens were used, with an average width of 8.9 mm and a gage length of 2.5 cm. Tapered fiberglass tabs were adhesively bonded to the ends of both sides of the samples to provide a gripping surface for the wedge-loaded tensile grips. Poisson strain gages were glued on to both sides of the specimens in the center of the gage section. Because of the thin nature of the specimens, it was critical to ensure that the end tabs were flat and parallel along their entire length. Specimens were measured at three points along the length of the tab and ground flat if they were out of parallel by more than 0.025 mm. This prevented inducing any bending or twisting of the samples during testing and provided true values of composite tensile strength. Samples were loaded at a constant cross-head speed of 0.13 cm/min.

Results of tensile testing for all of the composites is summarized in Table II-2. Each value shown is the average of three separate tests. Values of ultimate tensile strength and elastic modulus were consistent with expectations for the most part. One sample of the unidirectionally reinforced P-100/BSG composite exhibited a particularly high value of tensile strength at 599 MPa. The transverse strengths for both of the unidirectionally reinforced composites were considered to be very good, with an average strength of 38 MPa and failure strains on the order of 0.6%. All of the composites exhibited a considerable amount of fiber pullout behavior on the fracture surface, indicating a relatively weak fiber-matrix interfacial bond and a reasonable degree of crack deflection during fracture. The non-linear shapes of the stress-strain curves that were observed are typical for these types of C/Glass composites.

III.5. THERMAL EXPANSION BEHAVIOR

Thermal expansion behavior was measured for each of the five composites in both the 0° and 90° directions. Each sample was cycled over the temperature range from 25°C to 300°C to

Table III-2 - Mechanical Properties of Thin-Gage C/Glass Composites

Fiber/Matrix	Orientation	Fiber Vol %	Test Direction	UTS (MPa)	E (GPa)	Failure Strain (%)	Prop. Limit Stress (MPa)	Poisson's Ratio
P-100/BSG	0° + Scrim	40 (P-100) 4.2 (Scrim)	0°	466	289	0.18	181	0.19
			90°	39	22	0.62	7	0.02
K1100X/BSG	0° + Scrim	38.1 (K1100) 4.2 (Scrim)	0°	337	316	0.13	63	0.17
			90°	38	22	0.57	6	0.02
P-100/BSG	[0/90]s	40.7	0°	328	169	0.20	115	0.02
			90°	287	161	0.19	130	0.02
K1100X/BSG	[0/90]s	41.5	0°	204	168	0.14	67	0.01
			90°	269	186	0.16	59	0.00
P-100/BSG	[0/±60]s	41.4	0°	166	105	0.17	60	0.20
			90°	220	105	0.31	61	0.27

-50°C to 25°C at a heating/cooling rate of 2°C/min for a total of 5 thermal cycles. The original length of each thermal expansion sample was 5.1 cm.

Representative thermal strain curves and secant coefficient of thermal expansion (CTE) curves for the composites are shown in Figures III-6 through III-13. The thermal strain ($\Delta L/L$) figures each show the thermal strain experienced by the sample over the first two cycles plus the thermal strain for cycle 5. The $\Delta L/L$ shown is the *cumulative* thermal strain over all of the thermal cycles, viz. any residual thermal strain remaining at the end of a thermal cycle serves as the starting point for the next thermal cycle. For example, Figure III-6 indicates that approximately -60 ppm thermal strain remains in the sample at the end of cycle 1. The curve for cycle 2 then begins at that point (-60 ppm), rather than starting back at zero. Thermal strain curves are shown for both 0° and 90° orientations for the unidirectionally reinforced P-100 composite with scrim since the observed behavior was very different for the two orientations. Thermal strain behavior for the $[0/90]_s$ composites and the $[0/\pm 60]_s$ composite was basically the same for both 0° and 90° orientations. Therefore, thermal strain curves for only the 0° orientation are shown for these multiaxially reinforced composites.

Secant CTE for the heating portion of each cycle was determined by dividing the thermal strain at each temperature by the temperature difference from the starting temperature (25°C). This method of calculating CTE gives an indication of the total change in length at a given temperature, and differs from a tangential method which provides an indication of the instantaneous change in length at a given temperature. Secant and tangential CTE are only the same for materials exhibiting linear thermal expansion behavior. The figures shown correspond to the heating portion of the final thermal cycle and are shown merely to give an indication of the magnitude of CTE over the indicated temperature range for each material.

There are several features of the thermal strain behavior that merit some comment. For each of the five composites, the initial thermal cycle resulted in some degree of negative residual strain at the end of the cycle. For the most part, subsequent cycling resulted in closed hysteresis loops, with no significant change in overall thermal strain behavior in those cycles following the initial cycle. This suggests that the materials are dimensionally stable following an initial heating/cooling cycle. The negative residual strain at the end of the initial cycle is not fully understood, but is thought to be related to partial closure of matrix cracks that exist initially due to stresses arising from thermal expansion mismatch between the fibers and matrix. Another feature of the thermal strain behavior that deserves some comment is that the 0° behavior did not really differ that much among the three different ply configurations. This was somewhat unexpected, since for other C/Glass composite systems $[0/90]_s$ or $[0/\pm 60]_s$ configurations usually exhibit thermal expansion that is less negative (close to zero) than unidirectionally reinforced composites.

III.6. THERMAL CONDUCTIVITY

Thermal conductivity was measured at room temperature for the unidirectionally reinforced P-100/BSG and K1100X/BSG composites using the cold plate technique. Measurements were performed at Research Opportunities, Inc. in Torrance, CA. Steady-state thermal conductivity was determined in the direction of the fiber using the entire 15.2 cm x 15.2 cm composite panel. In these measurements, one end of each panel was submersed in a cold fluid and held at a constant temperature of 15°C. A strip heater was attached to the opposite end of the panel and set to a temperature of approximately 63°C. The orientation of the panel was such that the fibers were aligned in the direction of the heat flow between the heater and the cold bath. RTD's were affixed to the panel at different locations and were used to measure the panel temperature at each location after a 30 minute stabilization time. The heat flow calculated from these temperatures and locations was then used to determine the thermal conductivity of the panel in the direction of the fiber.

Thermal conductivity for the unidirectionally reinforced P-100/BSG and K1100X/BSG composites as determined using the above technique is shown in Table III-3. The values agree fairly well with those that would be predicted using the rule-of mixtures, indicating that composite processing did not significantly damage the high thermal conductivity characteristics of either the P-100 or K1100X fiber. The high values of thermal conductivity exhibited by these C/Glass composites indicate that they are good candidates for many lightweight satellite thermal management applications.

Table III-3 - Thermal Conductivity of Thin-Gage C/Glass Composites

<u>Fiber/Matrix</u>	<u>Orientation</u>	<u>Fiber Vol %</u>	<u>Thermal Conductivity (W/m K)*</u>
P-100/BSG	0° + Scrim	40 (P-100) 4.2 (Scrim)	228
K1100X/BSG	0° + Scrim	38.1 (K1100X) 4.2 (Scrim)	376

* Thermal conductivity measured in-plane in the fiber direction at room temperature

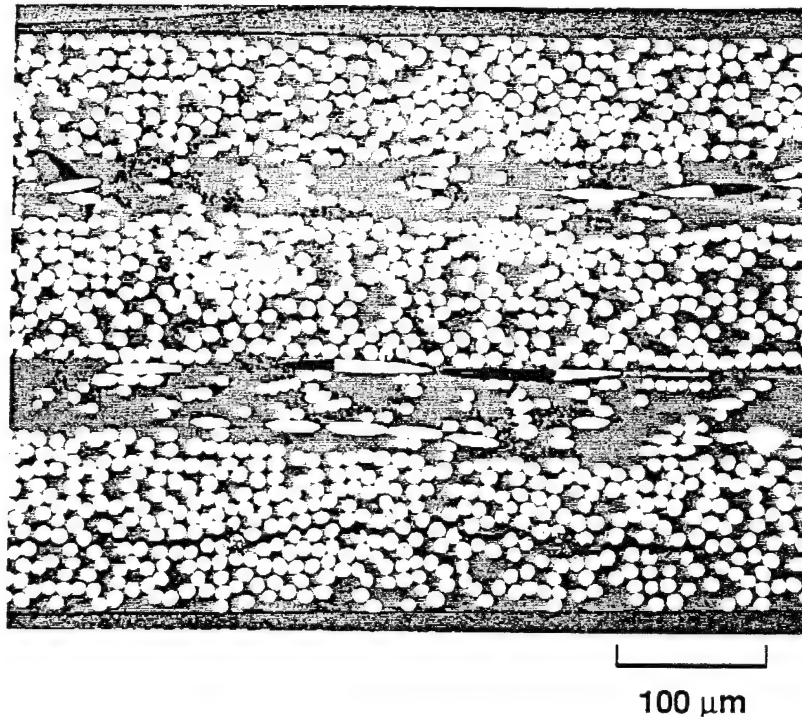


Figure III-1. Transverse microstructure of the unidirectionally reinforced P-100/BSG composite containing scrim cloth.

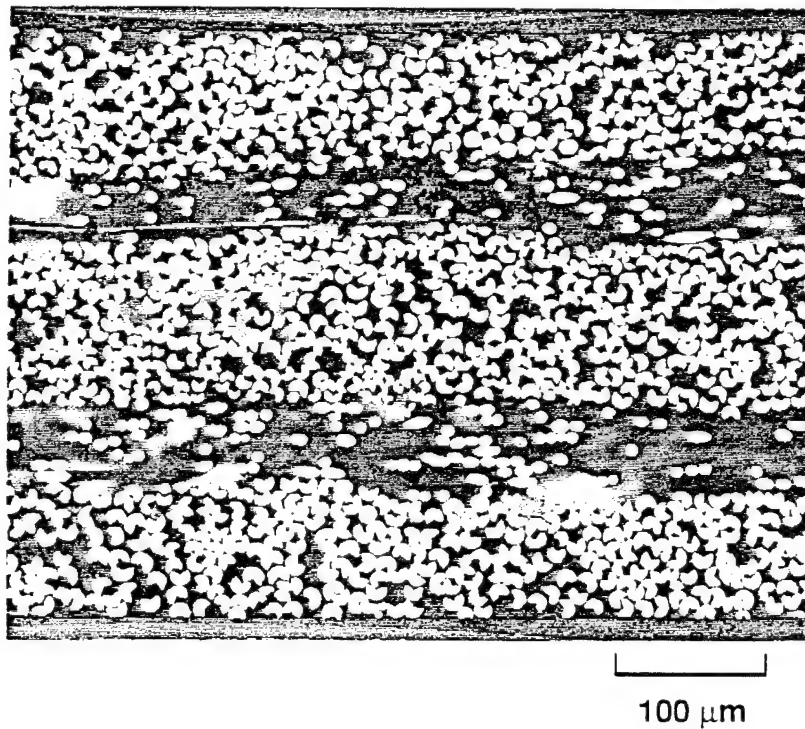


Figure III-2. Transverse microstructure of the unidirectionally reinforced K1100X/BSG composite containing scrim cloth.

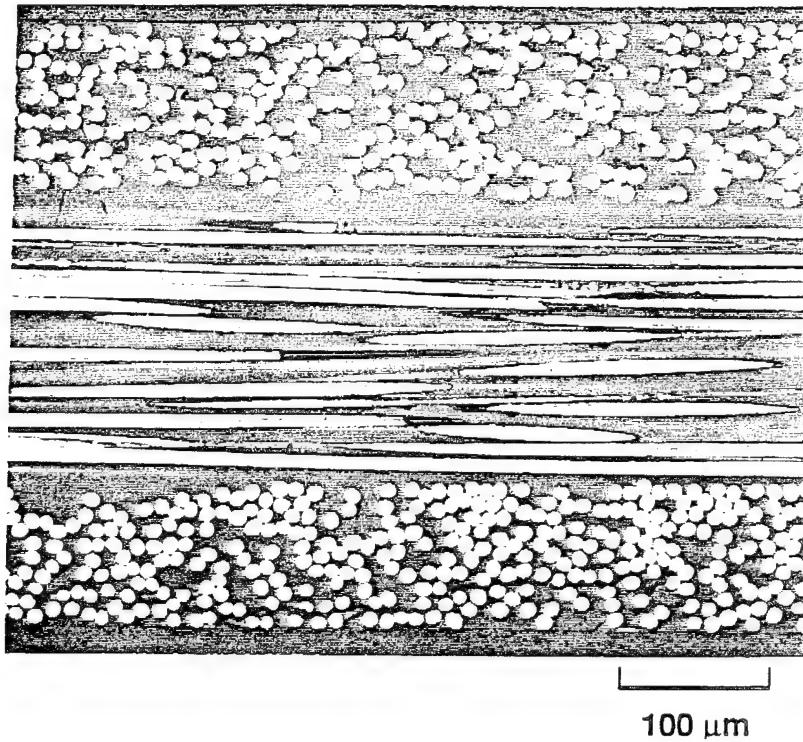


Figure III-3. Transverse microstructure of the $[0/90]_s$ reinforced P-100/BSG composite.

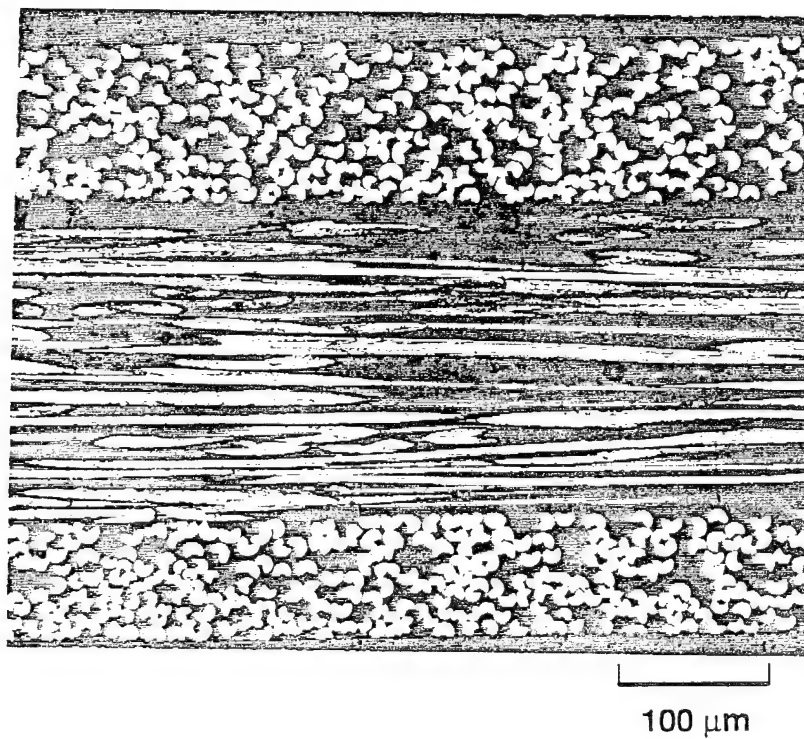


Figure III-4. Transverse microstructure of the $[0/90]_s$ reinforced K1100X/BSG composite.

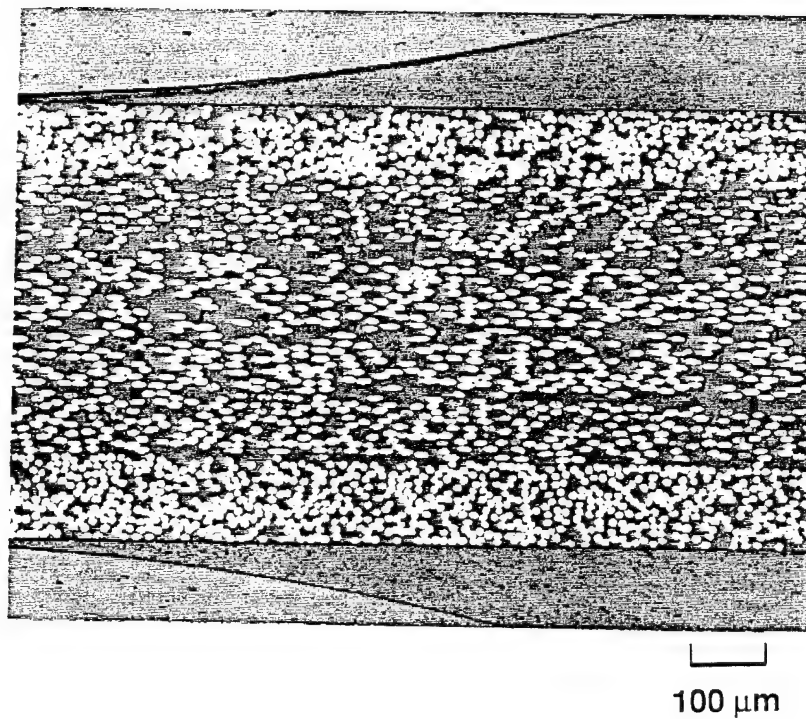


Figure III-5. Transverse microstructure of the $[0/\pm 60]_s$ reinforced P-100/BSG composite.

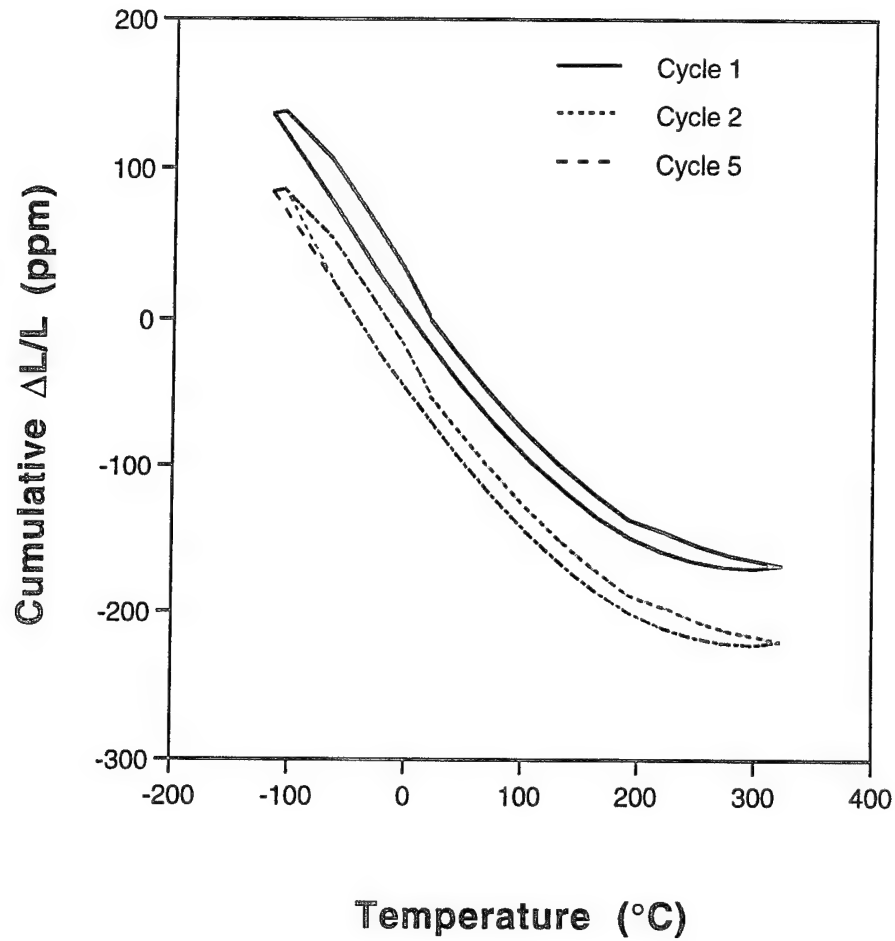


Figure III-6. Thermal strain vs. temperature for the 0° + Scrim P-100/BSG composite measured in the 0° direction. Cycles 1, 2, and 5 are shown in the figure.

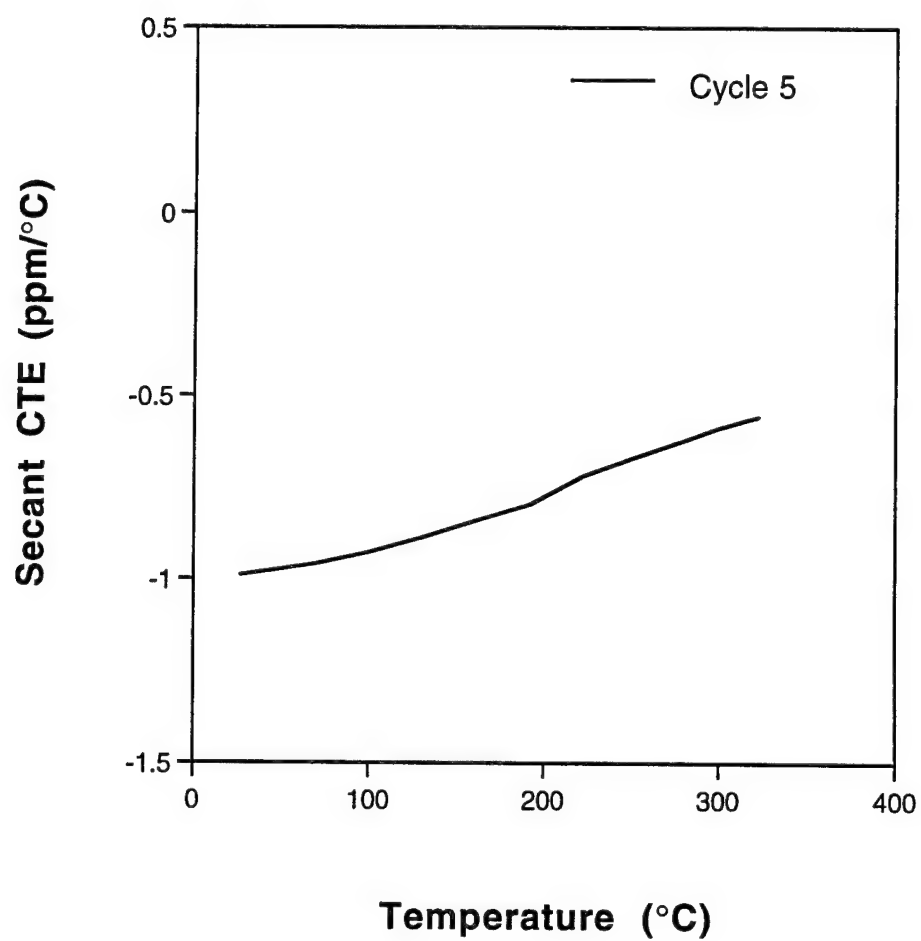


Figure III-7. Secant CTE vs. temperature for the 0° + Scrim P-100/BSG composite measured in the 0° direction. The curve shown corresponds to the initial heating portion of Cycle 5.

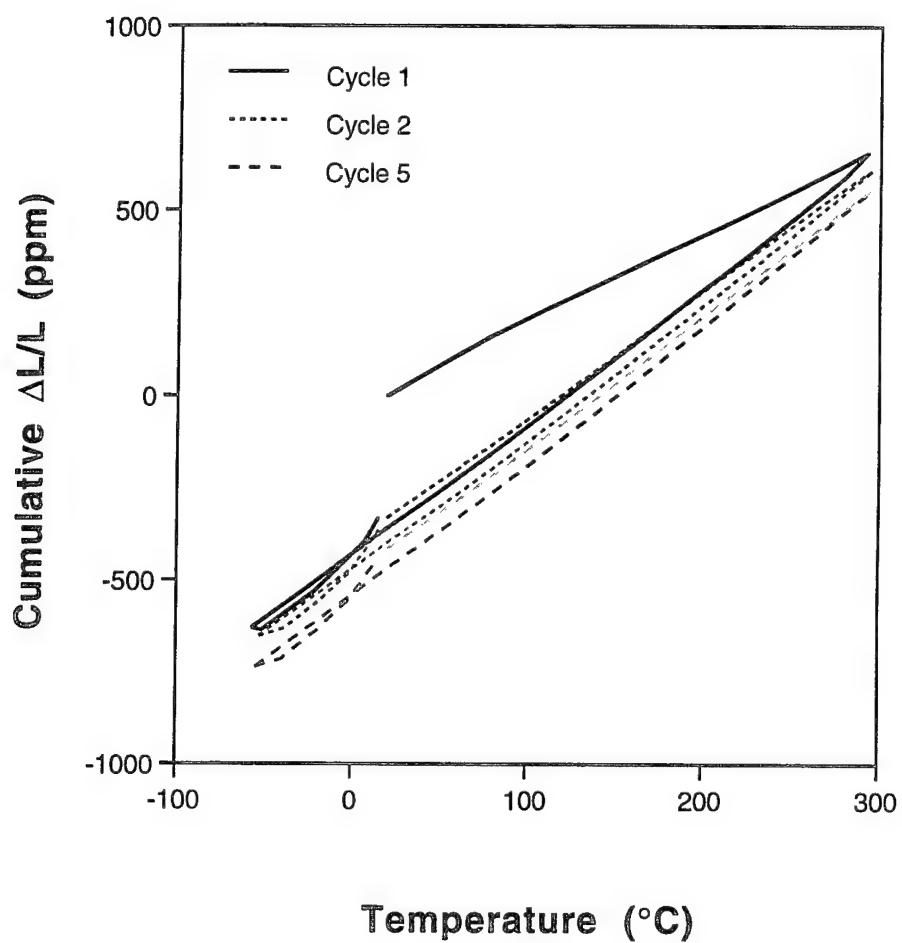


Figure III-8. Thermal strain vs. temperature for the 0° + Scrim P-100/BSG composite measured in the 90° direction. Cycles 1, 2, and 5 are shown in the figure.

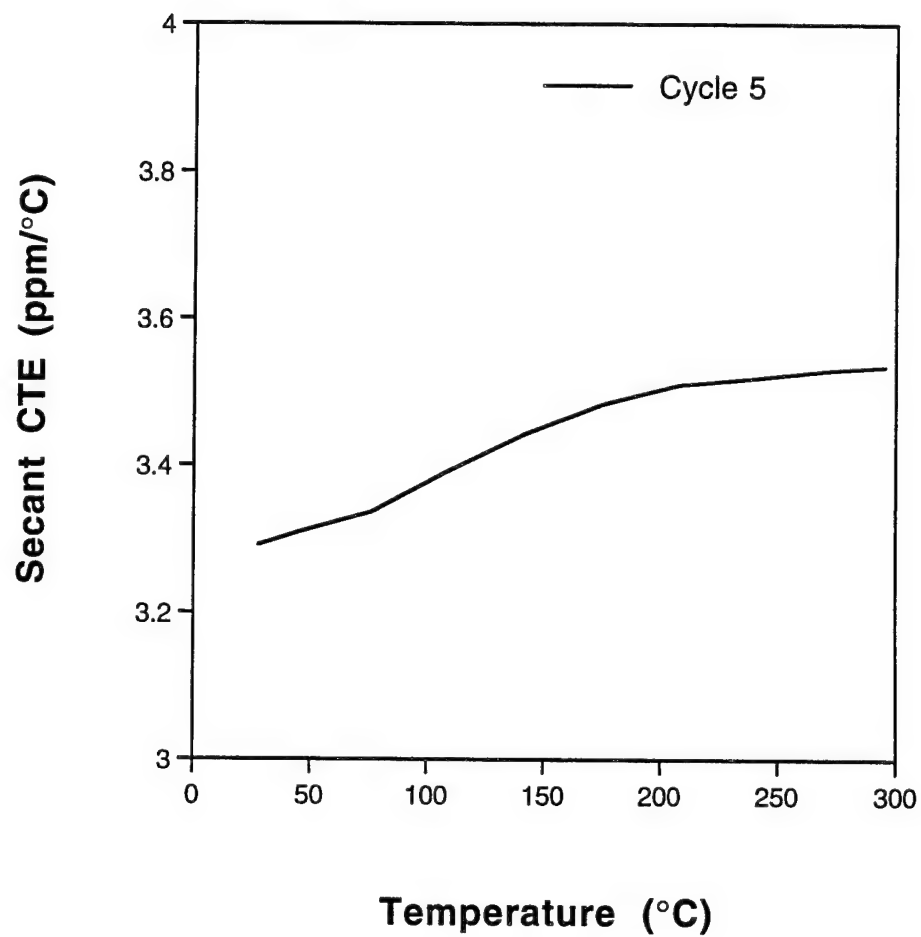


Figure III-9. Secant CTE vs. temperature for the 0° + Scrim P-100/BSG composite measured in the 90° direction. The curve shown corresponds to the initial heating portion of Cycle 5.

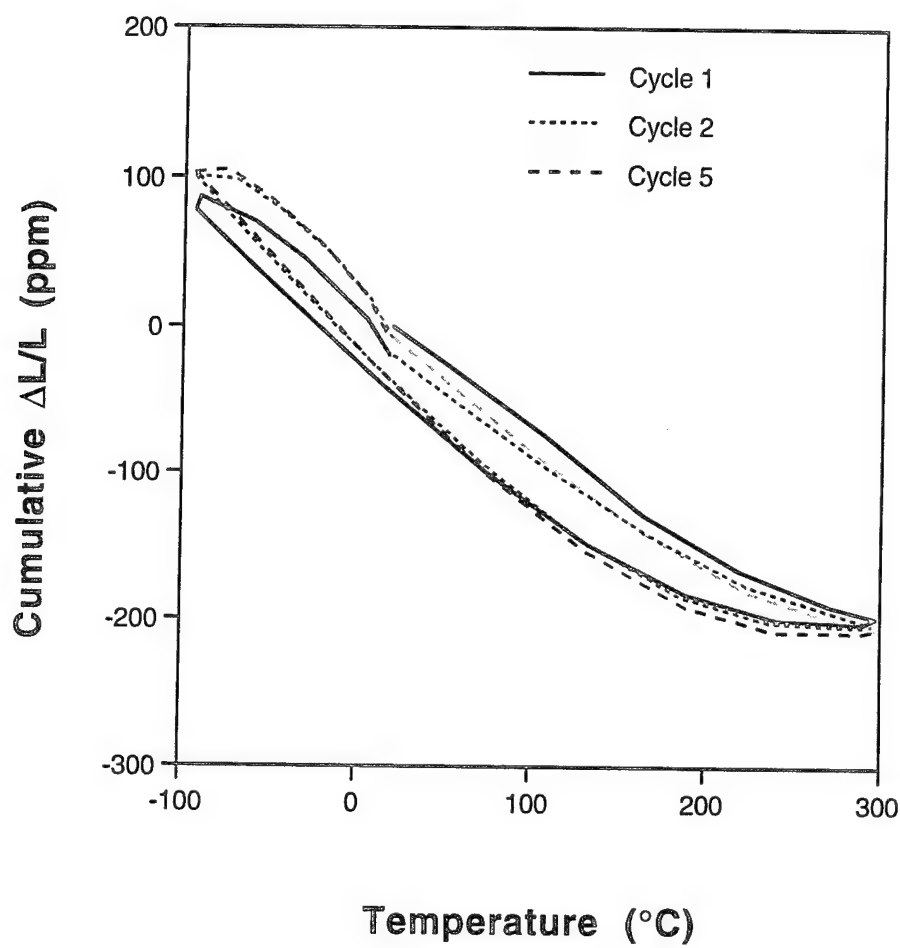


Figure III-10. Thermal strain vs. temperature for the $[0/90]_s$ reinforced P-100/BSG composite measured in the 0° direction. Cycles 1, 2, and 5 are shown in the figure.

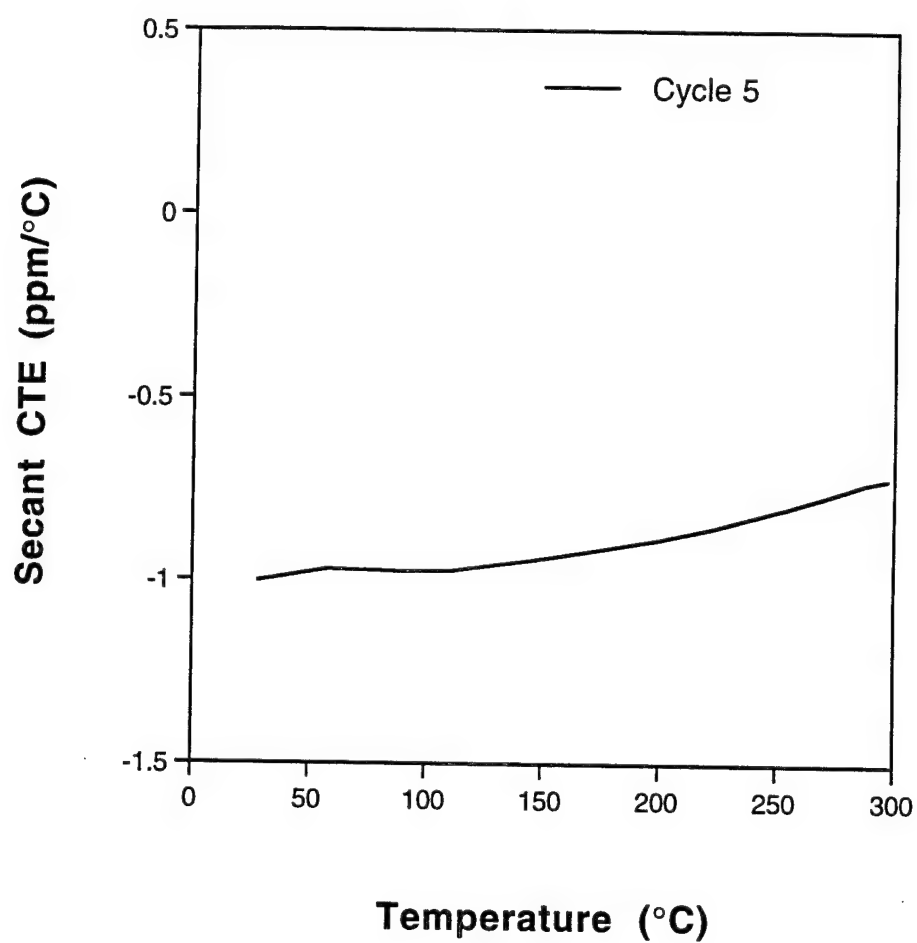


Figure III-11. Secant CTE vs. temperature for the $[0/90]_s$ reinforced P-100/BSG composite measured in the 0° direction. The curve shown corresponds to the initial heating portion of Cycle 5.

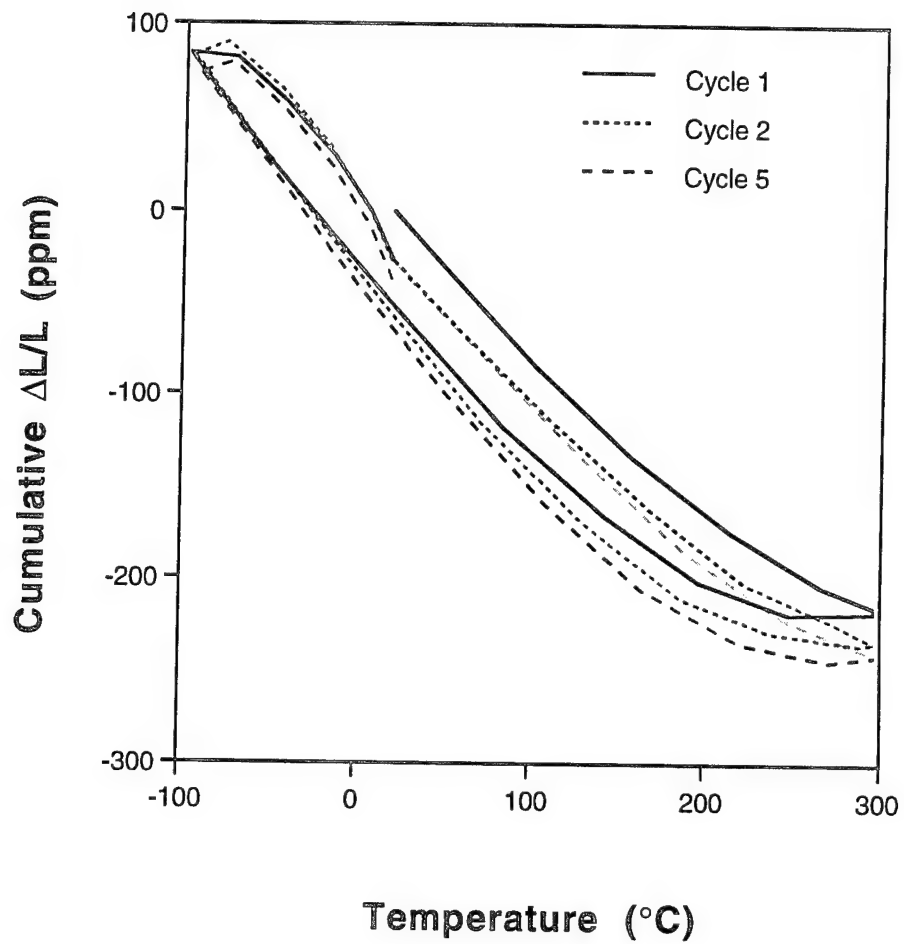


Figure III-12. Thermal strain vs. temperature for the $[0/\pm 60]_s$ reinforced P-100/BSG composite measured in the 0° direction. Cycles 1, 2, and 5 are shown in the figure.

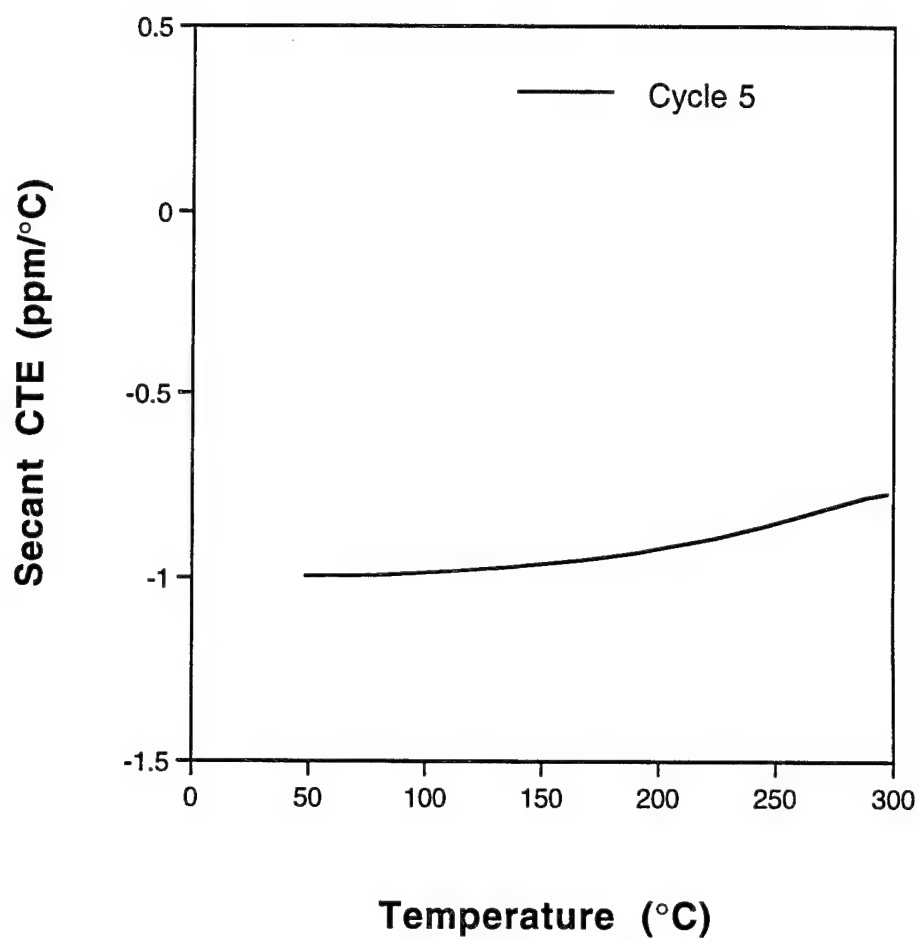


Figure III-13. Secant CTE vs. temperature for the $[0/\pm 60]_s$ reinforced P-100/BSG composite measured in the 0° direction. The curve shown corresponds to the initial heating portion of Cycle 5.

IV. DETAILED DESIGN OF C/GLASS COMPOSITES FOR DSPSE SATELLITE STIFFENERS

(Performed and reported by MSNW, Inc)

SUMMARY

This program builds upon the results of a previous survey of potential applications for graphite/glass composites in spacecraft, Reference 1. The results of the previous survey showed that graphite/glass material can offer weight savings and structural improvements in the stiffeners, longerons, and shear panels of the Deep Space Program Scientific Experiment (DSPSE) spacecraft. The original DSPSE design used an octagonal frame of longerons and stiffeners covered with sandwich panels to form decks and sidewalls. The original spacecraft was fabricated primarily of aluminum and was designed as a functional and inexpensive test bed for a variety of sensors and communications equipment.

The purpose of the program described in this report was to develop a detailed design of a P100/Borosilicate Glass (P100/BSG) stiffener for the DSPSE satellite. The program included the development of a material property database, finite element analysis of the spacecraft, sizing of the stiffener attachment regions, and specification of the prototype stiffener design. The study was based upon actual design requirements obtained from DSPSE satellite designers at the Naval Research Laboratory (NRL). Each potential design configuration was analyzed to determine the response to various acceleration loads and thermal cycles. The designs were evaluated in terms of minimum margins of safety and potential weight savings.

The detailed design of a P100/BSG stiffener for the DSPSE satellite resulted in several important conclusions and recommendations. A material property database was developed to support the design study on both unidirectional and quasi-isotropic (0/±45/90) P100/BSG laminates. The database includes bearing

strengths as well as longitudinal tensile, compressive, and thermal expansion properties which were critical to the satellite design. Comparisons of measured and computed properties showed that the test and modeling results agree well if, as explained in Reference 1, the matrix properties include the effects of microcracking caused by residual stresses. The fact that the experiments and theory agree implies that the material is well understood and mature enough to transition to realistic structural applications.

The material property database was used to determine preliminary B-basis design allowables for the tensile strength of two different unidirectional P100/BSG composites. The B-basis allowables were found to be 55.5 ksi for material that included graphite scrim and 68.2 ksi for material without scrim. These values represent preliminary B-basis values because the database contained less than 40 values, which does not satisfy the requirements for a true B-basis allowable. Nevertheless, the data exhibit a relatively low standard deviation so these preliminary B-basis allowables represent reasonable values for the design strengths. The fact that the B-basis calculations result in reasonable design values implies that the material is fairly repeatable and mature.

An optimized P100/BSG stiffener for the DSPSE spacecraft was designed based upon realistic design loads supplied by NRL. Detailed finite element analyses were performed to evaluate forces and stresses caused by liftoff accelerations, orbital transition accelerations, and temperature cycles. Four different design configurations were analyzed including aluminum (Design A), 0° P100/BSG stiffeners in an aluminum structure (Design B), 0° P100/BSG stiffeners in a graphite/epoxy structure (Design C), and 0/±45/90 P100/BSG stiffeners in a graphite/epoxy structure (Design D). The results showed that, in general, most of the forces in the spacecraft are carried by the stiffeners, longerons, and subfloor of the frame. The sidewall and deck panels carry low stresses and

primarily act to transmit the equipment and fuel loads into the frame. Typical mechanical stresses in the DSPSE satellite are relatively low. In all of the configurations analyzed, the highest acceleration induced in-plane stresses were less than 5 ksi. Similarly the highest shear stresses caused by the acceleration loads were less than 3 ksi. On the other hand, thermally generated stresses, caused by the mismatch in thermal expansion coefficients, were found to be significant. In particular the thermally induced loads were found to result in high localized bearing stresses at the attachments. Design D, which uses quasi-isotropic P100/BSG stiffeners in a structure made from graphite/epoxy longerons and shear panels, was found to minimize the thermal stresses and result in positive margins of safety for all mechanical and thermal loads. The P100/BSG stiffener weighs 3 pounds less than the aluminum component, which represents a 20 percent weight savings in the stiffeners. The use of P100/BSG stiffeners, graphite/epoxy panels, and graphite/epoxy longerons results in an overall structural weight savings of 30 percent when compared to the all-aluminum baseline design.

A drawing of the recommended stiffener design is provided in Figure 18. The recommended stiffener uses a 0/±45/90 P100/BSG material in an angle-iron configuration with flanges that are 1.312 inches long and 0.125 inch thick. The P100/BSG stiffener should be attached to the surrounding structure using 0.375 inch diameter bolts as shown in the detail of Figure 18. It is recommended that stiffeners using this design be fabricated and supplied to NRL for flight qualification testing.

DETAILED DESIGN OF GRAPHITE/GLASS COMPOSITES
FOR DSPSE SATELLITE STIFFENERS

BACKGROUND

A previous Phase I Small Business Innovative Research (SBIR) program funded by the Ballistic Missile Defense Organization (BMDO) assessed potential applications for graphite/glass composites in satellite thermal and structural components, Reference 1. Graphite/glass materials, which have been developed extensively at United Technologies Research Center (UTRC), possess several characteristics that make them particularly attractive for satellite applications. These composites exhibit excellent dimensional stability with high specific stiffness and near zero thermal expansion coefficients. Graphite/glass composites made with high conductivity pitch fibers have resulted in measured specific thermal conductivities that exceed the value of copper. The materials have shown high fiber dominated strengths and matrix dominated strengths that can be tailored by using reinforcing scrim to increase reliability. Graphite/glass composites can be used at temperatures approaching 1000°F, they do not outgas, and they showed no degradation when retrieved from the Long Duration Exposure Facility (LDEF) experiment, Reference 2. The fabrication techniques for the material are well developed so composites can be made with very thin plies and easily tailored properties. A variety of structural shapes have been demonstrated and tested including panels, tubes, and open channels.

The Phase I SBIR program, Reference 1, examined a variety of materials and satellite components. The components included radiator fins, electronic heat sinks, thermal doublers, battery sleeves, solar array substrates, longerons, stiffeners, and shear panels. The materials consisted of unidirectional K1100/Borosilicate Glass (BSG), unidirectional P100/BSG, [0/90] K1100/BSG, [0/90] P100/BSG, and [0/±60] P100/BSG. The results of

Reference 1 showed that the most attractive applications of graphite/glass composites were in the longerons, stiffeners, and shear panels of the Deep Space Program Scientific Experiment (DSPSE) satellite, which is shown in Figure 1a.

The DSPSE satellite is being developed as a test bed for a variety of BMDO sensors and is based upon a relatively inexpensive and functional structural platform. As shown in Figure 1a, the structural skeleton consists of longerons, stiffeners, and a structural subfloor that form an octagonal frame. The frame supports a top panel, called the thruster panel, a mid deck panel, and outer sidewall panels. All of the panels are sandwich structures with top and bottom skins attached to an aluminum honeycomb core. The panels support a variety of nonstructural equipment including fuel tanks, sensors, reaction wheels, and electronic instruments. The first generation DSPSE satellite, called Clementine, used aluminum as the structural material for the frame and panels. A subsequent DSPSE design employs graphite/epoxy facesheets for the deck and sidewall panels. The revised DSPSE design also uses reinforced graphite/epoxy regions to form the vertical edges of the sidewall panels, which replace the aluminum longerons.

The stiffener shown in Figure 1b was chosen as the focus of this design effort because preliminary sizing calculations showed that graphite/glass composites can result in weight savings of 10 to 80 percent over aluminum depending upon the design requirements. Additionally, fabrication of the angle-iron shape required for the stiffeners had already been demonstrated in a previous UTRC program, Reference 3. As shown in Figure 1b, the DSPSE stiffener is 18.6 inches long with two perpendicular flanges that are each 1.312 inches long and 0.125 inch thick. The stiffeners provide horizontal reinforcement to the frame and serve as attachment points for the decks and sidewalls. The P100/BSG family of

graphite/glass composites was selected as the stiffener material since it offered a good balance of strength and stiffness.

OBJECTIVES

The primary objective of the stiffener design effort was to specify the material, geometry, and attachment details of a P100/BSG stiffener suitable for use in a DSPSE satellite. In order to specify the design it was necessary to measure the mechanical properties of potential materials and develop a design database. Thus, one goal of the program was to define a test matrix and cutting plan for the experimental effort. It was also necessary to develop a detailed understanding of the internal stresses and load paths in the satellite caused by operating conditions. Therefore, a second goal of the program was to develop and exercise a detailed finite element model of the satellite and evaluate the stresses caused by acceleration loads and thermal cycles. Finally, once the local forces were known it was necessary to size the attachment regions, specify bolt diameters, and define thicknesses, which would prevent failure at the joints.

The design requirements and weight goals for the DSPSE satellite were obtained from the spacecraft designers at the Naval Research Laboratory, Reference 4, and are summarized in Table 1. As shown in Table 1, the satellite is designed for operation in low earth orbit and must have a minimum life of five years. The outgassing requirements call for a maximum mass loss less than one percent. Additionally, less than 0.1 percent of the mass loss can be in the form of collected volatile condensable material. The liftoff forces include an 8.5 G axial acceleration and a 3.5 G lateral acceleration. An orbital transition maneuver will impose an 11.0 G axial acceleration coupled with a 100 rpm rotational acceleration. The temperature extremes caused by the orbital cycle will vary from a low of -15°C (5°F) to a high of 50°C (122°F). The

satellite will be assembled at room temperature so the stress-free temperature was assumed to be 75°F.

The calculated weights for the spacecraft, presented in Table 1, show a dry satellite weight of 486 pounds. This includes 100 pounds of structural weight for an aluminum frame and panels. The remaining dry weight consists of electronics, reaction wheels, sensors, and batteries. The weight of the on-board fuel is 450 pounds, which results in a total weight of 936 pounds for a fueled satellite. The orbital transition maneuver utilizes an expendable motor which is external to the spacecraft. The mass of 936 pounds was used in the stress calculations representing liftoff and transition accelerations.

MATERIAL PROPERTY DATABASE

As outlined in the previous section it was necessary to measure the critical mechanical and thermal properties of the P100/BSG composites in order to design the stiffener. The following sections describe the test plan, the experimental data, and the development of approximate B-basis allowable strengths and summarize the material properties employed in the design.

Test Plan

The test matrix for the P100/BSG stiffener materials is detailed in Table 2. The table includes the original planned experiments (shown in parentheses) and the final tests that were performed. One of the materials evaluated in the test matrix was a unidirectional P100/BSG that utilized graphite scrim (about 4 percent by volume) to provide transverse strength. The unidirectional material was envisioned as the primary stiffener structural material and was therefore tested for axial tension, axial compression, and axial thermal expansion. As shown in Table 2, measurements for room temperature axial tension and for axial

thermal expansion of this material were made in Reference 1 and were incorporated in the design database. The second material configuration that was evaluated in this program was a ± 45 P100/BSG that also contained the graphite scrim. This material was tested in axial tension following the procedures detailed in ASTM D 3518, Reference 5, in order to determine the longitudinal shear modulus of the unidirectional material. The third material tested was a quasi-isotropic $0/\pm 45/90$ P100/BSG laminate that was envisioned as a material for local reinforcement at the attachment regions. Since the quasi-isotropic material was planned for joint locations, it was tested for axial tension, compression, and bearing. The test plan also called for the measurement of thermal expansion of the quasi-isotropic material. These tests were eliminated because the experimental apparatus was being refurbished and data on $0/90$ and $0/\pm 60$ P100/BSG composites (which have identical thermal expansions to a $0/\pm 45/90$ laminate) were available in Reference 1.

All of the test specimens were designed to be approximately 0.056 inch thick. This resulted in the use of twelve plies in the materials which included scrim (0° and $\pm 45^\circ$ laminates), and 16 plies in the $0/\pm 45/90$ laminates. When the actual satellite temperature extremes of 5°F to 122°F became known, it was decided to eliminate the planned tests at 250°F and -250°F and to increase the number of replications of each test at room temperature to five. Additional details of the test matrix including specimen dimensions and cutting plans are provided in an appendix to this report.

Experimental Data

The experimental data measured on both the unidirectional and quasi-isotropic materials are summarized in Tables 3 through 6, which show the tensile, compressive, shear, and bearing properties, respectively. Each table identifies the composite constituents, laminate configuration, average panel thickness, fiber volume

fraction, specimen designation, ultimate strength, modulus, ultimate strain, and yield strength. The tables include the data measured for each replication as well as averages and standard deviations. As will be discussed in subsequent sections, the tests resulted in material properties that were very close to expected values.

The unidirectional P100/BSG shear properties shown in Table 5 were computed from tensile properties measured on $\pm 45^\circ$ laminates following the procedure described in ASTM specification D3518M-91, Reference 5. As described in the specification, tensile data from a ± 45 laminate can be used to determine the in-plane shear response of a unidirectional composite. The measured loads and strains on the ± 45 laminate are related to the shear stresses and strains in a unidirectional composite by the following relations:

$$\tau_i = \frac{P_i}{2wt} \quad (1)$$

$$\gamma_i = \epsilon_i^x - \epsilon_i^y$$

where P represents the load, w is the specimen width, t is the specimen thickness, ϵ^x is the measured longitudinal strain, and ϵ^y is the measured Poisson strain with contraction taken as a negative number. The subscript i refers to values at any particular load increment. The shear modulus is then determined as

$$G_i = \frac{\tau_i}{\gamma_i} \quad (2)$$

and the ultimate shear strength is computed as

$$\tau_{ult} = \frac{P_{ult}}{2wt} \quad (3)$$

Using expressions for Young's modulus and ultimate strength,

$$E = \frac{\sigma}{\epsilon} = \frac{P_i}{wt\epsilon_i^x} \quad (4)$$

$$\sigma_{ult} = \frac{P_{ult}}{wt}$$

and the fact that the Poisson strain is $\epsilon_i^y = -\nu_{xy}\epsilon_i^x$, the expressions for shear modulus and strength can be written in terms of the measured tensile modulus and strength

$$G = \frac{E}{2(1+\nu)} \quad (5)$$

$$\tau = \frac{\sigma}{2}$$

In these calculations, ν was taken as 0.723, which represents the computed in-plane Poisson's ratio for a ± 45 P100/BSG laminate. The expressions identified as Equation (5) were used to determine the unidirectional shear properties summarized in Table 5.

The bearing data summarized in Table 6 were measured using the specimen configuration that is included with the table. The quasi-isotropic P100/BSG bearing specimen was approximately 1.50 inches wide and 0.060 inch thick. The hole diameter was 0.375 inch and the center of the hole was located about 0.725 inch from the free edge. A shoulder bolt was used with a nut torqued to finger tightness. The load identified in Table 6 as P_{init} represents the force at which the first noticeable nonlinear deflection occurred. Continued loading beyond this point resulted in a characteristic "sawtooth" load-deflection curve. Beyond the point of initial failure it appears that the edge of the hole is damaged, which allows the test specimen to deform until the bolt bears upon undamaged material. At that point the load increases until the undamaged material fails locally; then the load drops, the bolt translates, and the process continues.

The bearing strength, summarized in Table 6, was computed as

$$\sigma_{br} = \frac{P_{init}}{Dt}, \quad (6)$$

where D is the hole diameter and t is the plate thickness.

The tensile properties summarized in Table 3 show that the unidirectional composite exhibited an average longitudinal tensile modulus of 48.1 Msi and an average longitudinal tensile strength of 65.6 ksi. The results for the quasi-isotropic (0/±45/90) laminate show that the average longitudinal tensile modulus was 20.1 Msi and the average longitudinal tensile strength was 33.2 ksi. Similar results for the compressive, shear, and bearing properties can be taken from Tables 4, 5, and 6, respectively.

The measured properties are compared to theoretically projected properties in Figures 2 and 3. Figure 2 shows the comparison of moduli and Figure 3 shows the comparison of strengths. The theoretically projected properties are summarized in Table 7c. The theoretical properties were calculated using the constituent properties shown in Tables 7a and 7b, which were determined from data correlation studies reported in Reference 1. Note that the calculated composite properties use the fiber volume fractions that match the fiber contents of the actual composites (46.1 percent for unidirectional specimens and 48.7 percent for 0/±45/90 specimens).

The comparisons of theoretical versus measured moduli are summarized in Figure 2, where Figure 2a shows the results in tension, Figure 2b shows the results in compression, and Figure 2c shows the results in shear. The comparisons show that the model tends to agree well with the tensile modulus while it slightly underpredicts the compressive modulus. The discrepancy in the compressive modulus is because the model includes degraded matrix properties to simulate the effects of microcracking. Since the

matrix cracks close under compressive loading, the actual composite will be stiffer than the projected theoretical properties. The model also slightly overestimates the shear modulus of the composite, which is probably due to the uncertainty in the shear modulus of the P100 fiber.

The comparisons of measured versus computed strengths are summarized in Figure 3, where Figure 3a presents tensile strengths, Figure 3b presents compressive strengths, and Figure 3c presents shear strengths. In most cases, the theoretical results lie within the scatter of the data. It can be seen that some predictions tend to be high while others are slightly low. This implies that modeling modifications to improve the prediction for one laminate will degrade the calculations of the strengths of the other laminate. Thus, the model appears to represent a consistent and fairly accurate estimate of composite strengths.

In general, the data and theory show fairly good agreement. These results imply that the experimental materials resulted in expected properties and that the composite model, which has been used in the study to supplement the test data, was reasonably accurate.

Preliminary B-basis Design Allowables

Satellite designers who work with homogeneous metals are accustomed to utilizing B-basis design allowable strengths, Reference 6. By definition, a B-basis strength is a statistically determined value such that at least 90 percent of the population is expected to equal or exceed the B-basis value with a confidence of 95 percent. In other words, designers treat B-basis allowables as minimum expected material strengths.

The determination of a B-basis value depends upon the scatter in the experimental data and the number of data points in the

population. Generally, a data set for homogeneous metals that contains a large number of data points and exhibits a low standard deviation will result in a B-basis strength that is lower than, but relatively close to, the average of the data. Alternatively, developmental materials like graphite/glass composites may exhibit significant scatter in measured properties and may have a relatively limited database. Thus, there was a concern prior to the analysis that the B-basis strengths determined for the graphite/glass composites would be too low to yield practical structural designs. Nevertheless, a preliminary B-basis allowable was computed as an aid to designers.

The B-basis strength calculations focused upon the tensile strength of unidirectional P100/BSG for two reasons. First, the material was found in Reference 1 to be an attractive stiffener material and was therefore one of the selected materials on this program. Second, because of previous studies, it was possible to collect a relatively large database of 34 points on the material.

The procedures used to determine the B-basis strengths follow the methods outlined in Reference 6. In order to determine a true B-basis allowable, a minimum of 100 data points is required if the population can be shown to have a normal distribution. If the population has an unknown statistical distribution, then a minimum of 300 data points is required. Since the P100/BSG data were evaluated using accepted procedures but limited to 34 values, the results have been referred to as "preliminary" B-basis strengths.

The total data set of 34 tensile measurements is summarized in Table 8. The table includes the designation of each specimen, the fiber volume fraction, measured composite tensile strength and modulus, calculated fiber strength and modulus, and a brief description of the test conditions. The computed fiber strength was determined by dividing the composite strength by the fiber volume fraction and the calculated fiber modulus assumed rule of

mixtures behavior and a glass matrix modulus of 3.2 Msi (taken from Table 7a). As shown in Table 8, the data were partitioned using engineering judgement into five groups that reflected specific characteristics. These five groups were identified as 1) as-fabricated, 2) annealed, 3) humidity, 4) scrim, and 5) thermal cycles. The details of each grouping are defined in the table, which also includes the average and standard deviation for the entire data set.

In order to test the normality of the data, the measured strengths were ranked from low to high and plotted as shown in Figure 4a. Using the theoretical probabilities associated with a normal distribution, it was possible to determine the expected strength of each ranked data point. For example, the third smallest value in a population of 34 data points is theoretically expected to have a strength which is equal to the mean value minus 1.37 times the standard deviation, where the value of 1.37 is determined based upon the rank of the data point and the total number of values in the population. Figure 4a compares the actual measured strengths to the theoretically expected strengths. The comparison shows that the data set is probably not normal since the data points at the extreme ends of the set are relatively far away from the expected values.

In order to identify the possible outliers in the data, the characteristics of each of the five groups were plotted and compared as shown in Figure 4b. The figure compares the mean, maximum, and minimum values of each of the five data groups. The comparison shows that the groups representing as-fabricated, annealed, or humidity exposure fall in a relatively tight range around the overall mean of the data. On the other hand, the scrim data show strengths that are somewhat lower than the overall response and the thermally cycled data show strengths that are somewhat higher than the overall response.

Based upon these comparisons the scrim and thermally cycled materials were removed from the data set and the reduced data set of 23 values was checked for normality. A summary of the reduced data set is provided in Table 9 and the test for normality and comparison of group statistics are shown in Figure 5a and 5b, respectively. Figure 5a shows that the reduced data set is probably normal since the extreme values of the measured strengths fall much closer to the theoretically expected values. The comparison of the group characteristics presented in Figure 5b shows that the data from each of the subgroups, i.e. as-fabricated, annealed, and humidity exposure, can all be combined into one population without degrading the statistical parameters. This implies that annealing and exposure to humidity do not result in statistically significant changes to the composite tensile strength. Since the reduced data set of 23 points is probably normal, it is possible to compute a B-basis allowable as

$$B = \bar{X} - k_p s, \quad (7)$$

where \bar{X} represents the mean, k_p is the one-sided tolerance factor for 23 data points, Reference 6, and s is the standard deviation.

The computed B-basis allowable tensile strengths for the two data sets are summarized in Table 10. The table includes the number of values, a qualitative assessment of the normality, the mean, the standard deviation, the one-sided tolerance factor, and the B-basis strength for each data set. The results presented in the table show that the reduced data set with 23 data points is probably normal and can be represented by a preliminary B-basis strength of 68.2 ksi.

Since one of the materials of interest in the stiffener design was the unidirectional P100/BSG that used the scrim cloth, it was decided to measure additional data on this material so a B-basis strength could be determined. Table 11 presents a summary of all

measured longitudinal tensile strengths of 0° P100/BSG composites made with scrim. The table includes data tested on previous program plus five additional data points measured during this effort. The table shows that the mean for all the scrim data is 65.3 ksi and the standard deviation is 8.5 ksi. Because the standard deviation is 8.5 ksi for the scrim data and only 6.2 ksi for the reduced data set (Table 9), it is improper to apply the B-basis parameters for the reduced data to the scrim data. However, inspection of the scrim data shows that one data point, identified by a strength of 87.0 ksi, is much higher than the others and is therefore the cause of the high standard deviation. As shown in Table 11, if this one high strength value is removed, the mean value becomes 62.9 ksi and the standard deviation drops to 4.0 ksi. Since the scrim data set now has a standard deviation which is less than that of the reduced data set and since there are no obvious reasons for the statistical variations in the scrim material to be different from those of the material in the reduced data set, it can be argued that the scrim data are similar to the reduced data except that they exhibit a lower mean. Based upon this argument, the one-sided tolerance factor, k_B , from the reduced data set can be used with the mean and standard deviation of the scrim data to compute a preliminary B-basis strength for the scrim material of 55.5 ksi.

In summary, accepted statistical procedures were used to calculate preliminary B-basis allowables for the tensile strengths of two unidirectional P100/BSG composites. Because there are less than 100 available data points, the computed values can only be identified as preliminary B-basis strengths. In evaluating the data it was found that the complete data set is probably not normal. A reduced data set, which contained as-fabricated, annealed, and humidity exposure materials, was found to be normal. Using the reduced data set, it was possible to define a preliminary B-basis allowable of 68.2 ksi for the tensile strength of

unidirectional P100/BSG composites. Similar material that contains scrim layers was found to exhibit a lower average strength and lower standard deviation. The calculated preliminary B-basis allowable for the tensile strength of unidirectional P100/BSG that contains scrim was found to be 55.5 ksi.

Properties Used in Stiffener Design

A summary of the material properties used in the stiffener design is shown in Table 12. The table encompasses aluminum, quasi-isotropic T300/epoxy, unidirectional P100/BSG, and quasi-isotropic P100/BSG. The table includes longitudinal and transverse properties and contains the moduli, thermal expansion coefficients, densities, and strengths used in the design. The graphite/epoxy composite was assumed to have a fiber volume fraction of 60 percent. The moduli of the P100/BSG composites were computed assuming a fiber volume fraction of 40 percent and using the constituent properties shown in Tables 7a and 7b. The strengths of the P100/BSG composites were taken from the test data discussed in the previous sections. For example, the longitudinal tensile strength of the unidirectional P100/BSG with scrim was taken as 55.5 ksi, reflecting the results of the B-basis allowable analysis.

DETAILED STRUCTURAL ANALYSIS

Once the material property database was compiled it was possible to perform the detailed structural analysis of the DSPSE spacecraft to determine the mechanical performance of the graphite/glass stiffeners under realistic loading conditions. The following sections describe the spacecraft geometry, the finite element model, the design configurations that were analyzed, examples of the thermostructural response, computed margins of safety, and computed weight savings.

DSPSE Geometry

As shown in Figure 1, the DSPSE spacecraft structure includes an octagonal frame with honeycomb sandwich panels which form the decks and sidewalls. The details of the dimensions of the structural members were obtained from Reference 4 and are shown in Figures 6 through 9. Figure 6 shows the structural frame including longerons, stiffeners, and sandwich panels. As shown in Figure 6, the mid deck and thruster deck panels are 1.00 inch high with facesheets that are 0.025 inch thick. The sidewall panels are 0.250 high with facesheets that are 0.020 inch thick. All deck and sidewall panels employ 1/8 5052-.007 aluminum honeycomb. The overall dimensions of the frame are shown in Figure 7, which includes the longerons, stiffeners, and subfloor beam. As shown in the figure the frame is 43.2 inches high and the mid deck is located 19.9 inches from the base. The total width of the frame is 45.1 inches resulting in equal octagonal sides of 18.6 inches.

The details of the subfloor beam including the cross-section are shown in Figure 8. The subfloor beam is shaped like a tic-tac-toe board and has a total width of 45.1 inches. The length of each octagonal side is 18.6 inches. As shown in Figure 8, this results in a span of 13.2 inches for each of the extensions of the subfloor. The subfloor has an I-beam cross-section, Figure 8, with a total height of 3.00 inches and total width of 2.00 inches. The top and bottom flanges are 0.125 inch thick and the shear web is 0.188 inch thick. The figure shows that the height of the subfloor beam tapers from 3.00 inches to 1.50 inches at the ends of the extensions. In the model, the subfloor beam was assumed to maintain a constant depth of 3.00 inches along the entire length.

Typical dimensions of the longerons and stiffeners are shown in Figure 9. The longerons are approximately 43.2 inches long and have a three-flange cross-section as shown in Figure 9. Each flange is 1.312 inches long and 0.125 inch thick. The angle

between adjacent flanges is 67.5 degrees. The stiffeners are 18.6 inches long and have an angle-iron cross-section. Each flange of the stiffener is 1.312 inches long and 0.125 inch thick.

The structural properties of the subfloor, longerons, and stiffeners are summarized in Table 13, which includes the cross-section areas, torsional moment of inertia, bending moments of inertia, and distances from the neutral axes to the extreme fibers. The geometric characteristics shown in Table 13 were used to represent the frame members as three-dimensional beam elements in the spacecraft structural model. Note that two longerons are identified in Table 13 and referred to as longeron-left and longeron-right. The local principal axes of the longerons are not aligned with the principal axes of the spacecraft, so the table includes rotated moments of inertia to reflect the local longeron orientations.

Finite Element Model

A schematic diagram of the finite element model is shown in Figure 10. As shown in the figure, the model employs beam and shell elements to simulate a one-quarter symmetric slice of the spacecraft. The model uses 280 elements and 248 nodes for a total of 1488 possible degrees of freedom. The density of the facesheets of the panels was artificially increased to simulate the weight of the equipment and fuel mounted on the panels and subjected to the acceleration loads. The analysis was performed using COSTAR (COMposite STRuctural Analysis Routine), which is a commercial finite element code developed specifically to analyze composite structures, Reference 7.

Boundary conditions were applied to simulate appropriate deformations during the loading cycles. For axial and rotational accelerations the x-z and y-z faces, shown in Figure 10, represented planes of symmetry. Under acceleration loading the

base of each longeron was rigidly fixed to simulate attachment to the launch vehicle. During lateral acceleration in the x-direction the x-z face was treated as a plane of symmetry and the base of each longeron was clamped, as before. However, the nodes on the y-z face were allowed to move laterally in the x-direction by constraining the deformations at the y-z edge to be linked to one master node for each deck. Under thermal loading, the planes of symmetry were maintained at the x-z and y-z faces, but the spacecraft was assumed to be free of the launch vehicle so the base of each longeron was free to move laterally. The base of each longeron was still constrained axially to eliminate rigid body motion.

The model was developed and debugged by checking the geometry and running test cases on simple beam and shell problems. The structural weights of the components of the MSNW model were compared to similar data taken from an NRL model, Reference 4. The weight comparisons are presented in Table 14, which shows that the total weight of the MSNW model is within 7 percent of the value provided by NRL. These results are based on a fully aluminum design and show that the finite element model is very similar to the version used by NRL. Note that the total spacecraft structural weight is approximately 100 pounds.

Design Configurations

After the model was developed and verified, it was used to analyze four design configurations defined in Table 15 and referred to as A, B, C, and D. The table identifies the material used in the components of each design. Design A represents the baseline configuration and uses aluminum longerons, stiffeners, and panels. In Design B, unidirectional graphite/glass stiffeners are used in place of the aluminum stiffeners. In Design C, the panels and longerons are changed to quasi-isotropic graphite/epoxy to reflect modifications that NRL is considering for the next generation of

DSPSE satellites. Design C includes unidirectional P100/BSG stiffeners. Design D is identical to Design C except that the unidirectional P100/BSG stiffeners are replaced with quasi-isotropic P100/BSG stiffeners. Each of these configurations was analyzed for stresses caused by the liftoff accelerations, transition accelerations, and thermal cycles discussed previously and detailed in Table 1.

Thermostructural Response

Typical results of the structural and thermal loadings are shown in Figures 11 through 13, which portray the computed deformations of the baseline configuration (Design A). Figures 11, 12, and 13 show the deformations caused by the liftoff accelerations, the transition accelerations, and the thermal cycles, respectively. Each figure shows the original shape of the spacecraft (solid lines) and the deformed shape (dotted lines). The liftoff deformations presented in Figure 11 correspond to either axial, Figure 11a, or lateral, Figure 11b, motion at the base of the longerons. Under axial accelerations, the longerons are forced upward and the inertia of the equipment on the panels generates internal forces which lead to the bending deformations shown on the decks in Figure 11a. Similarly, the lateral acceleration of the longeron base generates inertial forces which result in the sideways deformation of the structure shown in Figure 11b.

The accelerations caused by the orbital transition maneuver include both an axial and a rotational acceleration. These loads result in the deformations shown in Figure 12, which presents both the deformations due to the axial acceleration, Figure 12a, and the deformations due to the rotational acceleration, Figure 12b. The axial deformations shown in Figure 12a are identical to those of Figure 11a except for the magnitude. The rotational deformations presented in Figure 12b show the outward bowing of the sidewalls caused by the inertia forces. Typical thermal deformations are

presented in Figure 13, which shows that the spacecraft grows proportionally under a temperature increase from 75°F to 122°F. Subsequent design calculations will evaluate the stresses caused by a thermal decrease (75°F to 5°F) since this represented the most severe portion of the thermal cycle.

An example of the typical forces and stresses computed by the model is shown in Figure 14, which presents a finite element plot of stress component 1 caused by liftoff axial accelerations in the baseline aluminum design. In the beam elements (i.e. longeron, stiffener, and subfloor), stress component 1 represents the axial force. In the shell elements (i.e. sidewall and deck panels), stress component 1 represents the in-plane shell force, N_{xx} . The results presented in Figure 14 show that the maximum internal forces are the axial forces at the base of each longeron where the inertia load of the spacecraft is transferred into the launch vehicle. The results show that the maximum force for this loading condition is about 66 pounds and that the forces and stresses in the structure are relatively low. The results also show that the primary loads are carried by the frame and that the stresses in the panels are almost insignificant. Similar observations were made for other design configurations and other loading conditions.

Margins of Safety and Weight Savings

Since the design study was primarily interested in the response of the stiffeners, the finite element results were used to compute local maximum stresses for each stiffener configuration and each loading condition. The finite element model results were surveyed to determine maximum nodal forces, shears, and moments in the stiffeners. The locations of the stiffener nodes are shown in Figure 15, in which the stiffeners are represented by the three rows of horizontal elements that run from nodes 18 to 28, 76 to

134, and 186 to 244. These nodal locations are referred to in subsequent tables of forces and stresses.

Summaries of the maximum stiffener forces and stresses computed by the finite element model are shown in Tables 16 through 19. Tables 16, 17, 18, and 19 show the results for design configurations A, B, C, and D, respectively. Each table shows the details of the design configuration and loading condition, along with the maximum stiffener loads and stresses. The loads include the axial force, F_1 , the two transverse shear forces, Q_2 and Q_3 , and the two bending moments, M_2 and M_3 . The torque loads on the stiffener were found to be insignificant and are not shown in the tables. Each entry shown in the tables represents the maximum stiffener force caused by the imposed accelerations or thermal cycle. The tables include nodal locations that refer to Figure 15 and that can be used to identify the position of the maximum forces.

Once the forces and moments were known, the maximum stresses in the stiffener were computed from beam theory

$$\sigma = \frac{F_1}{A} + \frac{M_{\max} t}{I} \quad (8)$$

and

$$\tau = \frac{3}{2} \frac{Q_{\max}}{A} \quad (9)$$

In these expressions F_1 , M_{\max} , and Q_{\max} represent the axial force, maximum shear, and maximum moment for each loading condition. The geometric properties for the stiffener, including area, moment of inertia, and distance from neutral axis, were taken from Table 13.

The results for the design configurations presented in Tables 16 through 19 show that the maximum stresses in the stiffeners are fairly low. The in-plane stresses caused by the acceleration

forces are less than 5 ksi. Similarly the shear stresses caused by the acceleration loads are less than 3 ksi. These stresses are acceptable since, as shown in Table 12, the P100/BSG laminates will exhibit minimum in-plane strengths of 28.5 ksi and minimum shear strengths of 6.7 ksi. The largest stresses are caused by the thermal cycle, which reflects the fact that the expansion coefficient of graphite/glass is much less than that of aluminum. As can be seen in Table 17, a unidirectional P100/BSG stiffener used in an aluminum design (Design B) will carry an in-plane compressive stress of 22.4 ksi when the satellite is cooled from 75°F to 5°F. This stress can be reduced to 5.7 ksi if the unidirectional stiffener is used in a graphite/epoxy design (Design C) as shown in Table 18. The thermal stress on the stiffener can be further reduced to 3.3 ksi if the unidirectional P100/BSG is replaced with quasi-isotropic P100/BSG (Design D) as shown in Table 19.

Once the stresses were known it was possible to compute margins of safety and weight savings for each design configuration. These results are summarized in Table 20, which includes the stresses, strengths, and margin of safety for each design configuration and loading condition.

The stresses caused by the orthogonal accelerations were combined in Table 20 to define the maximum in-plane, shear, and bearing stress in each component. The maximum stresses were computed, as prescribed in Reference 8, by finding the root mean square of the stresses computed for the independent axial and lateral accelerations. Table 20 presents the maximum values and includes the margins of safety for the in-plane stresses, shear stresses, and bearing stresses. The margin of safety was defined as

$$MS = \frac{\text{Strength}}{\text{Stress}} - 1 \quad (10)$$

which implies that a design with a positive margin will survive. The bearing stresses were computed as

$$\sigma_{bear} = \frac{F_1}{Dt} \quad (11)$$

where F_1 is the axial force shown in Tables 16 through 19, D is the bolt diameter, and t is the stiffener thickness. Here the bolt diameter was taken as 0.375 inch, which is reasonable in a flange that is 1.312 inches wide. The thickness, t , was taken as 0.125 inch as shown in Figure 9.

The results presented in Table 20 show that the computed margins of safety for the acceleration loads are all highly positive implying that the stiffener designs will easily survive the mechanical loads. The table shows negative margins of safety for the thermally induced bearing stresses in Designs B and C. Design B, which uses unidirectional P100/BSG stiffeners in an aluminum structure, exhibits a bearing stress margin of safety of -0.81. Design C, which uses unidirectional P100/BSG stiffeners in a graphite/epoxy structure, shows a bearing stress margin of safety of -0.25. These results imply that bearing failures may occur at the bolt holes in unidirectional stiffeners during thermal cycles. Fortunately, the bearing problem can be eliminated and an acceptable design can be developed by using quasi-isotropic P100/BSG as the stiffener material. This results in positive margins of safety for all loading conditions as shown in Table 20.

Table 20 also identifies the weight savings associated with each design configuration. The results show that 3 pounds of structural weight can be saved by replacing the aluminum stiffeners with P100/BSG stiffeners, Design B. The total weight of the aluminum stiffeners is about 15 pounds and the total weight of the P100/BSG stiffeners is about 12 pounds. This represents a 20 percent weight savings in the stiffeners and a 3 percent weight savings for the overall structure. Additional weight can be saved

by replacing the aluminum longerons and panels with T300/epoxy, as shown in Designs C and D. In these configurations the total weight savings includes 3 pounds due to the use of P100/BSG stiffeners and 27 pounds due to the use of T300/epoxy longerons and panels. This represents a weight savings of 20 percent in the stiffener components and a weight savings of 30 percent in the overall structure.

The minimum margins of safety taken from Table 20 are presented graphically in Figure 16. The figure shows the thermally induced bearing margins of safety which were found to be the critical stress component for each design. The figure shows the values of -0.81 for Design B, -0.25 for Design C, and +0.31 for Design D. Design A, which is the aluminum baseline configuration, is not included since the thermal stresses are identically equal to zero. The results clearly show that a quasi-isotropic P100/BSG stiffener, Design D, can survive the mechanical and thermal loads in the DSPSE spacecraft.

The weight savings associated with each design, which were shown in Table 20, are presented in Figure 17. The figure shows that Design D, which uses quasi-isotropic P100/BSG stiffeners and graphite/epoxy longeron and panels, will weigh 30 percent less than the baseline aluminum design. This weight savings includes 3 pounds which were saved by replacing the aluminum stiffeners with P100/BSG stiffeners. This 3 pounds weight savings represents a 20 percent savings in the stiffener weight.

RECOMMENDED STIFFENER DESIGN

The analytical results described above led to the recommended stiffener design shown in Figure 18. The stiffener is an angle-iron that is 18.6 inches long and fabricated from balanced and symmetric 0/±45/90 P100/BSG. The length of the flanges is 1.312 inches and the thickness of the flanges is 0.125 inch. Attachment

to the surrounding spacecraft structure is made using 0.375 inch diameter shoulder bolts that are centered in the flange. This results in a width-to-diameter ratio, w/d , of 3.5. At the ends of the stiffener the bolt holes can be located 0.75 inch or more from the edge resulting in a minimum edge-to-diameter ratio, e/d , of 2.0. The P100/BSG stiffener shown in Figure 18 can be used in a graphite/epoxy DSPSE satellite and will survive the mechanical and thermal loads in the spacecraft.

CONCLUSIONS AND RECOMMENDATIONS

The detailed design of a P100/BSG stiffener for the DSPSE satellite resulted in several important conclusions and recommendations. A material property database was developed to support the design study on both unidirectional and quasi-isotropic ($0/\pm 45/90$) P100/BSG laminates. The database includes measured bearing strengths as well as longitudinal tensile, compressive, and thermal expansion properties which were necessary for the satellite design. Comparisons of measured and computed properties showed that the test and modeling results agree well if, as explained in Reference 1, the matrix properties include the effects of microcracking caused by residual stresses. The fact that the experiments and theory agree implies that the material is well understood and mature enough to transition to realistic structural applications.

The material property database was used to determine preliminary B-basis design allowables for the tensile strength of two different unidirectional P100/BSG composites. The B-basis allowables were found to be 55.5 ksi for material that included a graphite scrim and 68.2 ksi for material without scrim. These values represent preliminary values, because the database contained less than 40 data points, which does not satisfy the requirements for a true B-basis allowable. Nevertheless, the data exhibit relatively little scatter so these preliminary B-basis allowables

represent reasonable values for design strengths. The fact that the B-basis calculations resulted in a reasonable design value also implies that the material is fairly repeatable and mature.

An optimized P100/BSG stiffener for the DSPSE spacecraft was designed based upon realistic design loads supplied by NRL. Detailed finite element analyses were performed to evaluate forces and stresses caused by liftoff accelerations, orbital transition accelerations, and temperature cycles. Four different design configurations were analyzed including all aluminum (Design A), 0° P100/BSG stiffeners in an aluminum structure (Design B), 0° P100/BSG stiffeners in a graphite/epoxy structure (Design C), and 0/±45/90 P100/BSG stiffeners in a graphite/epoxy structure (Design D). The results showed that, in general, most of the forces in the spacecraft are carried by the stiffeners, longerons, and subfloor of the frame. The sidewall and deck panels carry low stresses and primarily act to transmit the equipment and fuel loads into the frame. Typical mechanical stresses in the DSPSE satellite are relatively low. In all of the configurations analyzed, the highest acceleration induced in-plane stresses were less than 5 ksi. Similarly, the highest shear stresses caused by accelerations were less than 3 ksi. On the other hand, thermally generated stresses, caused by the mismatch in thermal expansion coefficients of the components, were found to be significant. In particular, the thermally induced loads were found to result in high localized bearing stresses at the attachments. Design D, which uses quasi-isotropic P100/BSG stiffeners in a structure made from graphite/epoxy longerons and shear panels, was found to minimize the thermal bearing stresses and result in positive margins of safety for all mechanical and thermal loads. The quasi-isotropic P100/BSG stiffener weighs 3 pounds less than the aluminum component, which represents a 20 percent weight savings in the stiffeners. The use of P100/BSG stiffeners, graphite/epoxy panels, and graphite/epoxy longerons results in an overall structural

weight savings of 30 percent when compared to the aluminum baseline design.

A drawing of the recommended stiffener design is provided in Figure 18. The recommended stiffener uses 0/±45/90 P100/BSG material in an angle-iron configuration with flanges that are 1.312 inches long and 0.125 inch thick. The P100/BSG stiffener should be attached to the surrounding structure using 0.375 inch diameter bolts as shown in the detail of Figure 18. It is recommended that stiffeners using this design be fabricated and submitted to NRL for flight qualification testing.

REFERENCES

1. K.W. Buesking and W.K. Tredway, "Graphite/Glass Composites for Satellite Thermal Applications," MSNW Final Report on NSWC Contract N60921-92-C-0101, December, 1992.
2. W.K. Tredway and K.M. Prew, "Analysis of the Effect of Space Environmental Exposure on Carbon Fiber Reinforced Glass," UTRC Report R91-112542, May 31, 1991.
3. P.H. McCluskey, W.K. Tredway, and K.M. Prew, "Fabrication of Carbon Fiber Reinforced Glass Composite Structural Elements," UTRC presentation at the 15th Annual Conference on Composites, Materials, and Structures, Cocoa Beach, FL, January 16-18, 1991.
4. W. Braun, "Stiffener Design Requirements," Data Package Received from Naval Research Laboratory, November 29, 1993.
5. "In-Plane Shear Stress-Strain Response of Unidirectional Polymer Matrix Composites," ASTM D3518M-91, Annual Book of ASTM Standards, Vol. 03:01, pp. 144-148.

6. "Metallic Materials and Elements for Aerospace Vehicle Structures," MIL-HDBK-5F, December 15, 1992.
7. J. Goering, "COSTAR, Composite Structural Analysis Routine," Matricks Software, Florissant, MO, 1989.
8. C.M. Harris and C.E. Crede, Shock and Vibration Handbook, McGraw-Hill, New York, 2nd ed., 1976, pg. 29-15.

Table 1. Design requirements for DSPSE spacecraft supplied by Naval Research Laboratory.

Environment	Altitude Lifetime	Low Earth Orbit
	Outgas mass loss	Minimum - 5 years Total < 1%, Condensable < 0.1%
Mechanical and Thermal Loads	Liftoff acceleration Orbital transition acceleration Thermal cycle	8.5 G axial, 3.5 G lateral 11.0 G axial, 100 rpm rotation -15°C to 50°C (5°F to 122°F, T ₀ =75°F)
Weights	Total spacecraft dry weight Structural weight (Aluminum) Propellant weight Total fueled spacecraft weight	486 lbs 100 lbs <u>450 lbs</u> 936 lbs

Table 2. Test matrix used to develop design database for P100/BSG satellite material.

Material/Component	Test & Direction	Temperature/Replications		
[0] ₁₂ with scrim Stiffener Material t=0.056 in	Axial Tension	-250°F	75°F	250°F
	Axial Compression	(3)	(3) 5	(3)
	Axial CTE	(3)	(3) 5	(3)
[±45] ₁₂ with scrim [45/0/-45/90] ₁₂ Attachment Material t=0.056 in	Axial Tension for In-Plane Shear	(2)*	→	
	Axial Tension	(3)	(3) 5	(3)
	Axial Compression	(3)	(3) 5	(3)
	Bearing	(3)	(3) 5	(3)
	Axial CTE	(2)	→	

* Data available from Phase I SBIR program, Reference 1.
(3) Numbers in parentheses refer to original test plan.

Table 3. Summary of experimentally measured tensile properties of P100/BSG satellite materials.

Fiber/Matrix	Layup	Thick (in)	ν_f (%)	Specimen	Ultimate Strength (Ksi)	Modulus (Msi)	Failure Strain (%)	Yield Strength (Ksi)
P100/BSG	0° w/ scrim	0.047	46.1	282-93-1	64.6	47.4	0.15	20.1
				-2	66.5	48.7	0.16	16.6
				-3	66.3	48.2	0.16	15.2
				-4	62.5	47.7	0.14	16.8
				-5	<u>68.1</u>	<u>48.4</u>	<u>0.15</u>	<u>22.5</u>
				Avg	65.6	48.1	0.15	18.2
				S Dev.	2.1	0.5	0.01	3.0
P100/BSG	0/45/90	0.060	48.7	285-93-1	33.4	21.6	0.18	4.5
				-2	34.2	20.9	0.20	2.8
				-3	32.1	19.5	0.19	2.9
				-4	33.0	20.0	0.20	3.3
				-5	<u>33.1</u>	<u>18.7</u>	<u>0.21</u>	<u>2.8</u>
				Avg.	33.2	20.1	0.20	3.3
				S Dev.	0.8	1.1	0.01	0.7

Table 4. Summary of experimentally measured compressive properties of P100/BSG satellite materials.

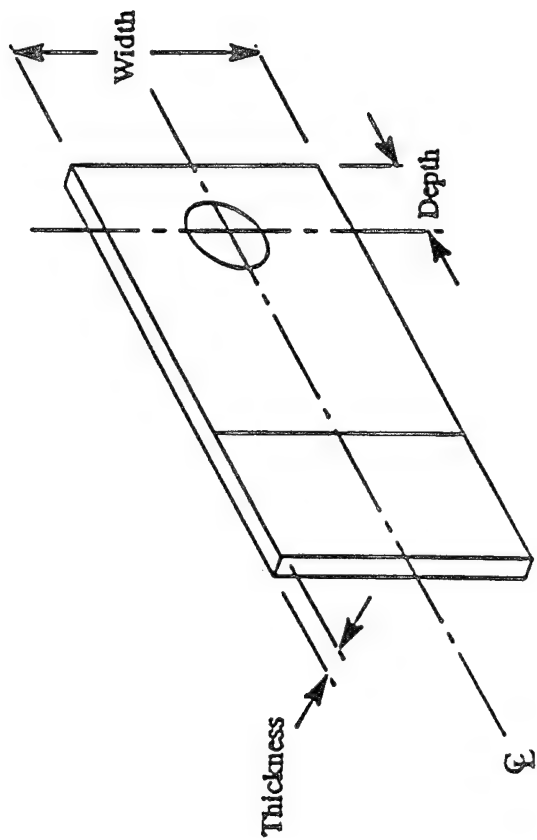
Fiber/Matrix	Layup	Thick (in)	ν_r (%)	Specimen	Ultimate Strength (Ksi)	Modulus (Msi)	Failure Strain (%)	Yield Strength (Ksi)
P100/BSG	0° w/ scrim	0.047	46.1	282-93-6	37.9	53.5	0.12	6.3
				-7	42.9	59.6	0.16	3.3
				-8	42.4	58.7	0.18	3.9
				-9	42.2	52.7	0.21	3.6
				-10	<u>43.3</u>	<u>55.2</u>	<u>0.16</u>	<u>4.0</u>
				Avg	41.7	55.9	0.16	4.2
				S Dev.	2.2	3.1	0.03	1.2
P100/BSG	0/45/90	0.060	48.7	285-93-6	25.2	20.4	0.47	2.2
				-7	25.8	23.6	0.49	1.9
				-8	35.1	27.2	0.55	2.4
				-9	30.4	26.1	0.42	2.4
				-10	<u>26.0</u>	<u>23.3</u>	<u>0.43</u>	<u>2.2</u>
				Avg.	28.5	24.1	0.47	2.2
				S Dev.	4.2	2.7	0.05	0.2

Table 5. Measured in-plane shear properties of unidirectional P100/BSG composite determined from tensile tests on ± 45 laminates.

Specimen Configuration				Measured $\pm 45^\circ$ Tensile Properties				0° Shear Properties*		
Fiber/Matrix	Laminate	Thickness (in)	ν_f (%)	Specimen Number	E (Msi)	σ_y (Ksi)	σ_{ult} (Ksi)	ϵ_{ult} (%)	G (Msi)	τ_{ult} (Ksi)
P100/BSG	[± 45] _N w/scrims	0.046	46.9	284-93-2	4.4	1.4	12.9	0.62	1.28	6.5
				-3	5.7	0.8	13.5	0.68	1.65	6.8
				-4	5.5	0.9	13.3	0.69	1.60	6.7
				-5	6.0	1.0	13.1	0.69	1.74	6.5
				-6	<u>6.5</u>	<u>0.6</u>	<u>13.6</u>	<u>0.66</u>	<u>1.89</u>	<u>6.8</u>
				Avg.	5.6	0.9	13.3	0.67	1.63	6.7
				S Dev.	0.8	0.3	0.3	0.03	0.23	0.2

* Shear properties computed following ASTM D3518 and using calculated Poisson's ratio of 0.723 for ± 45 P100/BSG laminate.

Table 6. Summary of experimentally measured bearing properties of P100/BSG satellite materials.



Fiber/Matrix	Layup	Specimen	P _{init} (lbs)	Hole Diameter (in)	Width (in)	Thickness (in)	Depth (in)	Bearing Strength (Ksi)
P100/BSG	0/45/90	285-93-11	420	0.375	1.491	0.058	0.731	19.3
		286-93-1	669	0.376	1.496	0.059	0.713	30.2
		-2	610	0.376	1.496	0.061	0.734	26.6
		-3	770	0.376	1.497	0.063	0.709	32.5
		-4	760	0.376	1.451	0.063	0.725	<u>32.1</u>
		Avg. S Dev.						28.1 5.5

Table 7. Theoretical properties of P100/BSG composites that were compared to experimental data. Properties of graphite fibers and glass matrix determined from data correlation studies on Phase I SBIR materials, Reference 1.

7a. Matrix Properties

Matrix	E (Msi)	ν	α ($10^{-6}/^{\circ}\text{F}$)	k (W/m $^{\circ}\text{K}$)	ρ (gm/cc)
BSG	3.20 *	0.22	1.77	1.06	2.25

* Modulus degraded to account for residual stress damage

7b. Fiber Properties

Fiber	E_f (Msi)	E_t (Msi)	G_s (Msi)	ν_a	ν_t	α_2 ($10^{-6}/^{\circ}\text{F}$)	α_t ($10^{-6}/^{\circ}\text{F}$)	k_s (W/m $^{\circ}\text{K}$)	k_t (W/m $^{\circ}\text{K}$)	ρ (gm/cc)
HM	46.7	1.55	4.05	0.26	0.36	-0.20	5.41	84	16	1.85
P100	100.0	0.50	2.50	0.26	0.70	-0.90	11.3	568	36	2.15
K1100X	115.0	0.50	2.50	0.26	0.70	-0.90	11.3	984	64	2.15

7c. P100/BSG composites

Material Configuration	Laminate Configuration	E_0 (Msi)	E_{90} (Msi)	$G_{0/90}$ (Msi)	ν_{0-90}	σ_0 ($10^6/^{\circ}\text{F}$)	σ_{90} ($10^6/^{\circ}\text{F}$)	ρ (lb/in 3)	σ_0^{tens} (ksi)	σ_0^{comp} (ksi)	σ_{90}^{tens} (ksi)	σ_{90}^{comp} (ksi)	$T_{0/90}$ (ksi)	K_0 (W/m $^{\circ}\text{K}$)	K_{90} (W/m $^{\circ}\text{K}$)
Stiffener Material	0° w/ Scrim $\nu_t = 46.1\%$	44.5	2.33	1.96	0.235	-0.770	3.60	0.081	71.1	56.7	5.70	11.4	6.27	239	2.34
Attachment Regions	0/±45/90 $\nu_t = 48.7\%$	18.8	18.8	7.29	0.286	-0.589	-0.589	0.081	30.4	24.2	25.7	20.5	16.1	140	140

Table 8. Complete data set (34 values) for tensile strength of unidirectional P100/BSG used in analysis of B basis design allowable.

Composite (-)	Fiber Volume (-)	Tensile Strength (Ksi)	Tensile Modulus (Msi)	Fiber Strength(c) (Ksi)	Fiber Modulus(d) (Msi)	Comments (-)
45-88	0.394	69.9	42.0	177.4	101.7	No scrim
45-88	0.394	78.1	47.3	198.2	115.1	No scrim
216-91-2	0.398	80.3	45.6	201.8	109.7	2" gage
216-91-3	0.398	82.1	48.5	206.3	117.0	2" gage
216-91-4	0.398	73.2	45.5	183.9	109.5	2" gage
23-91-1	0.432	78.8	46.7	182.4	103.9	As fabricated
23-91-8	0.432	77.4	46.5	179.2	103.4	As fabricated
142-92-1	0.460	78.3	53.5	170.2	112.5	No thermal cycles
142-92-2	0.460	73.8	54.1	160.4	113.9	No thermal cycles
216-91-9	0.398	86.8	49.0	218.1	118.3	1" gage, annealed 540°C, 60 min
216-91-10	0.398	91.5	47.9	229.9	115.5	1" gage, annealed 540°C, 60 min
216-91-11	0.398	94.2	49.4	236.7	119.3	1" gage, annealed 540°C, 60 min
216-91-6	0.398	82.2	48.3	206.5	116.5	1" gage, annealed 560°C, 30 min
216-91-7	0.398	80.2	46.7	201.5	112.5	1" gage, annealed 560°C, 30 min
216-91-8	0.398	83.1	47.9	208.8	115.5	1" gage, annealed 560°C, 30 min
216-91-12	0.398	72.4	46.5	181.9	112.0	1" gage, annealed 522°C, 138 min
216-91-13	0.398	77.6	44.3	195.0	106.5	1" gage, annealed 522°C, 138 min
23-91-2	0.432	76.3	49.2	176.6	109.7	Humidity, 547 hours (b)
23-91-4	0.432	75.7	47.5	175.2	105.7	Humidity, 547 hours (b)
23-91-6	0.432	84.1	47.2	194.7	105.1	Humidity, 547 hours (b)
23-91-3	0.432	87.9	48.6	203.5	108.3	Humidity, 1002 hours (b)
23-91-5	0.432	71.7	46.6	166.0	103.7	Humidity, 1002 hours (b)
23-91-7	0.432	86.9	44.8	201.2	99.5	Humidity, 1002 hours (b)
48-88	0.362	62.7	41.3	173.2	108.4	4% scrim
48-88	0.362	59.2	42.6	163.5	112.0	4% scrim
178-92	0.400	87.0	41.7	217.5	99.5	4.2% scrim
178-92	0.400	55.6	41.5	139.0	99.0	4.2% scrim
178-92	0.400	60.6	42.6	151.5	101.7	4.2% scrim
142-92-3	0.460	107.0	54.2	232.6	114.1	500 thermal cycles (a)
142-92-4	0.460	88.3	53.3	192.0	112.1	500 thermal cycles (a)
142-92-5	0.460	109.0	54.3	237.0	114.3	500 thermal cycles (a)
142-92-6	0.460	101.0	54.3	219.6	114.3	2000 thermal cycles (a)
142-92-7	0.460	84.0	54.8	182.6	115.4	2000 thermal cycles (a)
142-92-8	0.460	<u>109.0</u>	<u>54.5</u>	<u>237.0</u>	<u>114.7</u>	2000 thermal cycles (a)
Mean		81.4	47.9	194.1	110.0	
Std. Dev		12.74	4.11	24.98	5.79	

(a) Thermal cycle: -50°C to 150°C, 30 mins

(b) Humidity: 120°F, 95% RH

(c) Composite strength / fiber volume

(d) Rule of mixtures assuming matrix modulus is 3.2 Msi

Table 9. Reduced data set (23 values) for tensile strength of unidirectional P100/BSG used in analysis of B basis design allowable.

Composite (-)	Fiber Volume (-)	Tensile Strength (Ksi)	Tensile Modulus (Msi)	Fiber Strength(c) (Ksi)	Fiber Modulus(d) (Msi)	Comments (-)
45-88	0.394	69.9	42.0	177.4	101.7	No scrim
45-88	0.394	78.1	47.3	198.2	115.1	No scrim
216-91-2	0.398	80.3	45.6	201.8	109.7	2" gage
216-91-3	0.398	82.1	48.5	206.3	117.0	2" gage
216-91-4	0.398	73.2	45.5	183.9	109.5	2" gage
23-91-1	0.432	78.8	46.7	182.4	103.9	As fabricated
23-91-8	0.432	77.4	46.5	179.2	103.4	As fabricated
142-92-1	0.460	78.3	53.5	170.2	112.5	No thermal cycles
142-92-2	0.460	73.8	54.1	160.4	113.9	No thermal cycles
216-91-9	0.398	86.8	49.0	218.1	118.3	1"gage, annealed 540°C, 60 min
216-91-10	0.398	91.5	47.9	229.9	115.5	1"gage, annealed 540°C, 60 min
216-91-11	0.398	94.2	49.4	236.7	119.3	1"gage, annealed 540°C, 60 min
216-91-6	0.398	82.2	48.3	206.5	116.5	1"gage, annealed 560°C, 30 min
216-91-7	0.398	80.2	46.7	201.5	112.5	1"gage, annealed 560°C, 30 min
216-91-8	0.398	83.1	47.9	208.8	115.5	1"gage, annealed 560°C, 30 min
216-91-12	0.398	72.4	46.5	181.9	112.0	1"gage, annealed 522°C, 138 min
216-91-13	0.398	77.6	44.3	195.0	106.5	1"gage, annealed 522°C, 138 min
23-91-2	0.432	76.3	49.2	176.6	109.7	Humidity, 547 hours (b)
23-91-4	0.432	75.7	47.5	175.2	105.7	Humidity, 547 hours (b)
23-91-6	0.432	84.1	47.2	194.7	105.1	Humidity, 547 hours (b)
23-91-3	0.432	87.9	48.6	203.5	108.3	Humidity, 1002 hours (b)
23-91-5	0.432	71.7	46.6	166.0	103.7	Humidity, 1002 hours (b)
23-91-7	0.432	<u>86.9</u>	<u>44.8</u>	<u>201.2</u>	<u>99.5</u>	Humidity, 1002 hours (b)
Mean		80.1	47.5	193.7	110.2	
Std. Dev		6.23	2.56	19.23	5.60	

(b) Humidity: 120°F, 95% RH

(c) Composite strength / fiber volume

(d) Rule of mixtures assuming matrix modulus is 3.2 Msi

Table 10. Preliminary B basis allowable tensile strengths for 0° P100/BSG composites.

Data Set	n	Normality	Mean	Std. Dev.	k_B^a	B
-	-	-	(Ksi)	(Ksi)	-	(Ksi)
Composite	34	Poor	81.4	12.9	1.74	59.0
Composite	23	Good	80.1	6.37	1.87	68.2

^a One-sided tolerance factor for B basis allowable for n data points, $B = \bar{X} - k_B s$.

Table 11. Summary of tensile data on unidirectional P100/BSG composites that utilize graphite scrim.

Specimen	V_f	Tensile Strength	Comment
-	(%)	(Ksi)	-
48-88	36.2	62.7	4% Scrim
48-88	36.2	59.2	"
178-92	40.0	87.0	4.2% Scrim
178-92	40.0	55.6	"
178-92	40.0	60.6	"
282-93-1	42.1	64.6	Approx. 4% Scrim
-2	42.1	66.5	"
-3	42.1	66.3	"
-4	42.1	62.5	"
-5	42.1	<u>68.1</u>	"
Avg.		65.3	
S Dev.		8.5	
w/o 87.0 Ksi ^b			
Avg.		62.9	
S Dev.		4.0	

^b If high strength point is omitted from data, then scrim data fits within statistics of P100/BSG population. Using tolerance factor from full population, B basis strength for scrim data is 55.5 Ksi.

Table 12. Material properties used in design of DSPSE satellite with P100/BSG stiffeners.

Material	Layout	E_0 (Msi)	E_{90} (Msi)	ν	$G_{0/90}$ (Msi)	α_0 ($10^{-9}/F$)	α_{90} ($10^{-9}/F$)	ρ (lb/in ³)	σ_0^i (Ksi)	σ_0^c (Ksi)	σ_{90}^i (Ksi)	σ_{90}^c (Ksi)	τ (Ksi)
Aluminum	-	10.0	10.0	0.300	3.85	12.0	12.0	0.10	40.0	40.0	40.0	40.0	20.0
T300 Gr/Ep	0/45/90	5.21	5.21	0.320	1.97	2.55	2.55	0.06	30.0	48.9	30.0	48.9	24.4
P100/BSG	0 w/ scrim	41.9	3.20	0.189	1.95	-0.52	1.77	0.08	55.5	41.7	5.70	11.4	6.70
P100/BSG	0/45/90	15.9	15.9	0.284	6.21	-0.51	-0.51	0.08	33.2	28.5	33.2	28.5	16.1

Table 13. Geometric properties of three-dimensional beams used to represent frame members in DSPSE spacecraft model.

Frame Member	A (in ²)	K (10^{-3} in ⁴)	I_2 (10^{-2} in ⁴)	I_3 (10^{-2} in ⁴)	t_2 (in)	t_3 (in)
Subfloor Beam	1.02	7.46	84.2	16.8	1.00	1.50
Longeron - Left	0.492	2.36	6.52	14.5	1.212	0.926
Longeron - Right	0.492	2.36	14.5	6.52	0.926	1.212
Stiffener	0.312	1.69	5.13	5.13	0.937	0.937

Table 14. Comparison of structural weight of DSPSE satellite components from NRL and MSNW finite element models.

Component	NRL (lbs)	MSNW (lbs)
Subfloor Beam	22.0	17.7
Subfloor Stiffeners	1.5	4.5
Mid Deck Panel	12.2	12.6
Mid Deck Stiffeners	3.5	4.5
Thruster Deck Panel	6.5	12.6
Thruster Deck Stiffeners	3.2	4.5
Longerons	13.6	16.3
Sidewall Panels	30.2	27.2
Gussets	<u>0.6</u>	—
Total	93.3	99.9

Table 15. Summary of design configurations analyzed in study of P100/BSG stiffeners for DSPSE satellite.

Design	Panels	Longerons	Stiffeners	Comment
A	Aluminum	Aluminum	Aluminum	Baseline Design
B	Aluminum	Aluminum	0 P100/BSG	-
C	Gr/Ep	Gr/Ep	0 P100/BSG	NRL will use Gr/Ep in next generation
D	Gr/Ep	Gr/Ep	0/45/90 P100/BSG	-

Table 16. Computed maximum stiffener forces and stresses in design configuration A (all aluminum) of DSPSE satellite.

Run	Panel Mat'l	Long. Mat'l	Stiff. Mat'l	Load	Maximum Stiffener Loads										Max. Stress	
					Node	F ₁ (lbs)	Node	Q ₂ (lbs)	Node	Q ₃ (lbs)	Node	M ₂ (in-lbs)	Node	M ₃ (in-lbs)	σ (Ksi)	τ (Ksi)
1	Al	Al	Al	Lift Z	248	22.8	21	3.58	222	50.7	21	33.2	213	3.53	0.49	0.23
2	Al	Al	Al	Lift X	186	89.6	21	49.7	17	111	25	109	21	2.70	1.64	0.51
3	Al	Al	Al	Trans. Z	248	29.5	21	4.63	222	65.7	21	42.9	213	4.57	0.63	0.30
4	Al	Al	Al	Trans. Rot.	76	82.1	21	88.2	222	11.1	186	11.9	26	3.89	0.40	0.40
5	Al	Al	Al	Thermal	-	0.0	-	0.0	-	0.0	-	0.0	-	0.0	0.0	0.0

Table 17. Computed maximum stiffener forces and stresses in design configuration B (aluminum panels and longerons, 0° P100/BSG stiffeners) of DSPSE satellite.

Run	Panel Mat'l	Long. Mat'l	Stiff. Mat'l	Load	Maximum Stiffener Loads										Max. Stress	
					Node	F ₁ (lbs)	Node	Q ₂ (lbs)	Node	Q ₃ (lbs)	Node	M ₂ (in-lbs)	Node	M ₃ (in-lbs)	σ (Ksi)	τ (Ksi)
6	Al	Al	0 C/Gl	Lift Z	237	47.9	21	3.68	222	155.3	21	79.0	213	1.85	1.14	0.71
7	Al	Al	0 C/Gl	Lift X	24	176	21	51.8	28	193.6	25	256	21	1.43	3.74	0.89
8	Al	Al	0 C/Gl	Trans. Z	237	62.0	21	4.76	222	201.0	21	102.2	213	2.39	1.47	0.92
9	Al	Al	0 C/Gl	Trans. Rot.	134	178	21	91.8	248	32.6	186	19.3	26	2.23	0.78	0.47
10	Al	Al	0 C/Gl	Thermal	23	-6750	248	708	28	145	28	142	26	2.21	-22.4	3.24

Table 18. Computed maximum stiffener forces and stresses in design configuration C (Gr/Ep panels and longerons, 0° P100/BSG stiffeners) of DSPSE satellite.

Run	Panel Mat'l	Long. Mat'l	Stiff. Mat'l	Load	Maximum Stiffener Loads										Max. Stress	
					Node	F ₁ (lbs)	Node	Q ₂ (lbs)	Node	Q ₃ (lbs)	Node	M ₂ (in-lbs)	Node	M ₃ (in-lbs)	σ (Ksi)	τ (Ksi)
11	Gr/Ep	Gr/Ep	0 C/Gl	Lift Z	237	53.7	21	3.57	222	220	21	104.2	213	3.34	1.47	1.01
12	Gr/Ep	Gr/Ep	0 C/Gl	Lift X	76	181.6	21	51.3	25	600	25	331	21	2.55	4.70	2.74
13	Gr/Ep	Gr/Ep	0 C/Gl	Trans. Z	237	69.5	21	4.62	222	285	21	134.8	213	4.32	1.90	1.30
14	Gr/Ep	Gr/Ep	0 C/Gl	Trans. Rot.	134	208	21	90.8	248	45.7	186	19.9	26	3.98	0.88	0.42
15	Gr/Ep	Gr/Ep	0 C/Gl	Thermal	127	-1745	248	305	17	41.3	28	28.9	21	0.136	-5.68	1.39

Table 19. Computed maximum stiffener forces and stresses in design configuration D (Gr/Ep panels and longerons, 0/45/90 P100/BSG stiffeners) of DSPSE satellite.

Run	Panel Mat'l	Long. Mat'l	Stiff. Mat'l	Load	Maximum Stiffener Loads										Max. Stress	
					Node	F ₁ (lbs)	Node	Q ₂ (lbs)	Node	Q ₃ (lbs)	Node	M ₂ (in-lbs)	Node	M ₃ (in-lbs)	σ (Ksi)	τ (Ksi)
16	Gr/Ep	Gr/Ep	Iso C/Gl	Lift Z	237	38.2	21	3.85	222	121.3	21	64.5	213	10.2	0.92	0.56
17	Gr/Ep	Gr/Ep	Iso C/Gl	Lift X	24	161.8	21	52.3	25	265	25	209	22	7.24	3.11	1.21
18	Gr/Ep	Gr/Ep	Iso C/Gl	Trans. Z	237	49.4	21	4.98	222	157	21	83.5	213	13.2	1.20	0.72
19	Gr/Ep	Gr/Ep	Iso C/Gl	Trans. Rot.	76	141.4	21	92.6	248	25.1	186	17.0	26	10.5	0.64	0.42
20	Gr/Ep	Gr/Ep	Iso C/Gl	Thermal	127	-1008	248	92.4	28	16.6	28	15.6	21	0.252	-3.27	0.42

Table 20. Computed stiffener margins of safety and weight savings for various DSPSE satellite designs that employ P100/BSG stiffeners.

Design Configuration				In-Plane Stress			Shear Stress			Bearing Stress			Weight Savings		
Design	Panel	Long.	Stiff.	Load	Stress (Ksi)	Strength (Ksi)	Margin ^a	Stress (Ksi)	Strength (Ksi)	Margin ^a	Stress ^b (Ksi)	Strength (Ksi)	Margin ^a	Structural Weight (lbs)	Weight Savings (%)
A	Mat'l	Mat'l	Mat'l												
	Al	Al	Al	Lift	1.21	40	32.1	0.40	20	49.0	1.39	40	27.8	100	-
				Trans	0.53	40	74.5	0.35	20	56.0	1.32	40	29.3		
B				Thermal	-	-	-	-	-	-	-	-	-		
	Al	Al	0 C/Gl	Lift	2.76	41.7	14.1	0.81	5.90	6.3	2.75	28.1	9.2	97	3
				Trans	1.18	41.7	29.5	0.73	5.90	7.1	2.84	28.1	8.9		
C				Thermal	-22.4	41.7	0.86	3.24	5.90	0.82	144.0	28.1	-0.81		
	Gr/Ep	Gr/Ep	0 C/Gl	Lift	3.48	41.7	11.0	2.06	5.90	1.86	2.86	28.1	8.8	70	30
				Trans	1.48	41.7	27.2	0.97	5.90	5.08	3.31	28.1	7.5		
D				Thermal	5.68	41.7	6.34	1.39	5.90	3.24	37.2	28.1	-0.25		
	Gr/Ep	Gr/Ep	Iso C/Gl	Lift	2.29	28.5	11.4	0.94	16.1	16.1	2.51	28.1	10.2	70	30
				Trans	0.96	28.5	28.7	0.59	16.1	26.3	2.26	28.1	11.4		
				Thermal	3.27	28.5	7.72	0.42	16.1	11.4	21.5	28.1	0.31		

^a Margin of safety = (strength/stress) - 1

^b Bearing stress = F_1/Dt , where $D=0.375$ in. and $t=0.125$ in.

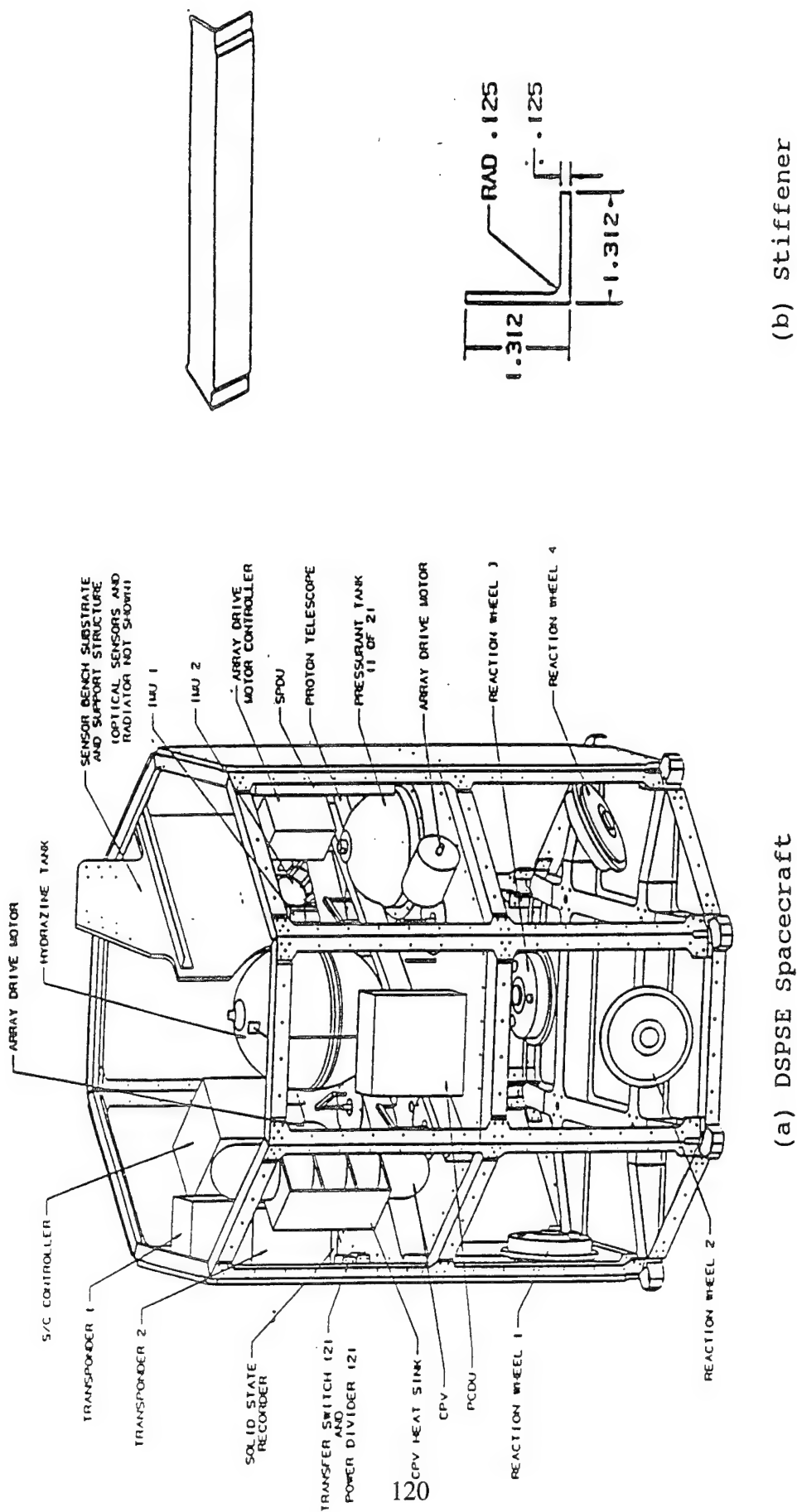
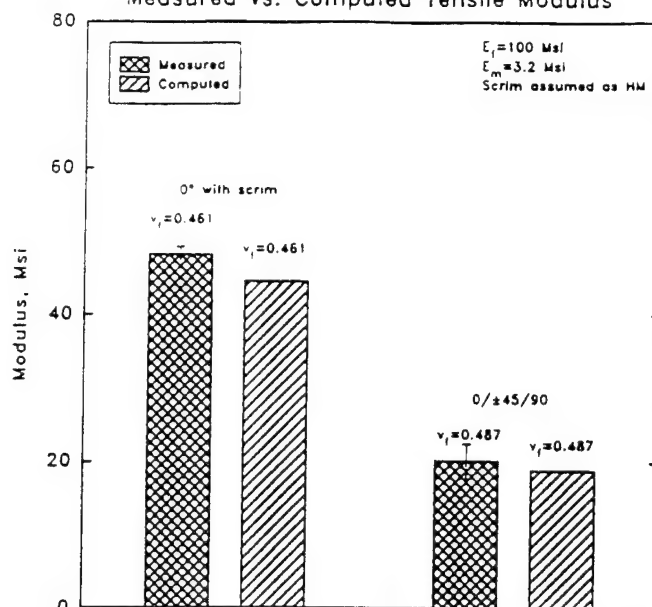


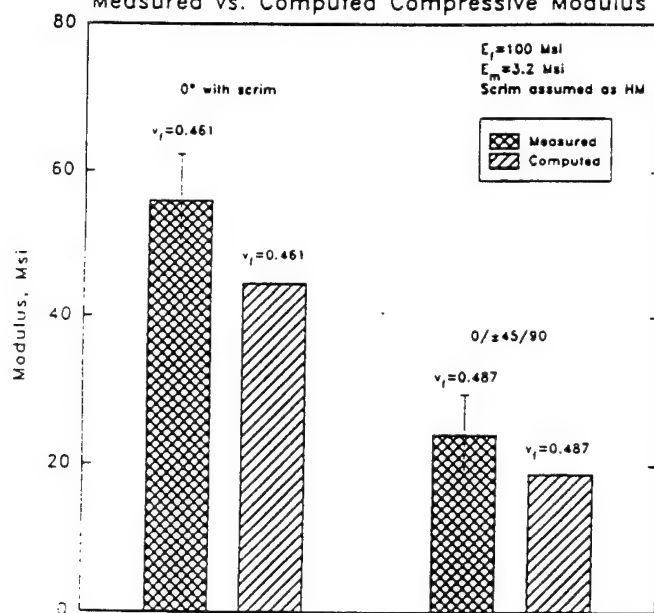
Figure 1. Schematic diagram of DSPSE spacecraft showing cross-section of stiffeners.

DATA CORRELATIONS FOR P100/BSG
Measured vs. Computed Tensile Modulus



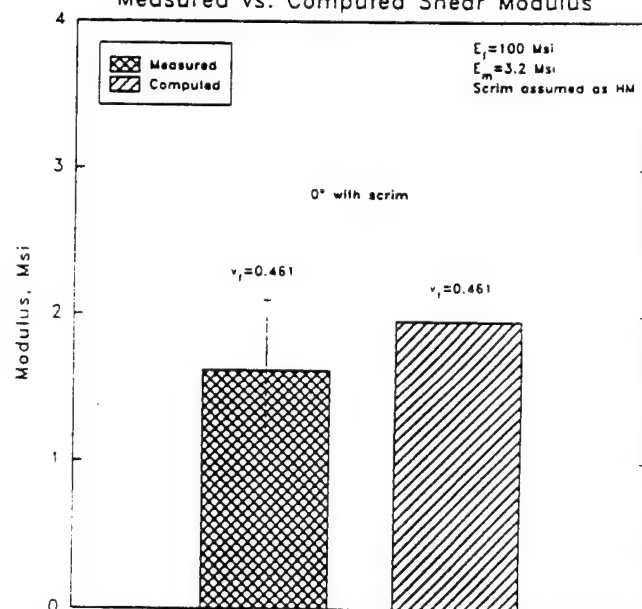
(a) Tensile

DATA CORRELATIONS FOR P100/BSG
Measured vs. Computed Compressive Modulus



(b) Compressive

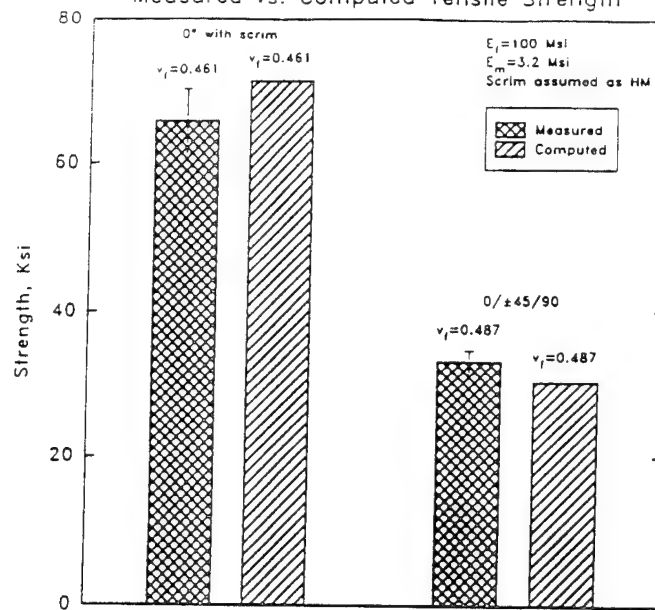
DATA CORRELATIONS FOR P100/BSG
Measured vs. Computed Shear Modulus



(c) Shear

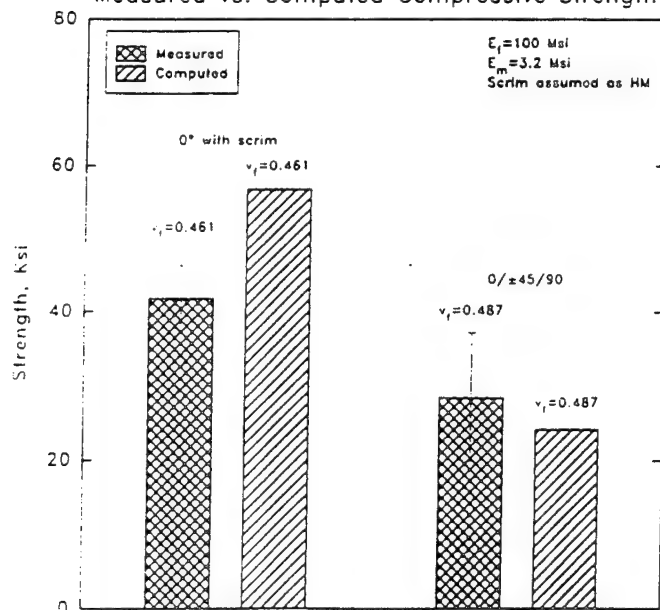
Figure 2. Comparison of measured and computed moduli for P100/BSG composites.

DATA CORRELATIONS FOR P100/BSG
Measured vs. Computed Tensile Strength



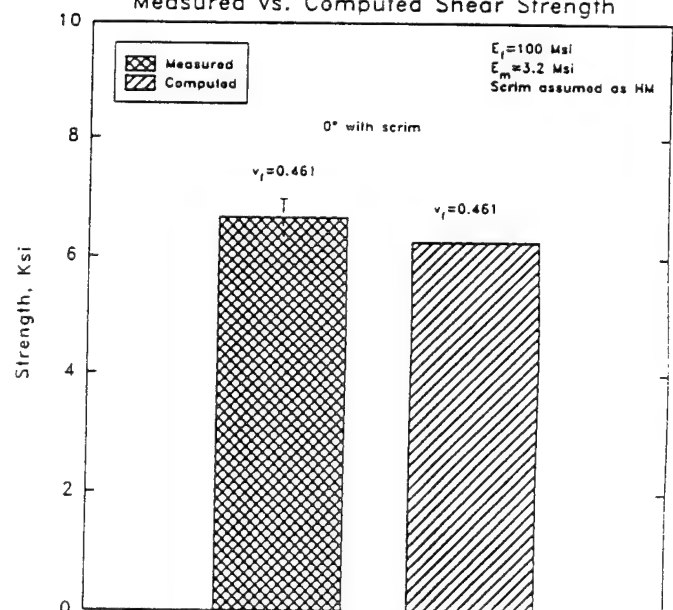
(a) Tensile

DATA CORRELATIONS FOR P100/BSG
Measured vs. Computed Compressive Strength



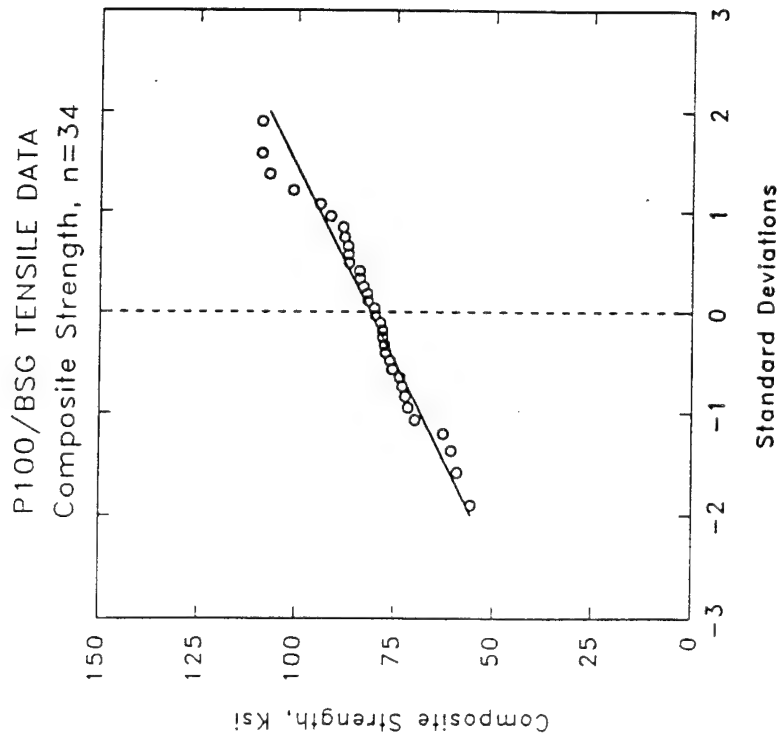
(b) Compressive

DATA CORRELATIONS FOR P100/BSG
Measured vs. Computed Shear Strength

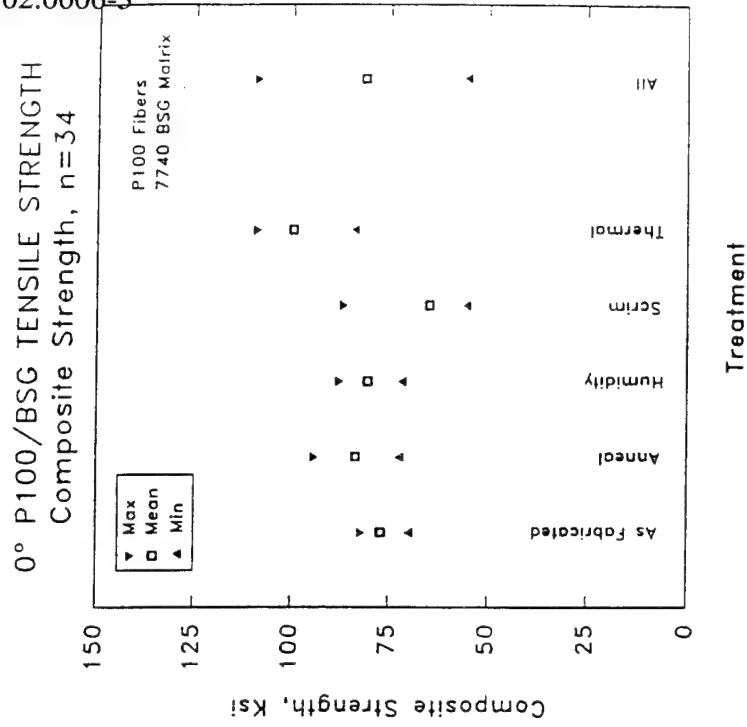


(c) Shear

Figure 3. Comparison of measured and computed strengths for P100/BSG composites.

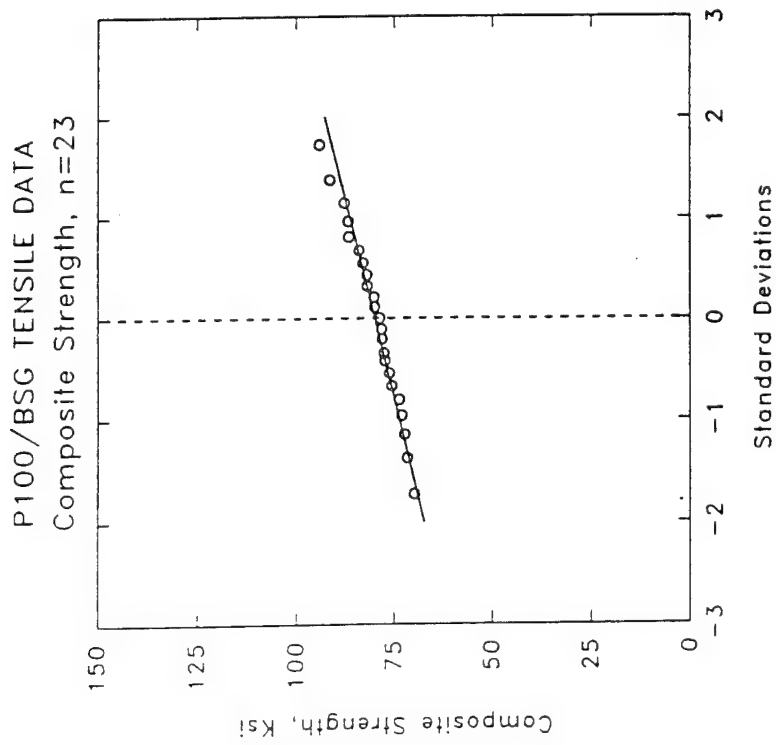


(a) Normality Test

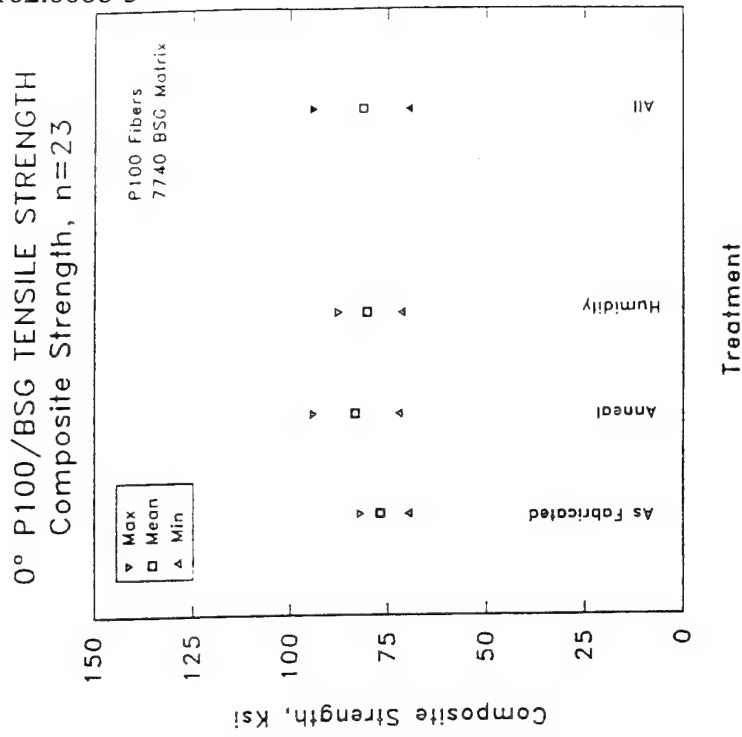


(b) Group Comparison

Figure 4. Statistical evaluations of complete data set (34 values) used in evaluation of B basis allowable for unidirectional P100/BSG tensile strength.



(a) Normality Test



(b) Group Comparison

Figure 5. Statistical evaluations of reduced data set (23 values) used in evaluation of B basis allowable for unidirectional P100/BSG tensile strength.

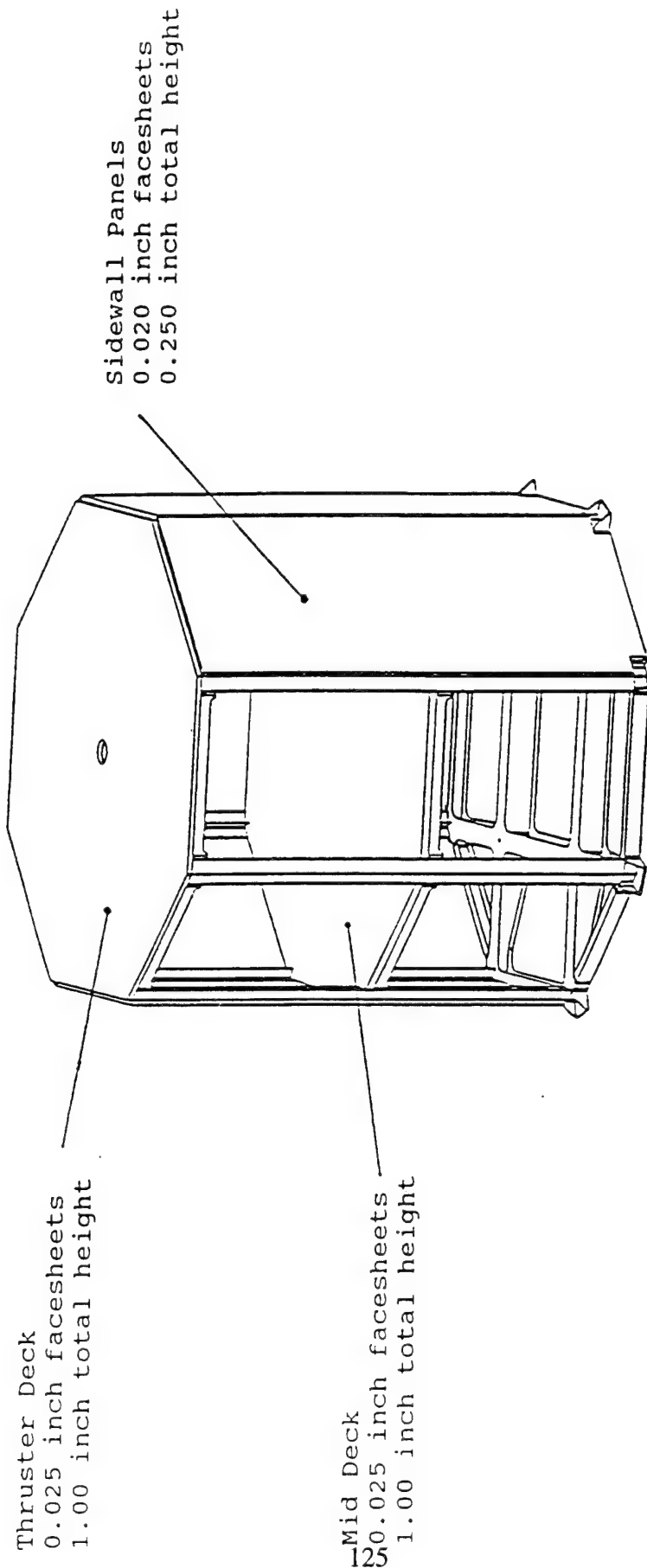


Figure 6. Schematic diagram showing dimensions of sandwich panels used in analysis of DSPSE satellite.

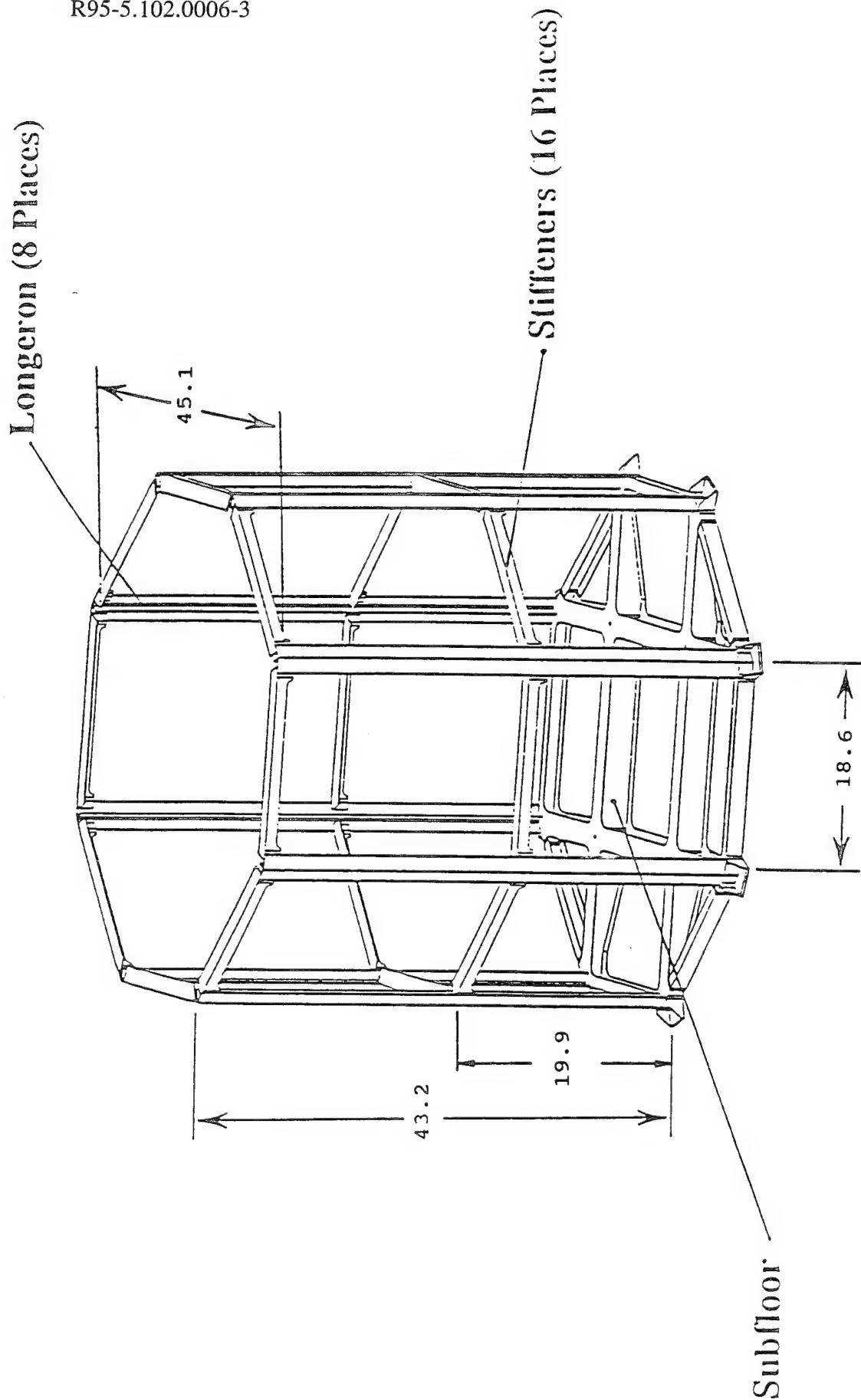
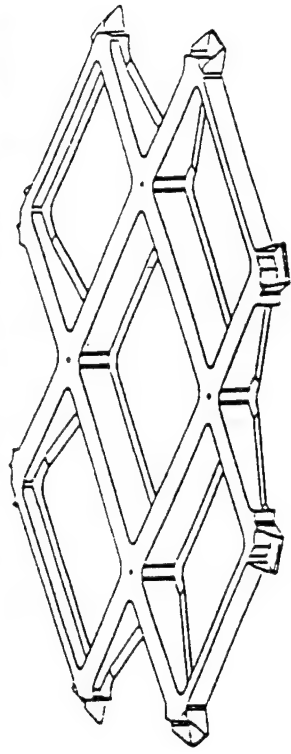


Figure 7. Schematic diagram showing dimensions of structural frame used in analysis of DSPSE satellite.



• Structural Subfloor

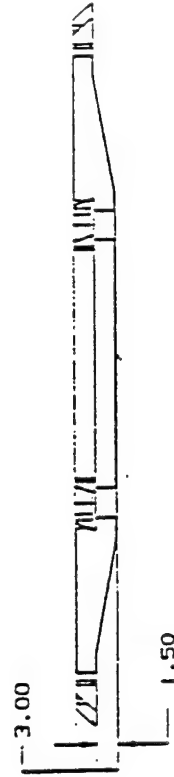
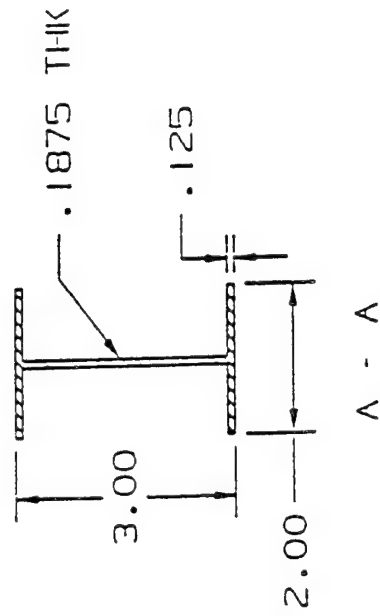
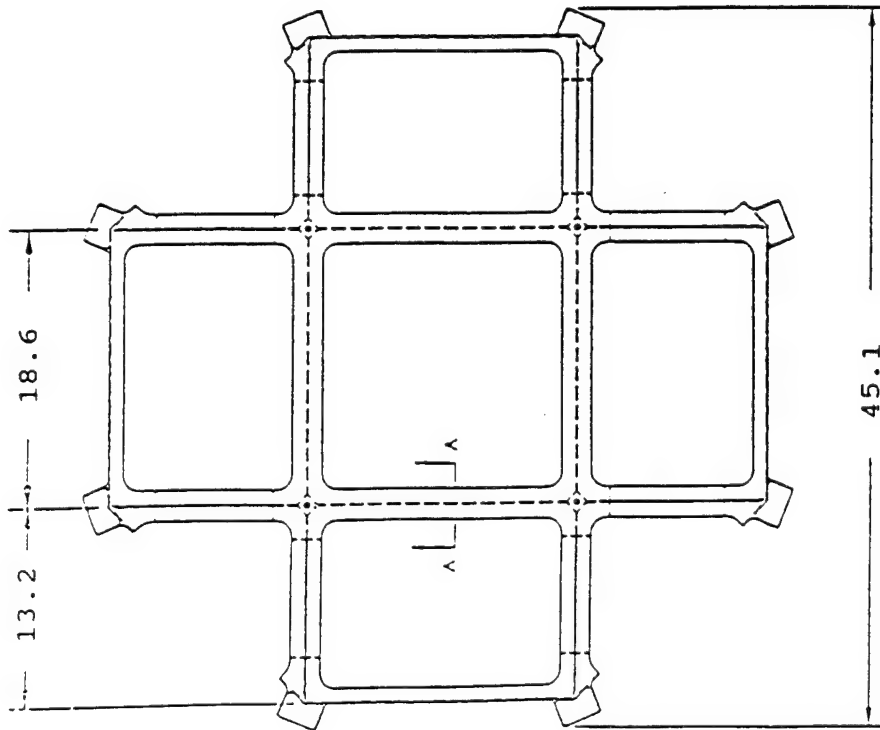
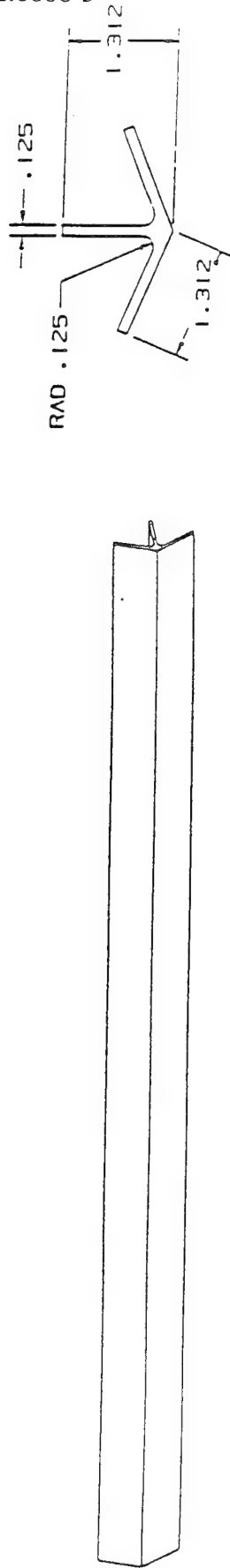


Figure 8. Schematic diagram showing dimensions of subfloor beam used in analysis of DSPSE satellite.

• Longer Design



R95-5.102.0006-3

• Stiffener Design



Figure 9. Schematic diagram showing dimensions of longerons and stiffeners used in analysis of DSPSE satellite.

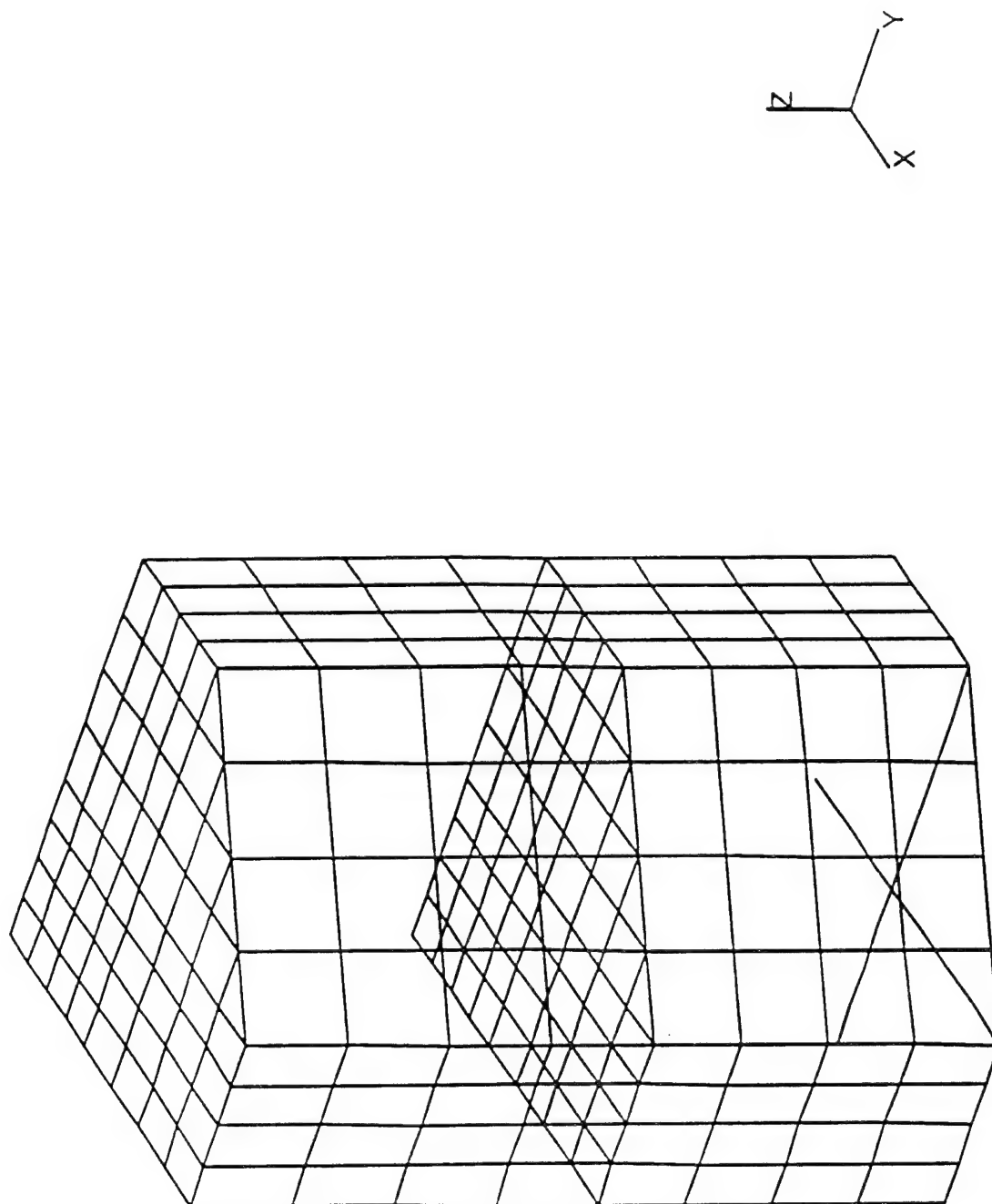
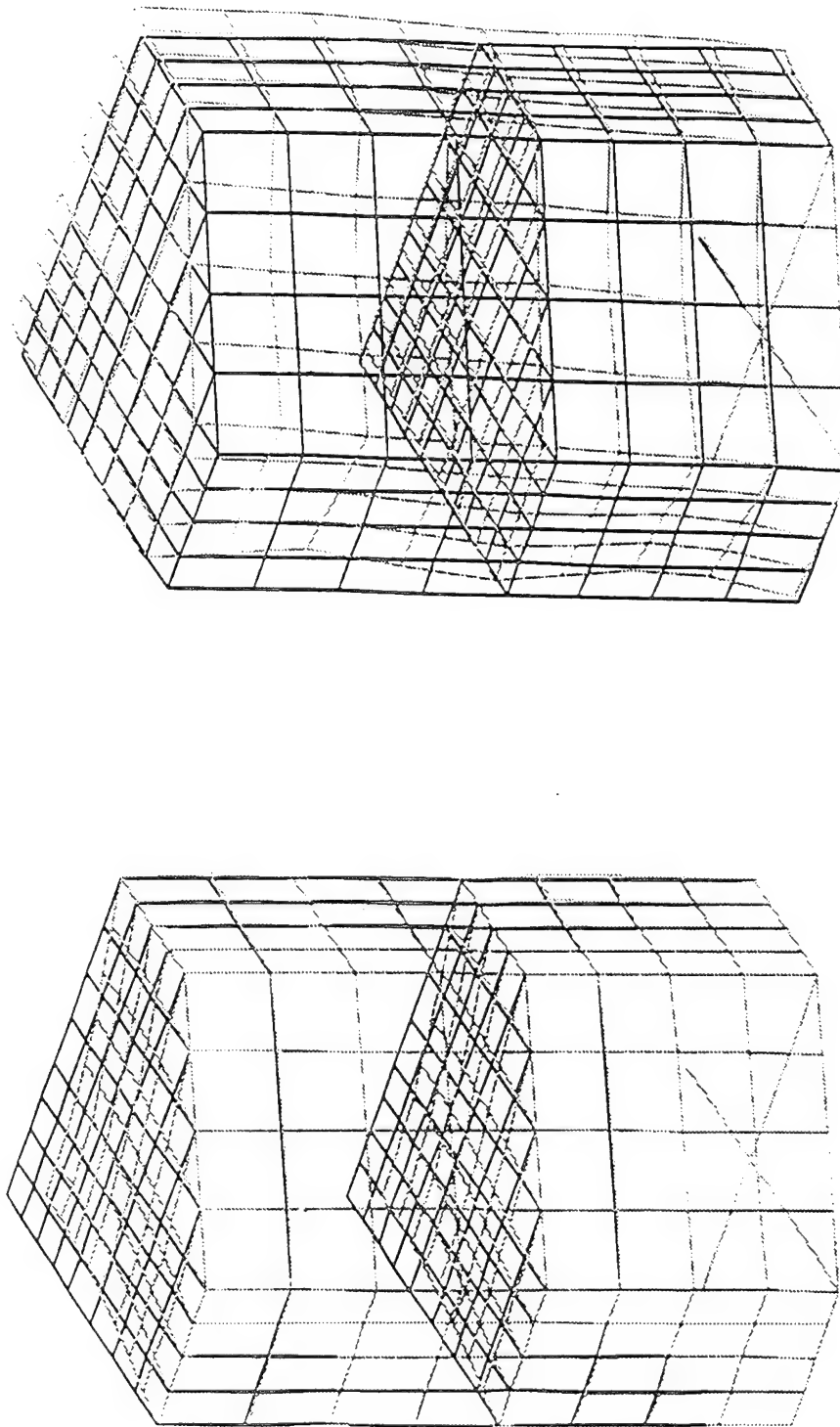


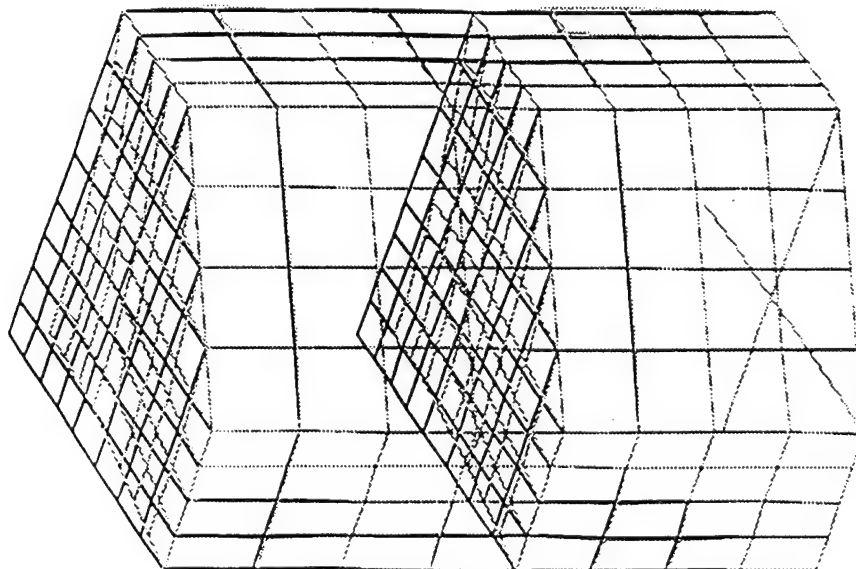
Figure 10. Finite element mesh used in analysis of DSPSE satellite.



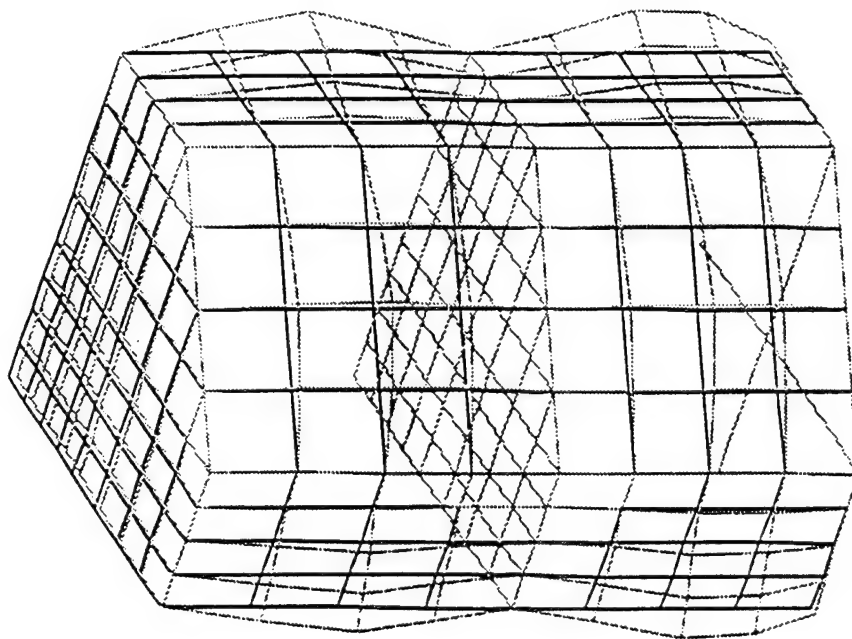
(a) Axial

(b) Lateral

Figure 11. Examples of typical computed displaced shapes of DSPSE satellite caused by liftoff accelerations (All aluminum, Design Configuration A).



(a) Axial



(b) Rotational

Figure 12. Examples of typical computed displaced shapes of DSPSE satellite caused by orbital transition accelerations (All aluminum, Design Configuration A).

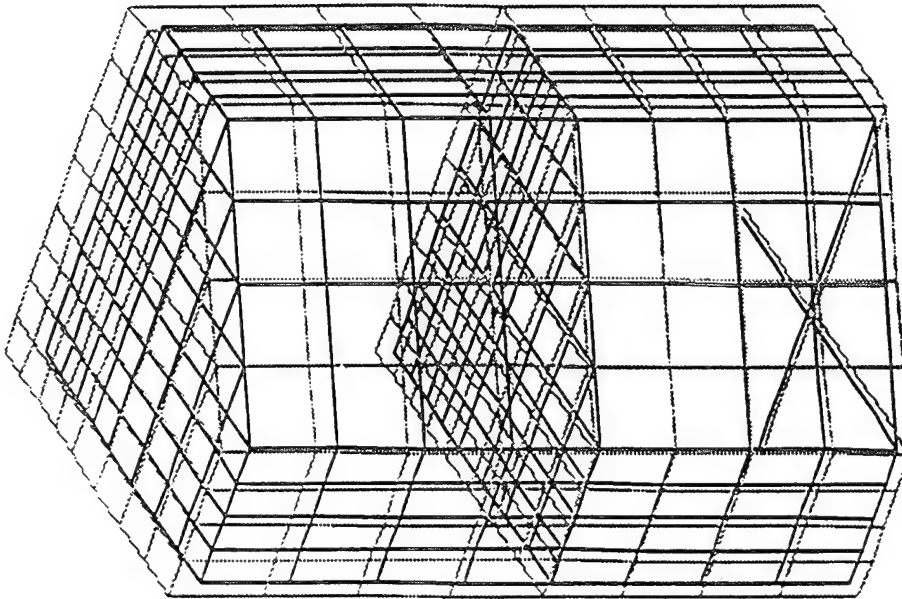


Figure 13. Examples of typical computed displaced shapes of DSPSE satellite caused by thermal cycle (All aluminum, Design Configuration A, $T_0=75^\circ\text{F}$, $T=122^\circ\text{F}$).

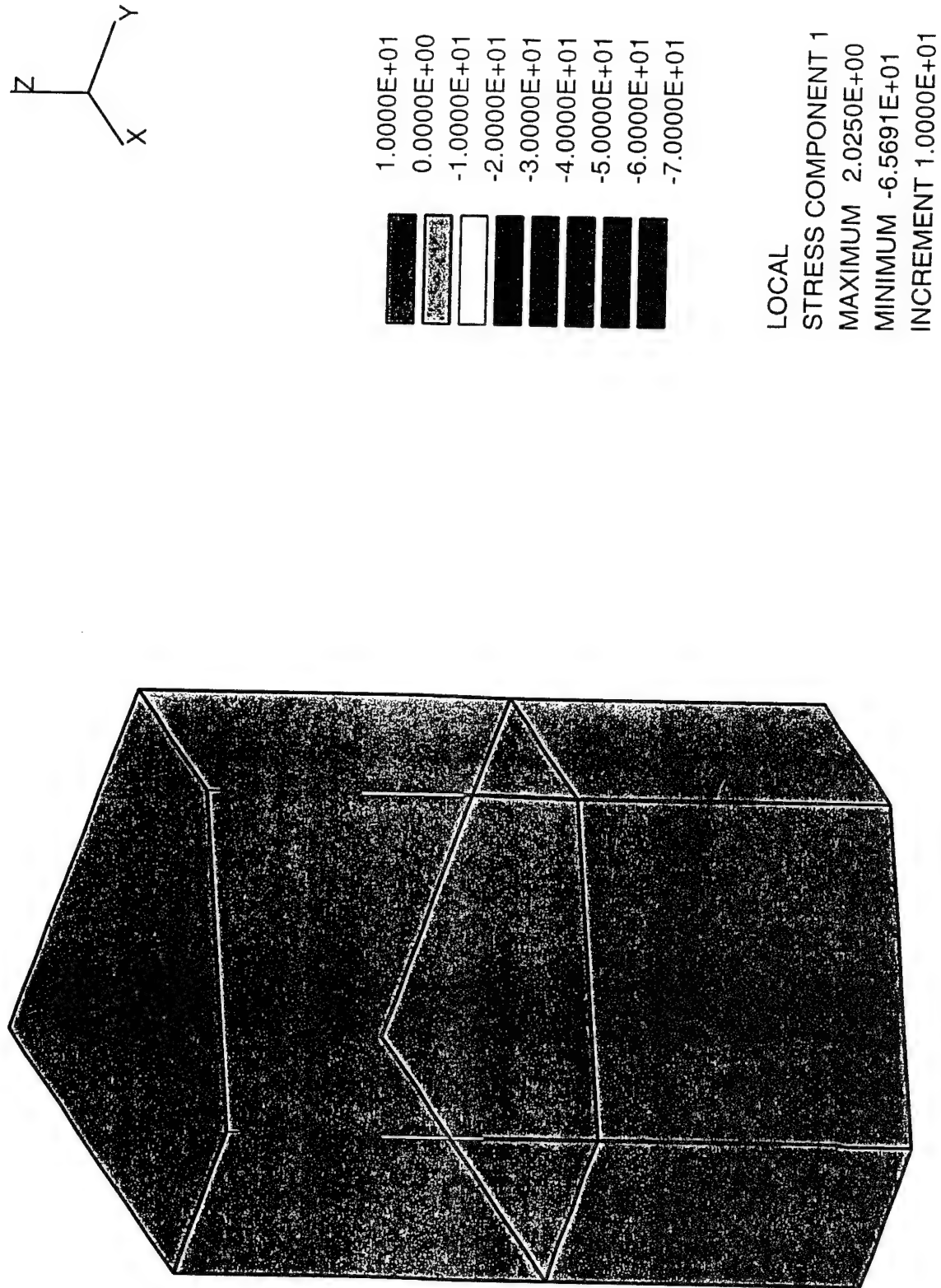
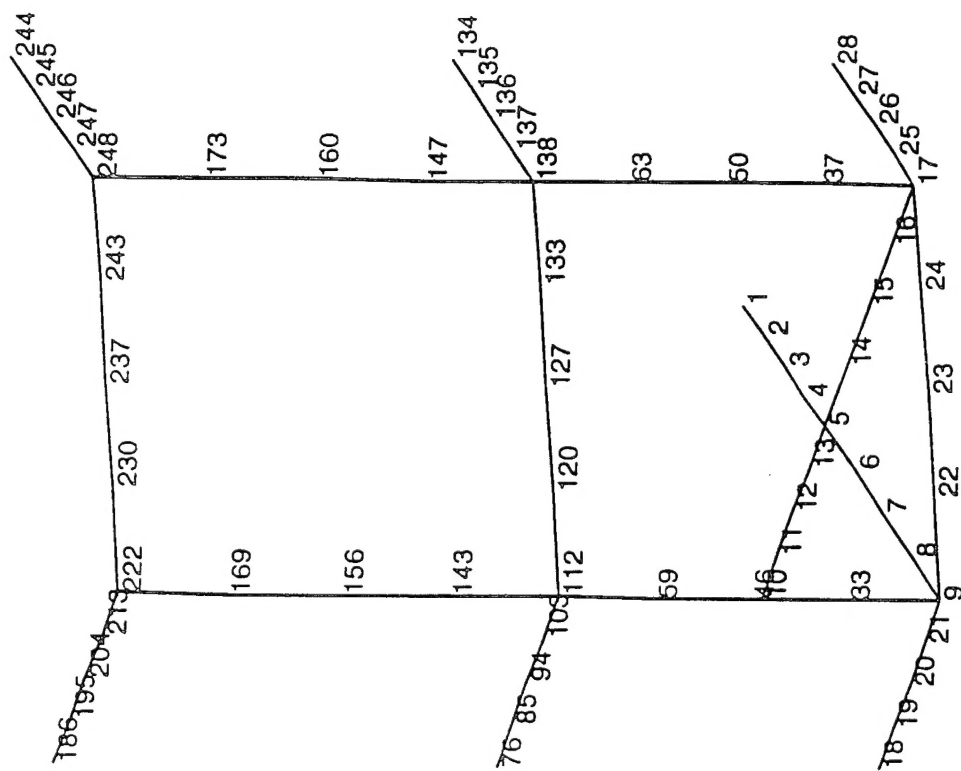
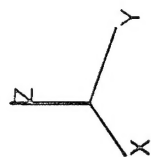


Figure 14. DSPSE Stress Example, Axial Liftoff, Aluminum (Design A)



DSPSE Satellite Structural Model - Beam Nodes

Figure 15. Partial plot of DSPSE finite element model showing nodal locations on stiffeners and longerons.

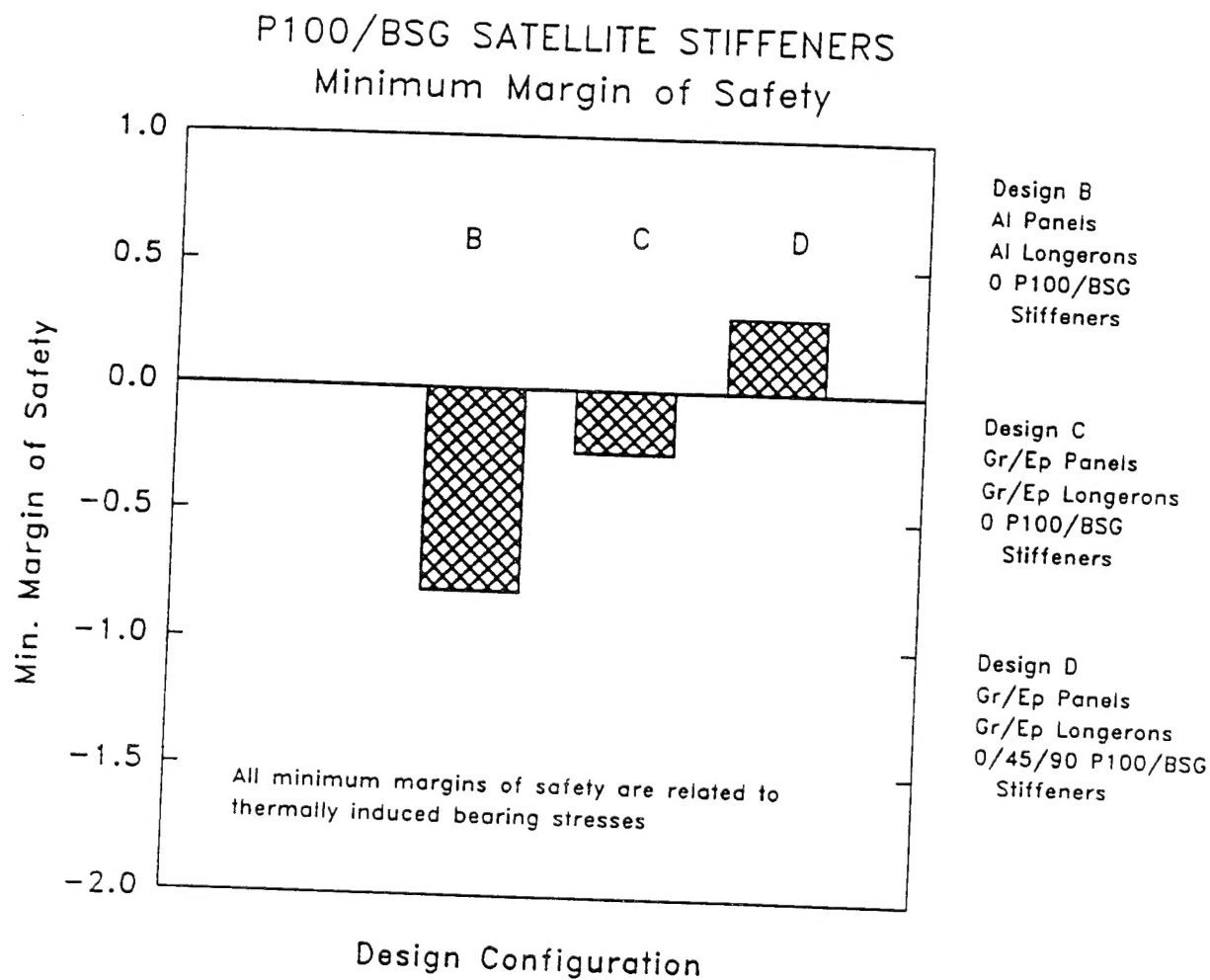


Figure 16. Comparison of minimum margins of safety computed for P100/BSG stiffeners in various DSPSE satellite designs.

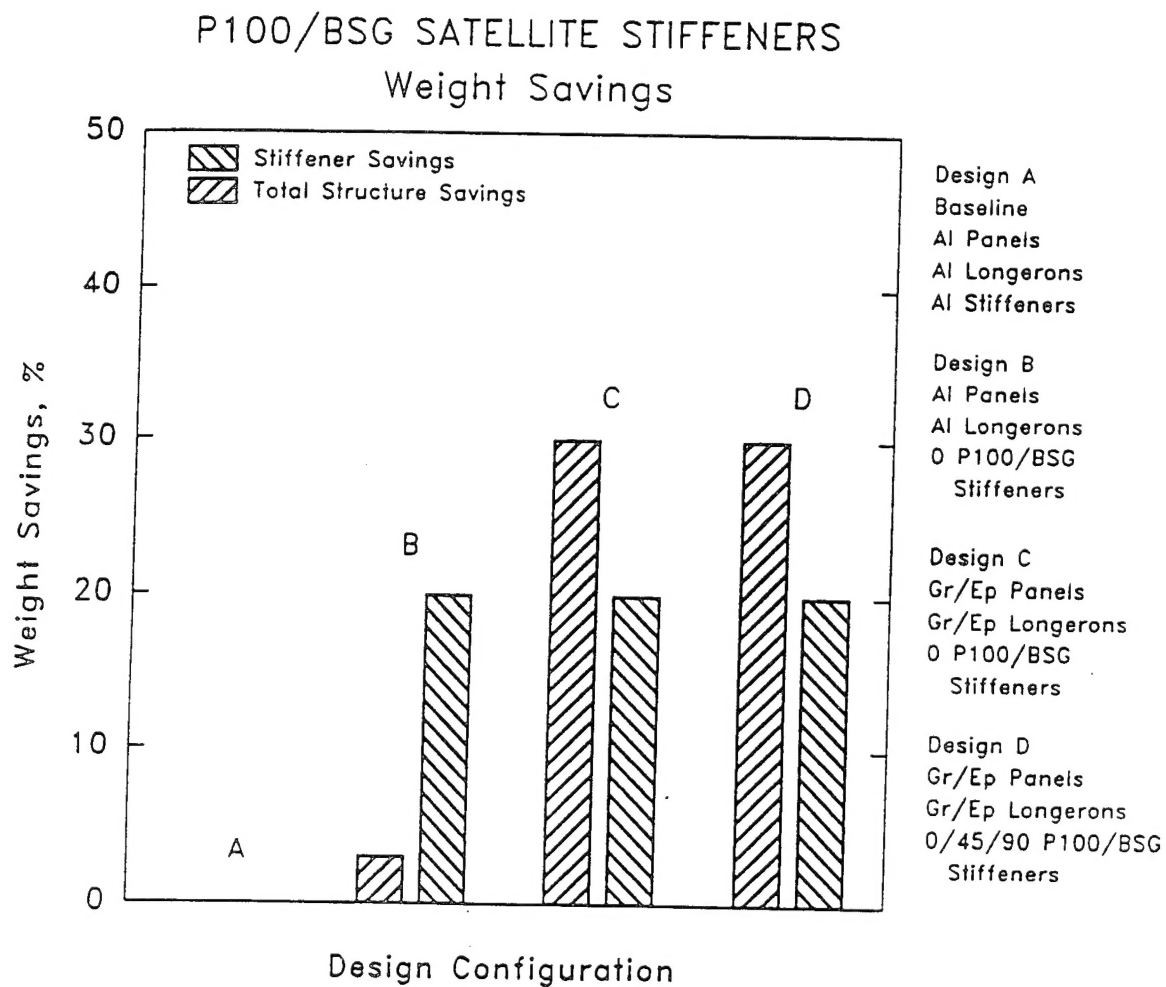
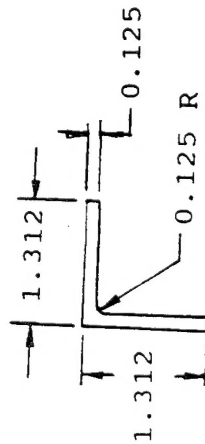
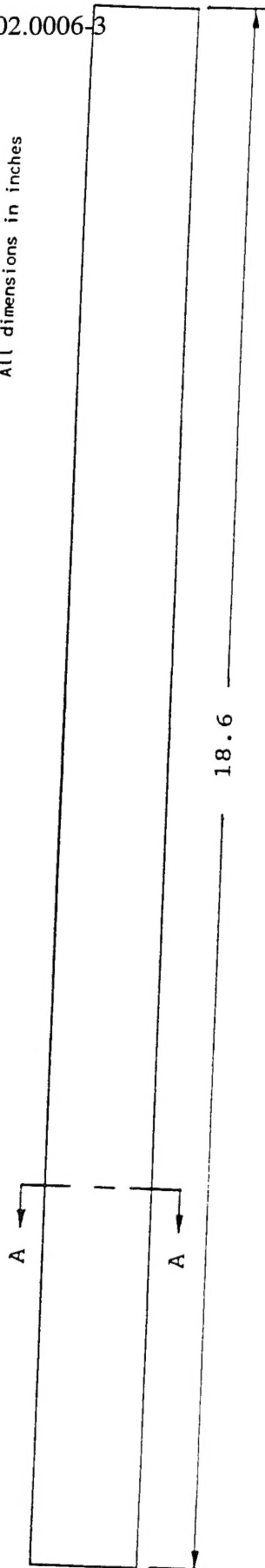


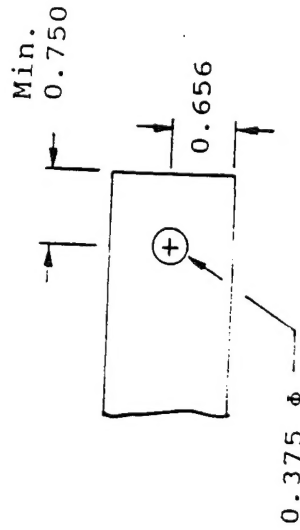
Figure 17. Comparison of weight savings computed for P100/BSG stiffeners in various DSPSE satellite designs.

Material is 32 or more plies of
balanced and symmetric 0/±45/90 P100/BSG
Bolts located as required for attachment
to longerons and panels
All dimensions in inches

955.102.0006-3



A - A



Bolted Joint Detail

DSPSE SATELLITE STIFFENER
DWG. No. 941606-1
KWB 6/16/94

Figure 18. Recommended design of P100/BSG stiffener for use in DSPSE satellite.